Split-Beam Sonars:
A backscatter model and prototype data analysis

by

© *Axel Belgarde*

A thesis submitted to the

School of Graduate Studies

in partial fulfilment of the

requirements for the degree of

Master of *Science*, Physical Oceanography

Department of *Physics and Physical Oceanography*

Memorial University of Newfoundland

February 2024

St. John's Newfoundland

Abstract

Split-beam echosounders provide estimation of fish size by directly measuring their target strength. A model that can be used to evaluate and optimize split-beam sonar performance is presented. The model has been used to generate beam patterns to match prototype instruments and to simulate acoustic signals based on the scattering of sound from particles in a three-dimensional domain. The sum of the contribution of the scatterers is sampled at the transducer locations, resulting in simulated signals used for data processing and sonar performance prediction. The model's capabilities were evaluated through comparisons with ASL Environmental Sciences' AZFP-Split prototype system. The field trials were conducted in Saanichton, BC, by lowering a calibration target sphere to a range of 220 m in the acoustic beam. Both model prediction and prototype system performance show accuracy of $\sigma = 0.2$ dB at 25 m range. Potential future applications of the model include exploring methods of target separation and improving accuracy when presented with complex target structures.

Acknowledgements

First of all, I am immensely grateful to Dr. Len Zedel, my supervisor, whose unwavering support and depth of knowledge have been invaluable. His ability to infuse humour into the challenges of graduate school is truly remarkable. I am incredibly fortunate to have him as my supervisor, his guidance made this whole journey an unforgettable experience.

I would like to express my sincere thanks to my colleagues of my research group, Josianne Ostiguy, Seyed Mohammad Mousavi, Nurul Ibrahim, and Shane Anderson, as well as the entirety of the physics and physical oceanography graduate students for supporting my endeavours and making a welcoming environment.

A special acknowledgment goes to thank Mahdi Razaz, who collaborated on this project and helped with the foundations of this model. He provided the support and the insight to lead my research in the right direction.

I am grateful for the opportunities provided by the IMERIT program and NSERC funding. Conferences, meetings, and travel experiences have been crucial for sharing research with peers and advancing scientific progress.

Thank you to everyone at ASL Environmental Sciences, for having faith in my capabilities and having me taking part in this project. A special appreciation to Jan and Des Buermans for their hospitality during my internship with the company.

Lastly, thank you to François Thibault, Jean-David Moisset, Simon Lizotte, Alexandre Cléroux Cuillerier, Antoine Légaré, Gabrielle Jess, Olivier Ribordy, and Zacharie Aubin, for whom I am eternally grateful for their unconditional support, even many time zones apart.

Contents

List of Tables

List of Figures

Nomenclature

Abbreviations

ADC Analog-to-digital converter

BEM Boundary element method

CTD Conductivity, temperature, and pressure profiler

CW Continuous wave

dB Decibels

DCM Deformed cylinder model

DFO Fisheries and Oceans Canada

DOA Direction of arrival of the backscattered signal

FFT Fast Fourier transform

FPGA Field-programmable gate array

KRM Kirchoff ray-mode approximation

MAE Mean absolute error

MUN Memorial University of Newfoundland

NOAA National Oceanic and Atmospheric Administration

NSERC Natural Sciences and Engineering Research Council of Canada

PSU Practical salinity unit

RMS Root mean square

SNR Signal-to-noise ratio

TOI Targets of interest

TS Target strength

Symbols

α Measured angular position of TOI with boresight on the x-axis

α_c Absorption coefficient

β Measured angular position of TOI with boresight on the y-axis

δ_x Phase difference between channels 1+4 and 2+3, used to measure α

δ_y Phase difference between channels 1+2 and 3+4, used to measure β

κ Demodulation coefficient

λ Wavelength of the transmitted pulse

$\mathbf{V}_j$ Velocity of the j-th particle

$\mathbf{X}_j$	Position of the j-th particle on the x axis
$\mathcal{F}$	Discrete Fourier transform
AL	Absorption loss of TOI
DI	Directional compensation of TOI
$\mathrm{d}t$	Model time step
$\mathrm{d}t_s$	Digital demodulation rate
RL	Received level of TOI
SL	Source level on transmit
TL	Transmission loss of TOI
TS	Target strength of TOI
$\overline{\mathrm{TS}}$	Mean target strength of TOI
σ	Standard deviation
σ_{bs}	Backscattering cross-section
τ	Pulse length
θ	Measured angular position of TOI with boresight
$\theta_{-3\mathrm{dB}}$	-3 dB beamwidth, defined by the angle from boresight to the half power point
θ_{lim}	Angle limit of ambiguity, corresponds to location of phase wrapping

a	Radius of the transducer
B	Bandwidth of the pulse
$C(t)$	Demodulated acoustic backscatter signal, given by $C(t) = I(t) + iQ(t)$
$c(t)$	Demodulated pulse template
c	Speed of sound underwater
d	Separation between transducer elements
f_c	Carrier frequency of the pulse
f_s	Re-sampling frequency
$I(t)$	In-phase component of the demodulated signal
I	Measured intensity of the TOI
k	Wavenumber of the pulse
n_i	Number of particles generated by the model in the domain
n_p	Number of pings
n_{pi}	Number of pings with a detected target
$Q(t)$	Quadrature component of the demodulated signal
r	Measured range of the TOI
R_0	Theoretical farfield

r_{ri} Distance between the receiver and the point scatterer

r_{si} Distance between the transmitter and the point scatterer

$S(t)$ Acoustic backscatter signal generated by the model

$s(t)$ Transmit pulse template

t_{e} Elapsed time between transmit and the received echo of the TOI

x Cartesian coordinate aligned with the athwartship axis

y Cartesian coordinate aligned with the alongship axis

z Ocean depth, surface is defined at $z = 0$ m, and positive axis is toward the ocean floor

Chapter 1

Introduction

The term *sonar* stands for **sound navigation and ranging**. It refers to a technique or a device that uses underwater sound propagation for different purposes, including navigation, distance measurement, communication and target detection. Sonar systems fall into two main categories: passive and active sonars. Passive systems are the simplest underwater acoustic devices, and refer to a sonar system that is only recording the ocean sound without emitting sound in the environment. On the other hand, active sonars have their transducer wired to an amplifier, emitting a pulse in the water column, and recording the data from the backscatter pulse. Split-beam sonars are active systems, and their principle is explained in detail in the following sections.

1.1 Active sonar principle

Active sonar systems transmit a sound pulse into the water environment and gather information on a target from the recorded reflected echo. As illustrated in Figure 1.1,

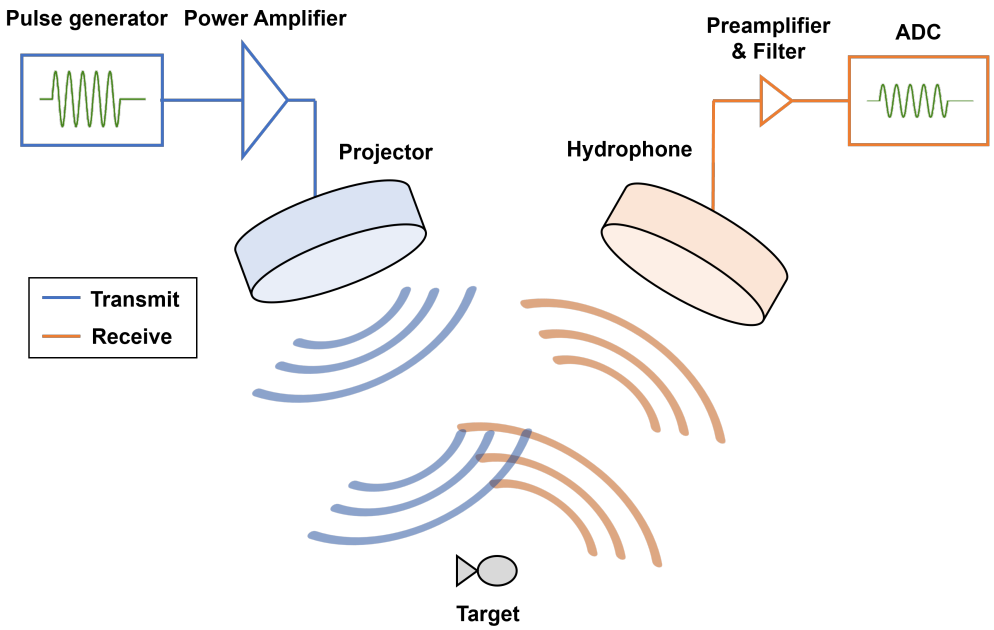

Figure 1.1: Representation of an active sonar system with separate transducers for transmitting and receiving the sound pulse.

an electric pulse is generated and amplified before being converted into a sound pulse by a transducer or an array of transducers called a projector or transmitter. The sound is then reflected off targets in the water and the echo is captured by another transducer or array of transducers, called a hydrophone or receiver. The pulse is then converted into an electric signal, preamplified, filtered and converted to digital data to be analyzed. Some sonar designs, like the split-beam sonar, use the same transducer for both transmitting and receiving by switching the operation of the transducer. With a single projector and hydrophone, the retrieved information from the recorded signal about a target includes the range and the intensity.

The range of a target is measured using the time elapsed between the transmission of the pulse and the detection of the reflected echo, and the speed of sound in the

water. The latter is generally obtained from an empirical equation using measurement of temperature and salinity at various depths in the water column. Medwin (1975), provided a simple empirical formula to measure the speed of sound in m/s

$$c = 1449.2 + 4.6T - 0.055T^2 + 0.00029T^3 + (1.34 - 0.01T)(S - 35) + 0.016z \quad (1.1)$$

where T is the temperature in degrees centigrade, S is the salinity in PSU (practical salinity unit), and z depth in metres. This equation is accurate to 0.1 m/s and good to 1 kilometre depth. This accuracy is sufficient for the model needs, and the equation was chosen over other existing empirical equations.

The echo intensity is a function of the size of the target, the location of the target in the acoustic beam pattern, the frequency used, and the material properties of the target. The size of the target impacts the receive intensity, since a larger surface reflects more energy back to the receiver. In fisheries acoustics, this acoustic size is referred to as *target strength* (TS), with units in dB re 1 m^2. Love (1971), suggested an empirical formula approximating the dorsal-aspect target strength of an individual fish from its length. The simplest TS-length relationship, as suggested by Foote (1979), comes in the equation

$$\mathrm{TS} = 20 \log L + b_{20} \quad (1.2)$$

where L is the fish length in cm and b_{20} is an empirical parameter specific to species and frequency. Target strength has since become the *de facto* way to refer to fish size using acoustic instruments. However, recent publications propose abandoning the utilization of a relationship based on length, as suggested in equation (1.2), in favour of alternative equations for estimating TS in relation to fish size (McClatchie, Macaulay, and Coombs (2003)).

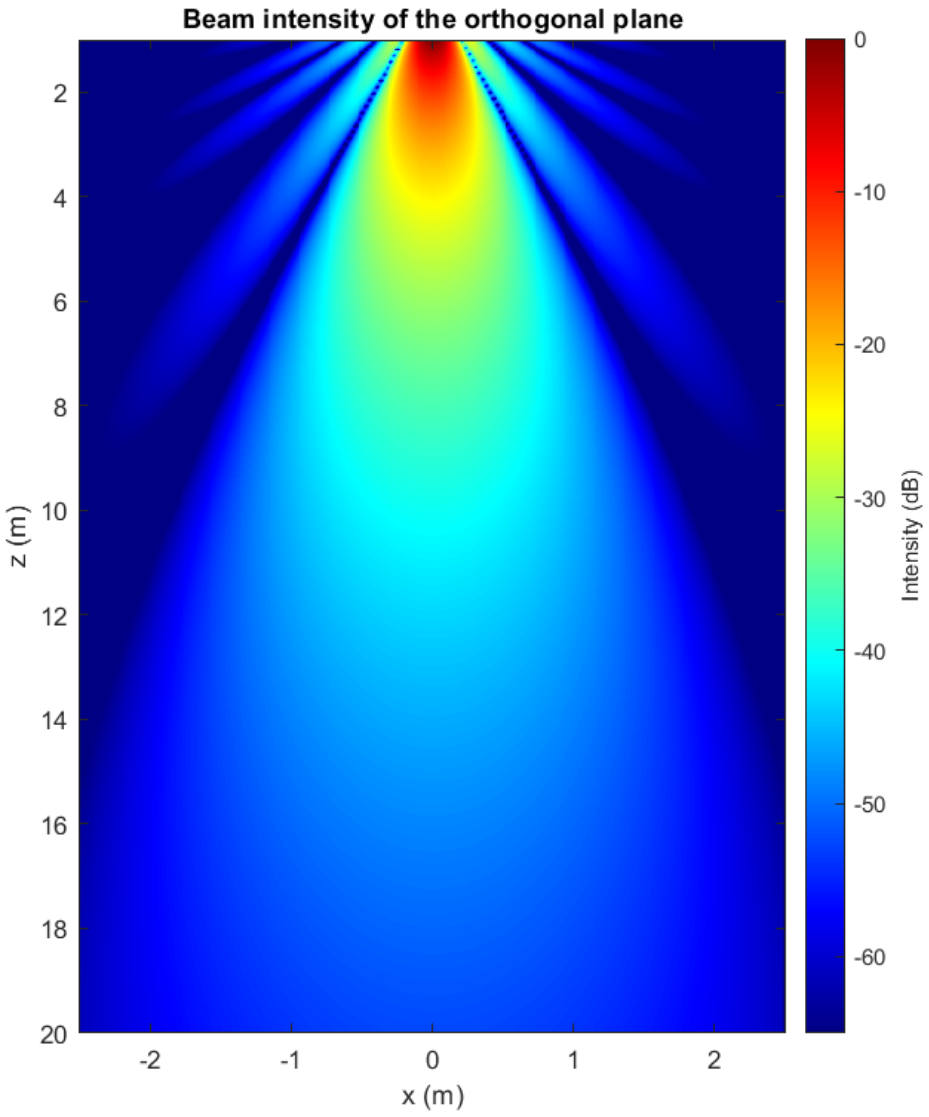

Figure 1.2: Orthogonal representation of the modelled two ways beam pattern intensity. The main lobe is the beam of high intensity centred at $x = 0$ m, and the side lobes appear in the positive and negative x axes.

Figure 1.2 shows the acoustic beam intensity of a circular transducer in depth. The intensity of the received echo from a backscattered pulse of a target will be determined by its position in the acoustic beam. As illustrated by the figure, both the range of the target and the angle of the target with the acoustic axis play a role in the received backscattered echo. Furthermore, the beam pattern effect needs to be considered for both the receiver and the transmitter beam patterns to accurately measure the backscattered echo intensity. The figure also shows side lobes, represented by diagonal beams on the left and right of the main lobe. These side lobes need to be accounted for in target detection, because a target located in a side lobe can be ambiguously detected as a target in the main lobe. Methods to minimize side lobes are often used in transducer designs, and post-processing methods are applied in algorithms to avoid target detection outside the main lobe.

For fisheries sonars post-processing algorithms designed to retrieve the fish size from a received signal, information on the 3D location of the target is needed to correctly measure the target strength. While the range can be measured with simple active sonars, more complex transducers are needed to measure the angle of the target with respect to boresight and correctly compensate the backscattered echo.

1.2 Split-beam echosounding principle

The term *echosounder* can be used interchangeably with the word *sonar*, as there is no official definition on how to discriminate one from the other. However, echosounders are usually referring to an active hydroacoustic instrument pointing downwards. The split-beam sonar, as it is used in the presented model and prototype, is an instrument

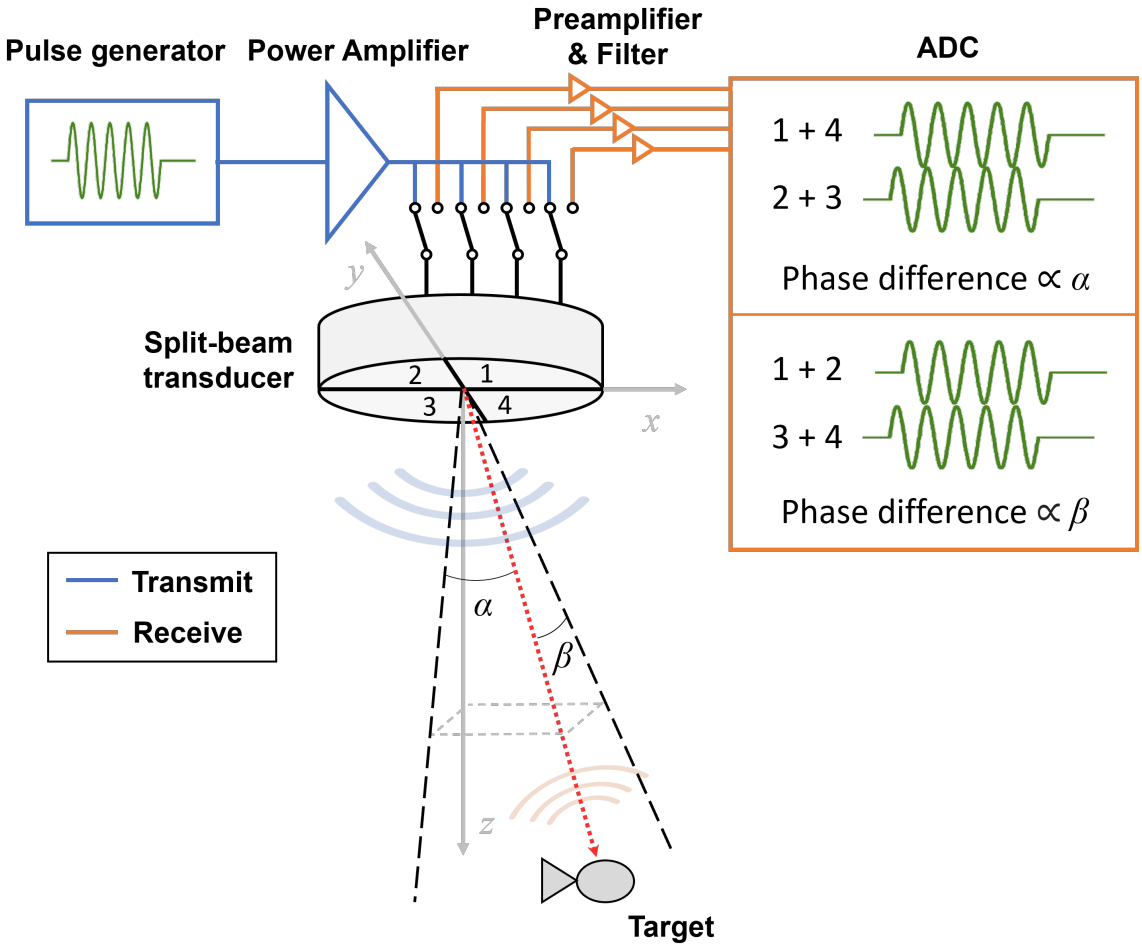

Figure 1.3: Principles of the split-beam echosounder. The target direction is determined by α and β which are the angles from the athwartship and alongship axes respectively. Signals from the four transducer quadrants are combined in pairs giving phase differences, which are proportional to these angles.

pointing downward and can thus be referred to as an echosounder.

Split-beam sonars are echosounders that provide *in situ* measurement of target strength by calculating the angular position of the target in the beam. This is achieved with a single transducer split into four quadrants. These quadrants are wired in a way to emit a pulse synchronized as one transmitter, but act as independent receivers upon the reflection of the echo. A wavefront backscattered from a target off-axis with boresight is detected by each quadrant with a time delay. The time delay, or phase difference, between the pairs of quadrant on the x axis is proportional to α, the angular position of the target with boresight on the x axis. Similarly, the two pairs of quadrants on the y axis is proportional to β, as shown in Figure 1.3. The angle with boresight θ is then defined by

$$\theta = \text{atan}\left(\sqrt{\tan^2(\alpha) + \tan^2(\beta)}\right) \tag{1.3}$$

and can be approximated to $\theta \approx \sqrt{\alpha^2 + \beta^2}$ for small values of α and β. Along with the range measurement, the angle measurement on both axes provides information on the target location in a 3D space. The target strength can then be evaluated from the intensity of the signal that is compensated with the transducer sensitivity given the position of the target in the beam.

1.3 Motivation for research

Split-beam echosounders have been on the market since the 1980s. It was first introduced as a commercial device for fisheries, but was later converted into a research instrument initially from the work of Foote, Kristensen, and Solli (1984). Split-beam

sonars have since become the industry standard for *in situ* target strength measurement. It is used to estimate size of fish, density of fish schools, and provide insight as to the species of fish. Their commercial availability makes it a tool that is easy to operate with the right training. However, the research publications on the technology do not show any details in the algorithms used to measure the position of the target since the first developments. The use of linear approximations and empirical equations for correction indicates the potential for improvement in accuracy with split-beam systems. Current computational and digital tools can be used to better understand and improve the position and target strength measurement techniques.

Because the target strength is measured by compensating the received signal with the location of the target in the beam, knowledge of the beam pattern of the transducer is needed. This is traditionally achieved through a calibration process, where the beam pattern is measured from the transducer in a controlled environment. Using computational tools to model the beam pattern of any given geometry can help improve the accuracy in the target measurements by mapping values of phases and intensity in the three-dimensional domain. Position and target strength measurement could then improve in accuracy by correcting the values for beam patterns of any geometries.

No model of the split-beam system has been made publicly available. A simulation of a split-beam sonar operation using point scatterers in a three-dimensional domain, backscatter theory, and data processing algorithms would provide a powerful tool for sonar designs by predicting the system performance. This tool can be used to guide the industry with modelling the beam pattern of a transducer geometry and evaluate the sonar performance before committing to a hardware design. It can also

be used as a way to improve the data processing algorithms, and exploring potential improvement such as methods of target separation and improving accuracy when presented with complicated target structures.

This project was an NSERC funded collaboration between MUN and ASL Environmental Sciences, an oceanographic, acoustic, remote sensing and ice research company based in Saanichton, British Columbia. For over 40 years, they have worked on developing acoustic and oceanographic instruments such as the Acoustic Zooplankton Fish Profiler, Ice Profiling Sonar and the Shallow Water Ice Profiler. With the intention to enter the market of split-beam echosounders for fisheries, a collaboration with MUN was established to work on a prototype of the AZFP-Split. The research goal was to create a split-beam echosounder model to provide insight on the sonar performance for various transducer geometries and parameters that were considered by ASL for the prototype instrument. Other objectives of the model include help identifying limitations of split-beam sonars, acting as a platform to explore computational tools for data processing of the prototype calibration and field trials, and confirm the model simulations with the results from the prototype output.

1.4 Outline of the thesis

This thesis is built in five main chapters to cover the literature review, a description of the split-beam sonar model, and the work done with the prototype instrument. The following chapter presents the literature review by exploring the interest in target strength measurement, with a focus on the utilization of dual-beam sonars and split-beam sonars. The latter is investigated in detail, covering previous research in

directivity correction and in comparative analysis with dual-beam sonars. Chapter 3 describes a MATLAB model designed for acoustic backscatter signal modelling. This includes the setup of the model, creation and movement of particles, beam pattern generation, and digital demodulation. The data processing techniques are presented, encompassing target detection, range and phase difference measurement, angular position estimation through various methods, and target strength estimation. The results from the generated model simulations are presented in chapter 4, with analysis of position measurement accuracy, target strength measurement consistency, and the impact of the number of particles, pulse length, and sampling frequency on the model. Chapter 5 discusses the development and analysis of the AZFP-Split prototype, including the calibration process and field trials. The results from the post-processing data analysis is presented in chapter 6, along with a comparison with the simulation results. Finally, a summary of the model and field trial results is presented in chapter 7, highlighting key findings and potential avenues for future work with the model.

Chapter 2

Literature Review

2.1 Interest for target strength measurement

Knowledge of fish and other organisms as acoustic objects is essential both for their identification or classification as well as their sizing and abundance estimation. Since the 1930s, a considerable amount of activity of acoustic fisheries has been concentrated on the study of target strength of fish and of other marine organisms. The early techniques for estimating fish abundance involved manually processing the marks on an echogram. However, these methods were very inaccurate and time-consuming. Better understanding on target strength theory was needed to improve identification of fish size and abundance estimation. Midttun (1984) gathered the extent of knowledge on target strength to elucidate the concept since there was no acoustic theory which could fully describe the process of scattering from complex targets such as fish and other marine organisms at that point in time. The paper states the philosophy behind target strength measurement in two parts. Firstly, target strength measurement

from the scattering of a fish must require carefully controlled conditions where the variables can also be observed, including the acoustic wavelength, fish species, size, orientation and swim bladder condition. Secondly, *in situ* observations on wild fish have the advantage of being a direct way to measure fish in their natural habitat.

The first part of target strength theory has been explored with encaged and stunned fish in controlled areas, *in situ* observations proved itself to be more challenging. The lack of control over the target being measured and the transducer directivity adds complexity to an instrument designed for this purpose. To elucidate on the transducer directivity, Ehrenberg (1989) describes the received intensity I of an acoustic echo reflected from an individual scatterer at an angular position θ from the acoustic axis and a range R as a function of the backscattering cross section σ_{bs} as

$$I = k\frac{10^{-2\alpha_c R}}{R^4}|D(\theta)|^2\sigma_{bs} \tag{2.1}$$

where k is a scale factor that can be determined during the system calibration, $10^{-2\alpha_c R}$ is the range dependent loss due to absorption, $1/R^4$ is the loss due to spreading, and $|D(\theta)|^2$ is the transducer two-way beam pattern function. The target strength, expressed in dB re 1 m^2, is the logarithmic function of the backscattering cross-section:

$$\mathrm{TS} = 10\log_{10}\left(\frac{\sigma_{bs}}{1\ \mathrm{m}^2}\right). \tag{2.2}$$

The signal produced by a single-beam echosounder depends on the direction of the target as well as the backscattering cross section. The amplitude of a received signal is a function of the transducer beam pattern, the direction of the target must be measured so that the observed echo strength may be compensated by removing the beam pattern effect through a combination of physical and electronic means for each

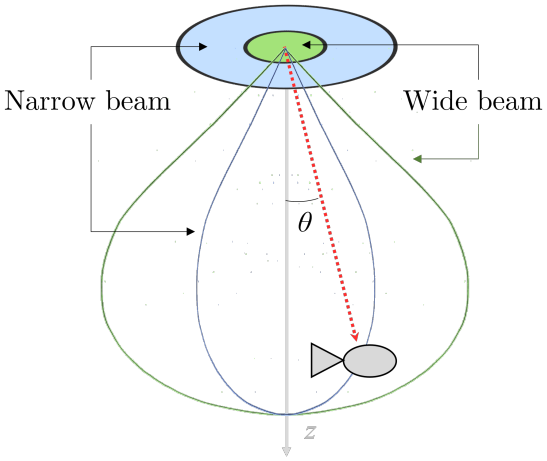

Figure 2.1: Principles of the dual-beam echosounder. The target direction is determined by echo intensity of the narrow beam receiver (illustrated in blue) and the wide beam receiver (illustrated in green).

individually resolved echo.

2.2 Dual-beam sonars

The first instrument developed for *in situ* direct target strength measurement was the dual-beam sonar. Ehrenberg (1974) suggested the potential effectiveness of the dual-beam sonar system as a means to measure the target strength of a scatterer. This is achieved by using a large circular transducer, which yields a narrow beam, and a smaller circular transducer at the centre of the previous one, which makes a wide beam as shown by Figure 2.1. The sizes of the two transducers are such that the narrow transducer acoustic beam has side lobes that overlaps the wide beam side lobes.

The pulse is transmitted by the entire transducer, therefore by the narrow beam,

and both small and large transducers act as independent receivers. The ratio of the echo intensities for the narrow and wide beam, described as I_{n} and I_{w} respectively, is used to compute the direction of arrival. As described by Simmonds and MacLennan (2005), the received intensity for each receiver depends on the direction of the target in the beam b_{n} and b_{w} and the backscattering cross-section. The intensities are then given by

$$I_{\mathrm{n}} = C_a \sigma_{bs} b_{\mathrm{n}}^2 \tag{2.3}$$

$$I_{\mathrm{w}} = C_a \sigma_{bs} b_{\mathrm{n}} b_{\mathrm{w}} \tag{2.4}$$

where C_a is the on-axis power sensitivity factor. Solving the equation for σ_{bs}, the backscattered cross-section is given as a function of the ratio of intensity such as

$$\sigma_{bs} = \left(\frac{1}{C_a}\right)\left(\frac{1}{b_{\mathrm{w}}^2}\right)\frac{I_{\mathrm{w}}^2}{I_{\mathrm{n}}}. \tag{2.5}$$

Because the target direction and b_{w} are functions of $I_{\mathrm{n}}/I_{\mathrm{w}}$, the backscattering cross-section, and therefore target strength, can be estimated using the intensity from both received signals.

2.3 Split-beam sonars

An alternative method of direct target strength measurement was developed in the following years from the dual-beam system. The alternative method, dubbed split-beam, consists of a transducer array of at least three elements to measure the three-dimensional position of the target and this information is used to remove the beam pattern effect from the target strength measurement.

The first split-beam echosounder was introduced with the Simrad ES380 in 1984. Although developed specifically for use by fishermen to provide estimation of both the abundance and sizes of fish, the potential of the split-beam instrument as a research tool was first explored by Foote, Kristensen, and Solli (1984) and Foote, Aglen, and Nakken (1986). In its simplest form, the concept is described by Foote as an idealized two point receiver system for which the angle of direction of arrival with boresight θ is given by equation

$$\theta = \begin{cases} \sin^{-1}(cT/d) \\ \pi - \sin^{-1}(cT/d) \end{cases} \tag{2.6}$$

where c is the sound speed of the medium, T is the time difference between the detection of the pulse between the two receivers, and d is the separation of the two receivers. Another way to write equation (2.6) is given by Ehrenberg and Torkelson (1996), given in terms of phase difference δ and wavelength λ for small angle approximation with equation

$$\theta = \sin^{-1}\left(\frac{\delta}{2\pi d/\lambda}\right) \approx \frac{\delta}{2\pi d/\lambda}. \tag{2.7}$$

Because the offset measurement of two signals can only be determined from -π to π, phase ambiguity can cause erroneous angular position measurement of a target. The system must be limited to ensure the measured angular position is within the main acoustic beam lobe where the measured phase difference has no phase ambiguity. For a simplified two element array, Foote mentions that the direction of arrival would be limited to a cone of the vertex angle

$$\theta_{\text{lim}} = \pi - 2\sin^{-1}(cT/d) \tag{2.8}$$

to avoid phase ambiguity. A hard threshold is used by setting any data recorded

past the -12 dB two ways beamwidth to zero in their field trials with the Simrad ES380 operated at 38 kHz to avoid ambiguity problems. The target strength was then compensated based on the measured beam pattern of the instrument. The trials concluded that the initial adaptation of the commercial split-beam echosounder was limited, but insightful information has been provided for the development of a research version of the ES380 to provide additional features, such as digitized signals.

Foote, Aglen, and Nakken (1986) present measurement of the mean *in situ* target strengths for six species of fish with a split-beam echosounder. In the following years, MacLennan and Svellingen (1989) explored calibration techniques for a split-beam echosounder and determined the sensitivity of the instrument to improve its accuracy for a research tool. Additional research such as Jones and Xie (1994) has been made on determining fish abundance from volume backscattering strength. With these advancements, split-beam systems can estimate the positions of individual echoes in dense schools, measure the fish density on long period of time, collect information about a fish's three-dimensional position and travel direction.

2.3.1 Directivity correction

In their field trials, Foote, Kristensen, and Solli (1984) notice an under-compensation of about 1.5 dB for the detections near 5° from the axis, which represents the -12 dB beamwidth. Because the beam pattern was measured along a single cut from the axis, the values in the compensation were not changed and showed discrepancy in the results.

In a following working paper, Foote (1986) addresses the under-compensation

problem in the previous field trials by theoretically investigating the beam patterns for two transducers to see how angle measurement resolution translates into TS resolution. By comparing a hexagonal shaped array of 68 elements at 38 kHz with a square shaped array of 36 elements at 70 kHz, the results show that the magnitudes of errors to the division of the beam angle are consistent with the manufacturer's nominal specification of ±0.375 dB accuracy. It is concluded that the removal of the bias from the instrument design is necessary to improve accuracy.

Ona (1990) explores calibration process for split beam echosounders including calibration of directivity compensation. They suggest a beam pattern function with an offset angle fitted to the data with estimated parameters:

$$D(\alpha,\beta) = 2^{-\left[\left(\frac{\alpha-\Delta\alpha}{\Phi_A}\right)^2+\left(\frac{\beta-\Delta\beta}{\Phi_B}\right)^2\right]^E} \tag{2.9}$$

where $\Delta\alpha$ and $\Delta\beta$ are the estimated athwartship and alongship angular offsets respectively, Φ_A and Φ_B are the estimated effective athwartship and alongship half power angles respectively, and E is the estimated shape parameter. With an offset angle between 0 and 0.25°, all the measurements fall within $\sim$ 0.3 dB, with 80% of the data within ± 0.1 dB, for all data within the -3 dB beamwidth. This equation also appears in Ona (1999), mentioning the directivity correction can either be made internally with the empirical function built to the Simrad EK500, or in post-processing with some software that finds the best fit for given parameters.

Jech et al. (2005) compare performance of two split-beams echosounders. Both the EK500 and Echoview software assume a small-angle approximation to define the beam pattern. They also mention an empirical compensation function derived by fitting a second-order polynomial to the alongship and athwartship angles and echo-strength

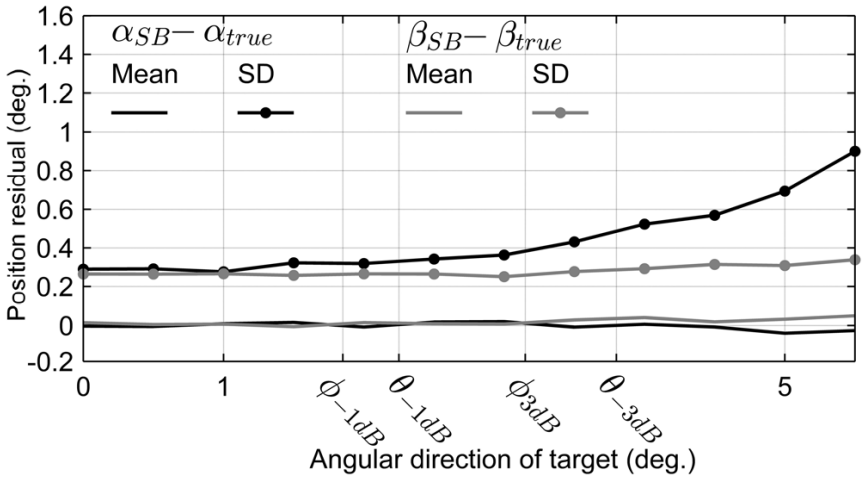

Figure 2.2: Mean position error (solid line) and its standard deviation (dotted) for horizontal (grey) and vertical (black) split-beam positioning of a target, for 100 iterations computed at each angular direction 0 to 5.5° with half-degree step. Reproduction of Figure 4 from Vatnehol and Ona (2017) with permission.

measurements:

$$\mathrm{D}(\alpha,\beta) = \mathrm{G} + \mathrm{c}_0\alpha + \mathrm{c}_1\alpha^2 + \mathrm{c}_2\beta + \mathrm{c}_3\beta^2 \tag{2.10}$$

where G is the overall echo-strength compensation value, and c_0, c_1, c_2, and c_3 are the empirically determined coefficients. Similarly to the method described by Ona, the compensation of the non-linear effects is done empirically in the beam pattern and the target strength compensation instead of correcting the measured angles.

Similar correction has been noticed in different transducer design, including a vertical cylindrical multi-beam array described by Vatnehol and Ona (2017). Figure 2.2 shows the angular measurement error increasing with the DOA in the split-beam algorithm. The split-beam accuracy is reduced with increasing off-axis DOA by ∼0.25° at the centre of the beam, ∼0.3° around -1 dB beamwidth, and ∼0.4° at -3

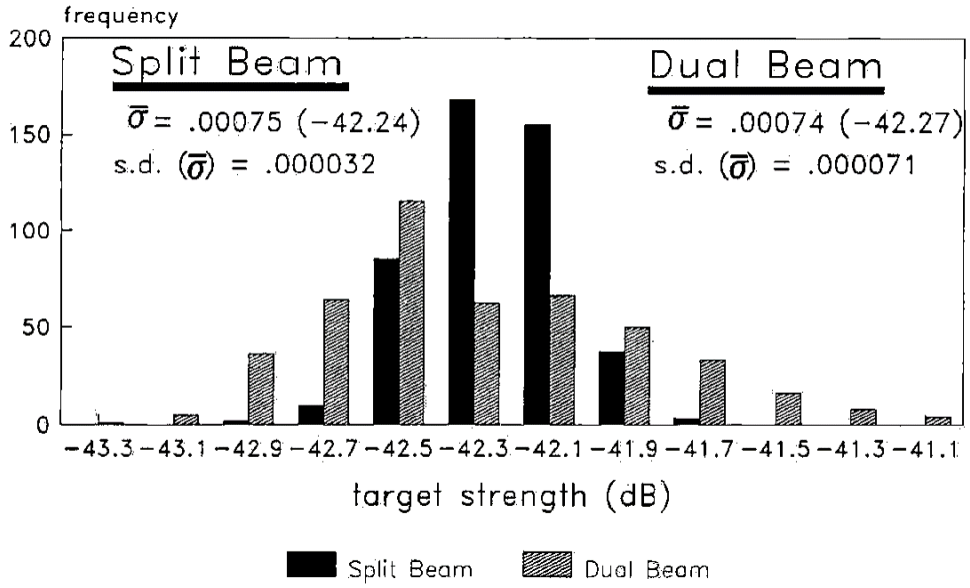

Figure 2.3: Comparison of target-strength measurements of calibrations using dual-beam and split-beam sonar techniques for a tungsten carbide sphere at 20 metres. Reproduction of Figure 5 from Traynor and Ehrenberg (1990).

dB beamwidth. In horizontal directions, the precision was $\sim$0.25° for all directions. Both split-beam and Interpolated Neighbouring Beam (INB) algorithms explored in the paper showed accuracy and precision reduced when the target is located further away from the beam centre. No attempt in improving the precision at large DOA is mentioned in the paper.

2.3.2 Comparison with dual-beam sonars

The split-beam method has been suggested by Traynor and Ehrenberg (1990) to be more accurate than the dual-beam sonar. Their experiment consisted of 460 repeated measurements of the target strength of the standard spherical target of -42.25 dB by using a transducer that can be used as both a dual-beam and a split-beam system.

The results, presented in Figure 2.3, show a better distribution of the target strength measurement for the split-beam system than the dual-beam sonar. They suggested the variability in dual-beam results were due to the noise which made the estimates of the direction of arrival less accurate with the method of evaluation.

Another advantage of the method of split beams over that of dual beams is the ability to measure the precise localization of scatterers in the beam. Surveys over individual fish can increase accuracy over the target strength measurement by mapping fish tracks through the beam, as well as a tool to study the general behaviour of the targets.

Chapter 3

MATLAB Sonar Model Description

A split-beam MATLAB model has been developed as a refinement of the existing Doppler sonar model described by Zedel (2008). The model is capable of simulating split-beam sonar operation based on acoustic backscatter theory of point scatterers in a three-dimensional domain. The objective of the model is to predict the performance accuracy of given designs, identify the limitations of the method, and optimize data processing techniques. As presented in Figure 3.1, the model configures a set of inputs, builds a signal over multiple pings, runs the signal through split-beam processing techniques, and presents the target strength measurement results.

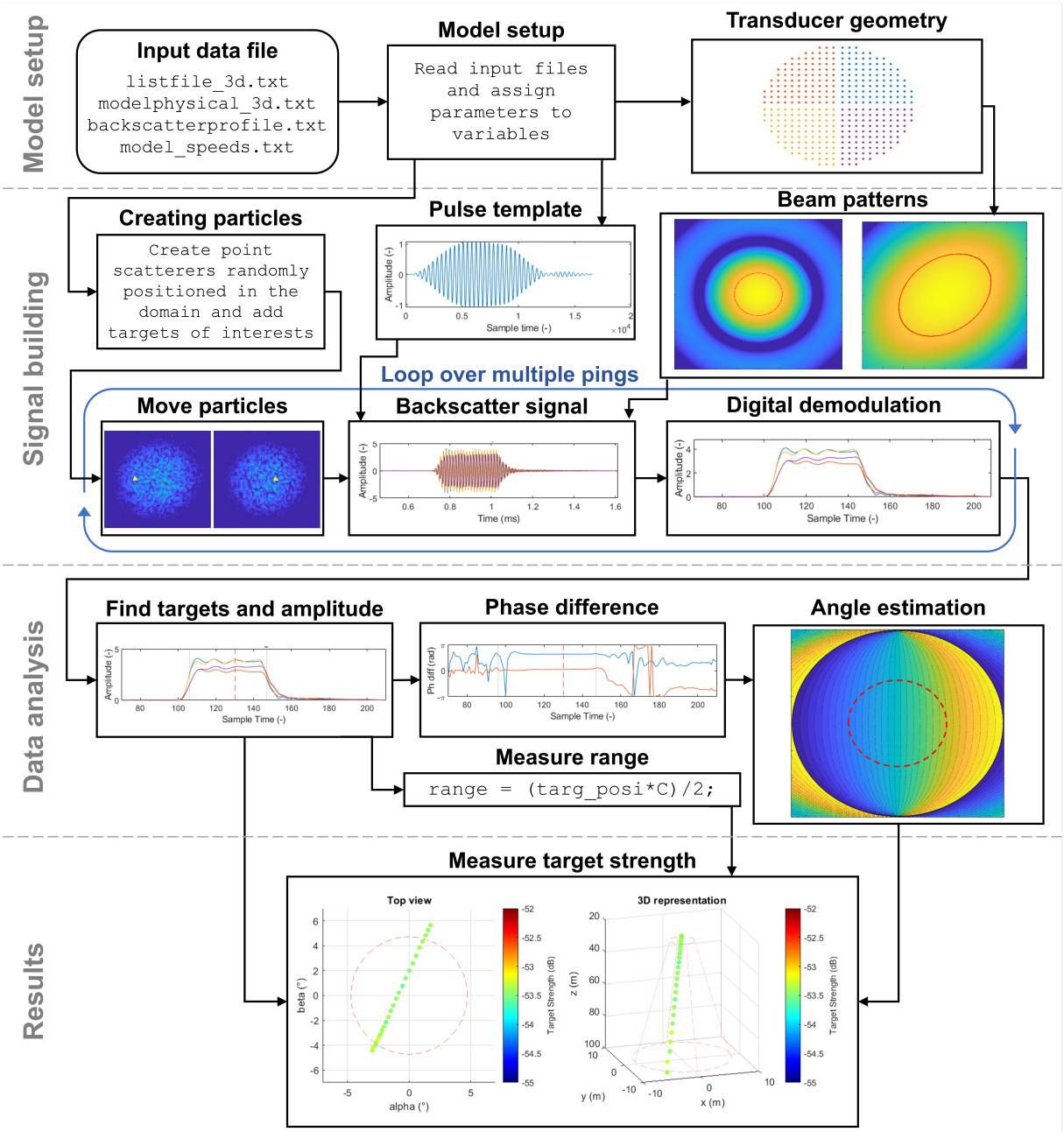

Figure 3.1: Bloc diagram of the model steps.

Parameter	Symbol	Value
Carrier frequency	f_c	70 kHz
Bandwidth	B	7 kHz
Pulse length	τ	500 μs
Model time step	$\mathrm{d}t$	3.7202381×10^{-8} s
Demodulation coefficient	κ	3
Sampling frequency	f_s	56 kHz
Transducer radius	a	0.066 m
Number of particles	n_i	300 particles
Number of pings	n_p	15 pings
Domain limits in x	$x_{\min}$, $x_{\max}$	$[-4, 4]$ m
Domain limits in y	$y_{\min}$, $y_{\max}$	$[-4, 4]$ m
Domain limits in z	$z_{\min}$, $z_{\max}$	$[10, 40]$ m

Table 3.1: List of parameters and example values assigned in the model setup.

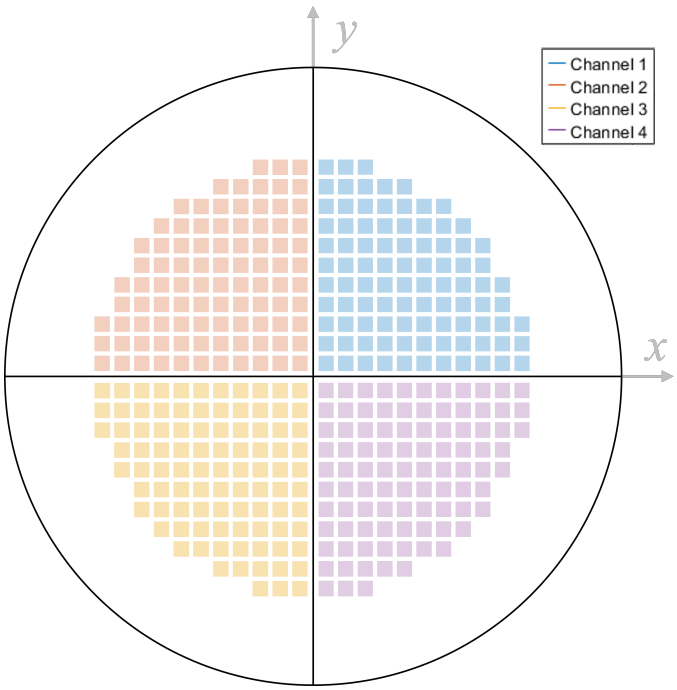

Figure 3.2: Schematics of the array of elements of the Airmar M475 split-beam transducer with channels numbering.

3.1 Model setup

3.1.1 Input files and variables

Input parameters for the transducer geometry, the pulse template, the model time step, the demodulation factor, the geometry of the domain, the number of particles, and the number of pings are imported from several text files and assigned to MATLAB variables. Table 3.1 shows some example values assigned to parameters as used for most of the present results presented unless marked otherwise.

3.1.2 Transducer geometry

The transducer in the model is meant to match the one used for the AZFP-Split prototype. The prototype used an Airmar M475 split-beam transducer (see Appendix A. for specifications). The transducer is made of 94 elements per quadrant, for a total of 376 elements. A MATLAB function generates a matrix of the 3D location of each element in the model domain. It is generated based on a radius of the array of elements. The results are shown by Figure 3.2.

Some information about the transducer can be extracted from theoretical equations. For a circular transducer of radius a, it has been determined that the formula to estimate the angular position of a target as described by equation (2.7) yields the best results when assuming a solution as a point receiver located at the geometric centre of the quadrant $4a/3\pi$. Therefore, the separation between the equivalent point transducers would be $d = 8a/3\pi$. The angular ambiguity limit of the system would then be described as

$$\theta_{\text{lim}} \approx \arcsin\left(\frac{3\pi^2}{8ka}\right) \tag{3.1}$$

where k is the wavenumber. Additionally, it is possible to get information on the half-power limit. When solving the directivity equation of a circular transducer for the -3 dB beamwidth, the half-power angle $\theta_{-3\text{dB}}$ for a one-way beam is given by

$$\theta_{-3\text{dB}} = \arcsin\left(\frac{1.61636}{ka}\right). \tag{3.2}$$

For a two-way beam, the equation becomes

$$\theta_{-3\text{dB}} = \arcsin\left(\frac{1.16029}{ka}\right). \tag{3.3}$$

These standard reference values are used to predict and understand the performance and limitation of a given transducer.

3.2 Modelling acoustic backscatter signal

3.2.1 Creating particles in the domain

Transmitted sound is scattered by particles or inhomogeneities in the water. The size, number, and spatial configuration of these scatterers determine the amplitude and phase of the signal at the receivers. The model simulates such event by having n_i point scatterers randomly positioned in a domain in an even distribution in a three-dimensional space. The distribution is achieved by assigning each particle a random number within the domain determined by $[x_{\min}, x_{\max}]$, $[y_{\min}, y_{\max}]$, and $[z_{\min}, z_{\max}]$.

The targets of interest (TOI) are then added by changing the position and amplitude contribution to a number of particles to a predetermined x, y and z position values, as well as a relative amplitude value to every particle assigned to be a TOI from an input file. For TOI in the farfield, the distance is judged to be sufficient to justify the use of point scatterers as a good estimation for target strength measurement without need to model complex acoustic structure for targets, such as fish swimbladders.

3.2.2 Moving particles

All particles in the domain move between each ping to represent the effect of velocity. Adding movement between pings allows to measure target strength of the TOI in

different positions as they move through the domain or as the sonar system drifts. As described by Zedel (2008), the position of the j-th particle at time t_i defined by $\mathbf{X}_j(t_i)$ is updated at time $t_i + 1$ with equation

$$\mathbf{X}_j(t_i + 1) = \mathbf{X}_j(t_i) + \mathbf{V}_j[\mathbf{X}_j(t_i)](t_{i+1} - t_i) + \Gamma_v[\mathbf{X}_j(t_i)](t_{i+1} - t_i) \tag{3.4}$$

where $\mathbf{V}_j[\mathbf{X}_j(t_i)]$ is the particle velocity at position $\mathbf{X}_j(t_i)$, and $\mathbf{\Gamma}_v$ is a random vector with mean zero and standard deviation assigned for the velocity. This equation is computed using the x, y and z position for assigned velocity from an input file before the signal building of every ping.

3.2.3 Signal building

The simulated signal is assembled by assigning a pulse template $s(t)$ of an amplitude in time calculated by the position of each particle in the domain. The template is constructed with a sinusoidal signal at the carrier frequency. It is then filtered using a rational transfer function defined by the coefficients of a Butterworth IIR filter based on the bandwidth and the pulse length. As shown in Figure 3.3 **a)**, the filter also creates a resonance after the main pulse, because the filter has a finite bandwidth that cannot eliminate all frequencies. The result shows up as a ripple in the signal after the transmit pulse. This ripple naturally occurs in transducers, as transducers cannot project all frequencies.

Based on the model presented by Zedel (2008), the acoustic backscattered signal is constructed as a sum of pulse template such as

$$S(t) = \sum_{i=1}^{n_i} A_i s\left(t - \frac{(r_{si} + r_{ri})}{c}\right) \tag{3.5}$$

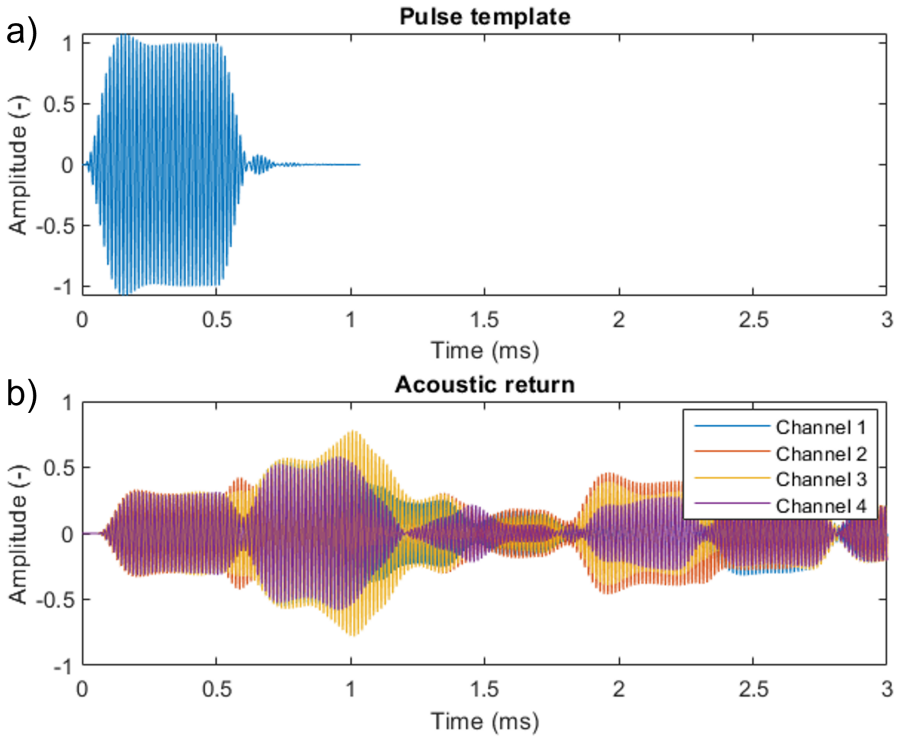

Figure 3.3: Example of model pulse template (**a)**) and one realization of an acoustic return of point scatters randomly positioned in the domain for the four receivers (**b)**).

where the summation is over all particles in the model domain, A_i the backscatter amplitude of the i'th point scatterer measured with the position in the beam patterns, $s(t)$ is the transmit pulse template, t is the time since pulse transmission, and r_{si} and r_{ri} are source-to-target and target-to-receiver distances, and c is the speed of sound in water. This summation needs to be done for each quadrant receiver. An example of a pulse template and an acoustic return is shown by Figure 3.3 **b)**.

The Doppler shift based on the particles velocity is also considered in the signal building, although the impact in the position and TS measurement has not been explored in depth. Following Zedel (2015), the time dilation that occurs when sound is scattered from a moving target can be expressed as

$$t' = t\,(1 - 2V_r/c) \tag{3.6}$$

where t is the time reference for the transmitted pulse, and V_r is the measured component of velocity.

Random noise signal is also added to the signal $S(t)$ simulating acoustic or electronic noise. However, the impact of signal-to-noise ratio from random noise signal over the target strength measurement has not been explored thoroughly as part of this project.

3.2.4 Beam pattern

For each particle in the domain, the total backscatter amplitude A_i is given by the product of the amplitude of the target with the transmitter beam pattern A_{si} and the amplitude with the receiver beam pattern A_{ri} such as

$$A_i = A_{si}A_{ri}. \tag{3.7}$$

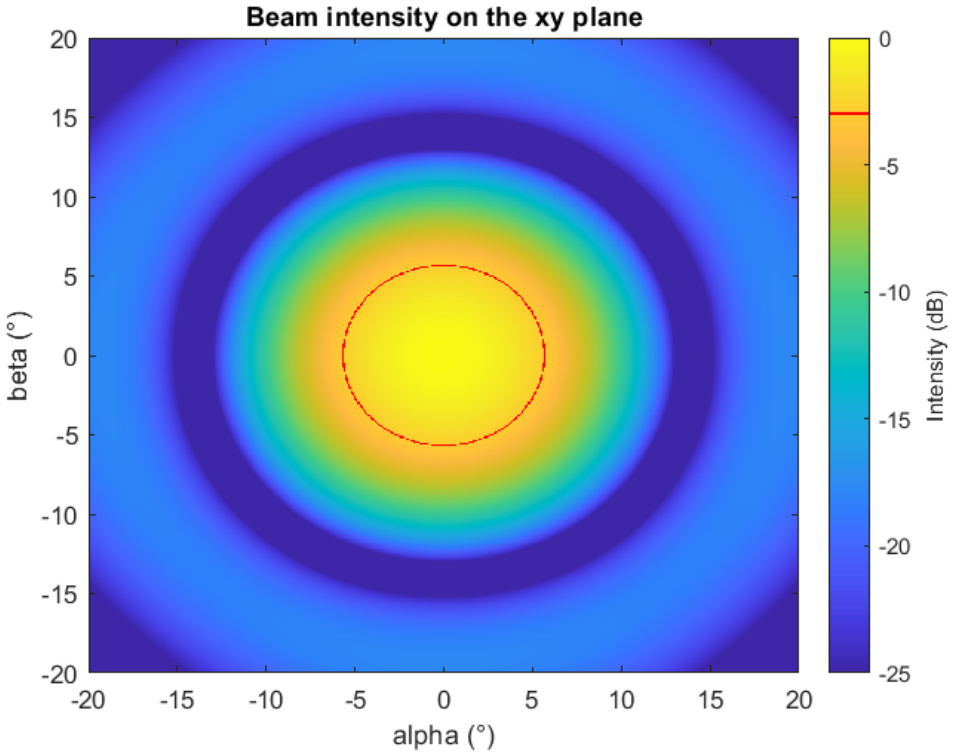

Figure 3.4: Beam pattern of a circular piston transducer in the farfield shown on the xy plane. The red line represent the -3 dB beamwidth.

This value is used to determine the amplitude of the pulse template $s(t)$ for each particle and for all four receivers.

3.2.4.1 Transmitter beam pattern

The transmit pulse of the system is generated by all four quadrants of the transducer transmitting simultaneously. Medwin and Clay (1998), provides an equation for the directional response $D(\theta)$ with a circular piston transducer in the farfield at an angle θ with respect to the acoustic axis given by

$$D(\theta) = \frac{2J_1\left(ka\sin\theta\right)}{ka\sin\theta} \tag{3.8}$$

where k is the wavenumber of the pulse, a is the radius of the transducer, and $J_1(x)$ is the first-order Bessel function.

Transmission loss from spreading losses and attenuation must be accounted in the intensity measurement. As the wavefronts travel outwards from the transducer, they spread over a larger area. Because the total energy is constant, the intensity decreases as the beam spreads with the range r_{si} in accordance with the inverse-square law. The directional response is now given by

$$D(\theta, r_{si}) = \frac{D(\theta)}{r_{si}^2}. \tag{3.9}$$

Next, the absorption loss is taken into account in the amplitude. A molecular relaxation phenomenon is caused by the relatively small amounts of magnesium sulfate salts and boric acid in sea water, moderated by the pH of the sea water. This relaxation process causes the absorption of sound at specific ranges of frequency. Based on equation (3.4.29) of Medwin and Clay (1998), the absorption coefficient α_c is given by

$$\alpha_c = \frac{A_1 P_1 f_1 f^2}{f^2 + f_1^2} + \frac{A_2 P_2 f_2 f^2}{f^2 + f_2^2} + A_3 P_3 f^2. \tag{3.10}$$

The first term is the boric acid component in sea water, the second one is the magnesium sulfate component in sea water, and third is the pure water component assuming a temperature of $T = 10^\circ$ C. All the coefficient values are taken from Medwin and Clay (1998). Accounting for the absorption loss, the amplitude response for the transmitter beam pattern A_{si} is given by the beam pattern $D(\theta, r_{si}, \alpha_c)$ such as

$$A_{si} = D(\theta, r_{si}, \alpha_c) = D(\theta, r_{si}) 10^{-\alpha_c r_{si}/20}. \tag{3.11}$$

The intensity of the beam pattern is plotted using the magnitude squared of the directivity, $|A_{si}|^2$, shown by Figure 3.4. The red lines in this figure represent the

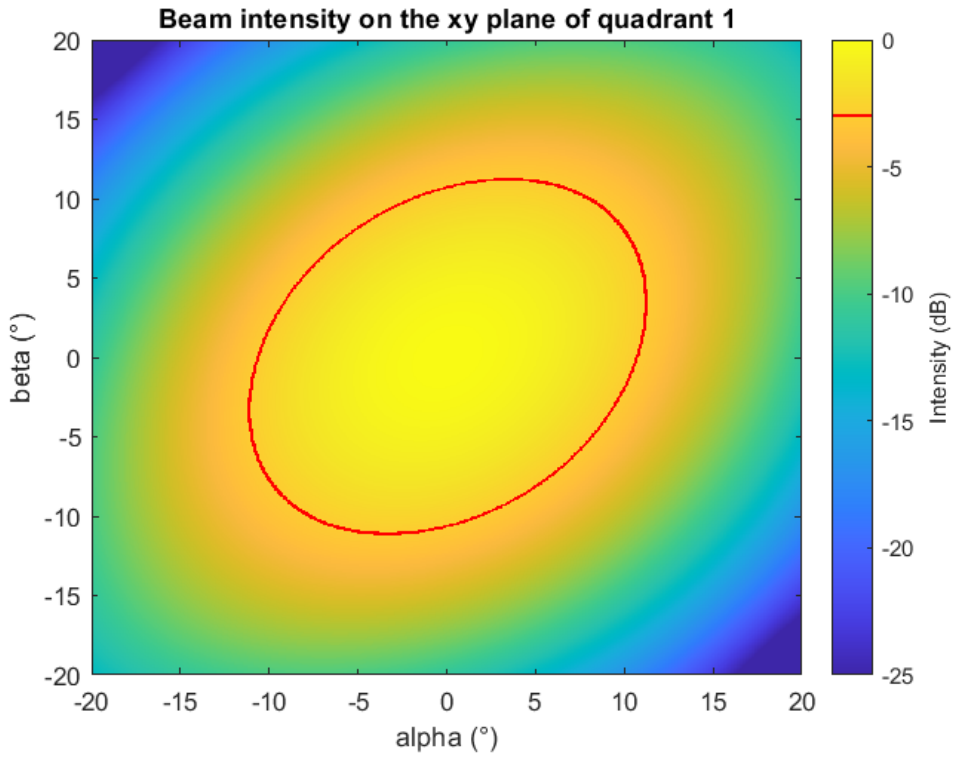

Figure 3.5: Beam pattern of a quadrant shaped transducer in the farfield shown on the xy plane. The red line represent the -3 dB beamwidth.

half-power beamwidth, or -3 dB beamwidth. This nominal designation of an instrument beamwidth based on its amplitude is used as an indication of the instrument limitation, although information outside of this limit is also part of the received signal.

3.2.4.2 Receiver beam pattern

Because the four quadrants of the transducer act as independent receivers, a model for a quadrant shaped transducer is needed to compute its amplitude response. A quadrant shaped transducer of radius a is generated and the surface is divided into subareas. Each of these subdivisions contribute to the directivity response of the transducer. The range r_{qi} of the i-th particle at coordinates x_i, y_i and z_i is calculated

with the Euclidean distance:

$$r_{qi} = \sqrt{(x_i - x_0)^2 + (y_i - y_0)^2 + (z_i - z_0)^2} \tag{3.12}$$

where x_0, y_0 and z_0 are the coordinates of the subdivision on the surface of the transducer.

The amplitude response of the distance of each point in space is given by:

$$D(ri) = \frac{1}{N} \sum_{n=1}^{N} \frac{g_n e^{ikr_{qi}}}{r_{qi}} \tag{3.13}$$

where N is the number of subdivisions on the surface of the quadrant-shaped transducer and g_n is the amplitude contribution of each subdivision. To match the amplitude of the transmitter, the sum needs to be normalized by dividing by N.

Similarly to the description given in the section 3.2.4.1, the transmission and absorption loss is considered in the amplitude with (3.9) and (3.11) using the range of the i-th particle with the centre of the receiver r_{ri}. The resulting receiver beam pattern amplitude A_{ri} is given by

$$A_{ri} = D(r_{qi}, r_{ri}, \alpha_c) = D(\theta, r_{ri}) 10^{-\alpha_c r_{ri}/20}. \tag{3.14}$$

The intensity of the beam pattern including spreading and attenuation loss $|A_{ri}|^2$ as shown by Figure 3.5.

3.2.4.3 Mapping phase

The distance from the transmitter to the scatterer and on to the receiver introduces a time delay or phase shift relative to the modelled source template. The phase offset is represented by introducing a complex number to the amplitude computation of each particle in both the transmitter and receiver beams. The absolute value of this

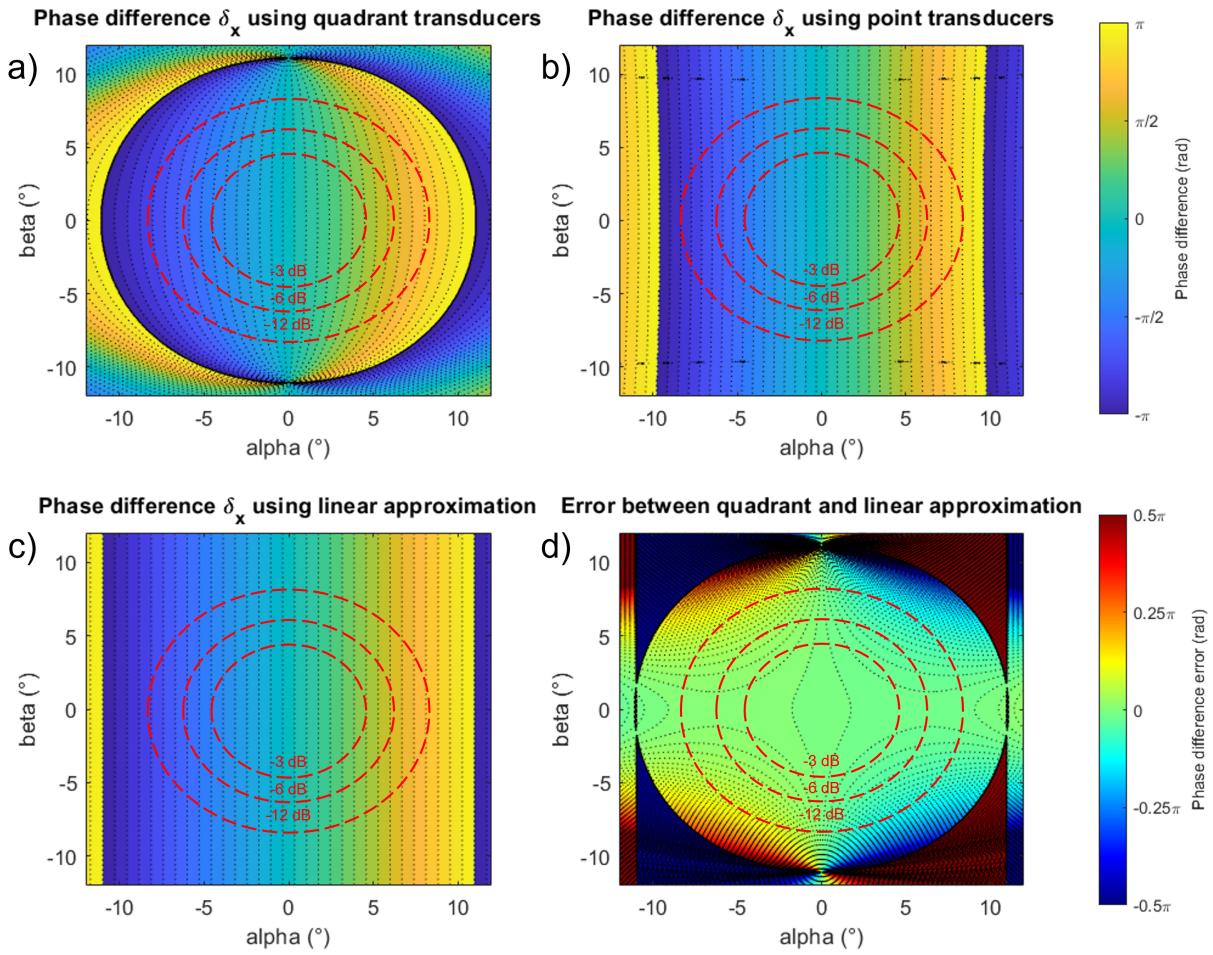

Figure 3.6: Phase difference map in the farfield by comparing the absolute phase using **a)** the pairs of quadrant-shaped transducers, **b)** the pairs of point transducers located at the centroid, **c)** the linear approximation equation. **d)** represent the difference between **a)** and **c)**. The dashed red circles represents the -3, -6, and -12 dB beamwidth.

complex number provides the intensity of the beam pattern at the location in space, while the argument provides the absolute phase. It is then possible to look at the difference in absolute phase between two beam patterns to create a map of expected phase difference value for any point in the domain. Figure 3.6 **a)** shows the difference between the argument of the sum of quadrants 1 and 4, and the argument of the sum of quadrants 2 and 3. This provides a map of phase difference value on the x axis, defined as δ_x that can be expected by a target in the farfield. A similar figure, rotated by 90°, can be obtained for δ_y by comparing the pairs of transducers on the y axis.

Similarly, phase difference maps can be generated using point transducers, providing an almost linear phase map, as shown by Figure 3.6 **b)**. Studying the geometry with the beam pattern model proved that the best approximation of the quadrant transducer phase map is by using a point transducer located at the geometric centroid of a quarter-circular area, or $4a/3\pi$, where a is the radius of the circular transducer. This happens to provide very similar phase difference values in the farfield as using the linear approximation of the angular direction of a target from the detected phase difference, described by equation (2.7), as shown by Figure 3.6 **c)**. Comparison of Figure 3.6 **a)** and **c)** shows there are offsets in phase difference between using a linear approximation and the actual phase difference expected from quadrant-shaped transducers. This difference is shown in Figure 3.6 **d)**, where the difference is up to 0.04π within the -3 dB beamwidth, and up to 0.3π within the -12 dB beamwidth.

3.2.5 Digital demodulation

The model time step is set to a small enough value to provide the necessary resolution in phase and range. However, the information can be preserved at much lower sampling rate without aliasing the signal. According to Nyquist sampling theorem, converting a signal into a sequence of values necessitates a sufficient condition for a sample rate that permits a discrete sequence of samples to capture all the information from a continuous-time signal of finite bandwidth. As described by Shannon (1949), the theorem states:

> If a function $f(t)$ contains no frequencies higher than W Hz, it is completely determined by giving its ordinates at a series of points spaced $1/2W$ seconds apart.

In the context of sonar signal processing, this means the sampling of the received signal must be made at over twice the carrier frequency to avoid aliasing. However, sampling at such high frequency can be power consuming, require larger data storage, and thus limit long-term application.

Decimation, or downsampling, is the process of re-sampling the signal at a lower rate. A non-aliasing decimation can be achieved in a way the information on amplitude and phase is preserved as long as the chosen sampling frequency is more than twice the transducer bandwidth. Lyons (2011) presents a method of decimation using spectral inversion. To choose the right re-sampling frequency f_s, it is necessary to use a value of sampling rate that forces the sampled spectra to be centred exactly at $\pm f_s/4$. This process is achieved by selecting the re-sampling frequency f_s using

equation (2-11) from Lyons (2011), which is given by

$$f_s = \frac{4f_c}{2\kappa - 1} \tag{3.15}$$

where κ is a positive integer, and f_c is the centre frequency of the original signal. To ensure the integer κ for which the sampling frequency is over twice the transducer bandwidth, we have to use equation (2-10) from Lyons (2011) expressed as

$$\frac{2f_c - B}{m} \geq f_s \geq \frac{2f_c + B}{m + 1} \tag{3.16}$$

where B is the bandwidth of the receiver and m is an arbitrary, positive integer ensuring that $f_s \geq 2B$. Some of the permissible f_s values from this equation will provide a sampled baseband spectrum located near 0 Hz. The positive frequency sampled baseband will have the inverted shape of the negative half from the original signal spectrum, which happens whenever m is an odd integer. When the original positive spectral bandpass components are symmetrical about the carrier frequency, any non-aliasing value for f_s may be chosen for the spectral inversion. A table of value of m can be made, and a value of f_s can be chosen with inequality (3.16), as shown by Table 3.2. We can then solve equation (3.15) to determine the integer κ that provides the closest f_s value within the constraint of the inequality (3.16).

The sampling period of the sampling frequency f_s is then given by $t_s = 1/f_s$, and the digital demodulation rate $\mathrm{d}t_s$ is given by

$$\mathrm{d}t_s = \frac{t_s}{\mathrm{d}t} \tag{3.17}$$

where $\mathrm{d}t$ is the time step of the model. Therefore, the decimation saves one data point every $\mathrm{d}t_s$ point. From there, every other data point of the downsampled signal can then be split into in-phase $I(t)$ and quadrature $Q(t)$ sizedecimated samples, as shown

m	$2f_c - B/m$	$2f_c + B/m + 1$
1	133 kHz	73.5 kHz
2	66.5 kHz	49 kHz
3	44.33 kHz	36.75 kHz
4	33.25 kHz	29.4 kHz
5	26.6 kHz	24.5 kHz

k	f_s
1	280 kHz
2	93.33 kHz
3	56 kHz
4	40 kHz
5	31.11 kHz

Table 3.2: Example of (3.16) and (3.15) with $f_c = 70$ kHz and $B = 7$ kHz.

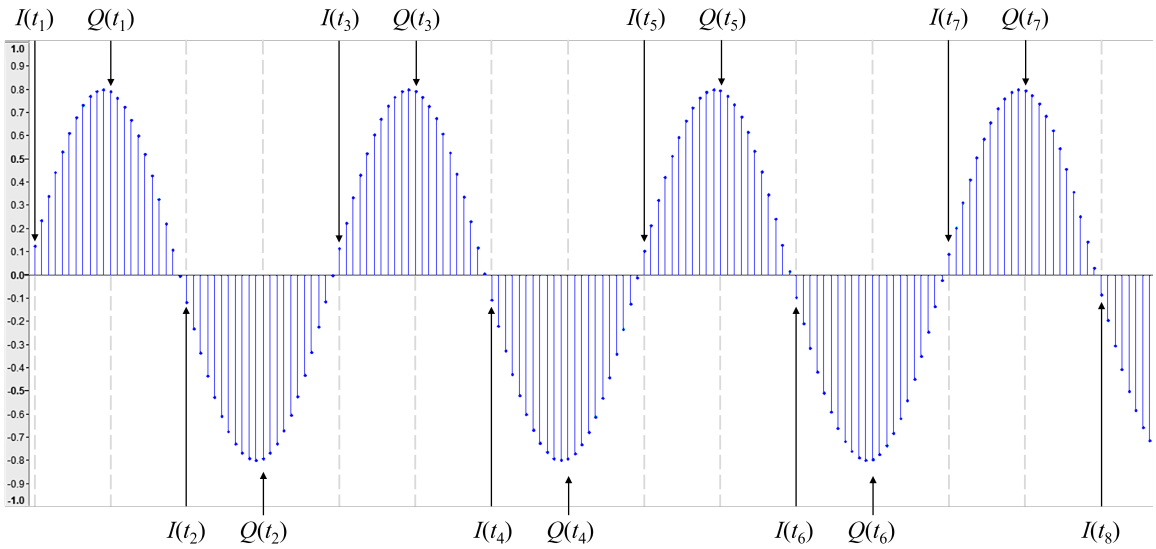

Figure 3.7: Demonstration of the in-phase and quadrature sampling with $\mathrm{d}t_s = 11$.

by Figure 3.7. Every other point of both the in-phase and quadrature sizedecimated samples then needs to alternate the plus ones and minus sign such as $(-1)^n$. By setting the in-phase samples to the real value and the quadrature samples to imaginary numbers, the result is a complex demodulated signal that preserves the echo intensity and the phase of the signal given by

$$C(t) = I(t) + iQ(t). \tag{3.18}$$

The amplitude of the signal is obtained from the absolute value of the complex number, $|C(t)|$, and the phase is obtained from its argument, $\mathrm{Arg}\,(C(t))$. A comparison between the original signal and the demodulated signal, shown with the absolute value $|C(t)|$ and the argument $\mathrm{Arg}\,(C(t))$, is shown by Figure 3.8. The variation in phase is caused by the low amplitude particles acting as background noise, implementing a chaotic phase behaviour in low amplitude regions of the signal. By identifying the TOI in the signal from the echo intensity, the phase shows a stable region of a length of τ.

3.3 Data processing algorithm

With a signal built and downsampled, the information can be extracted from post-processing data analysis tools. The TOI are identified from the signals for each ping. To compute the target strength, requires knowledge of the intensity, range, and position of each TOI for every ping.

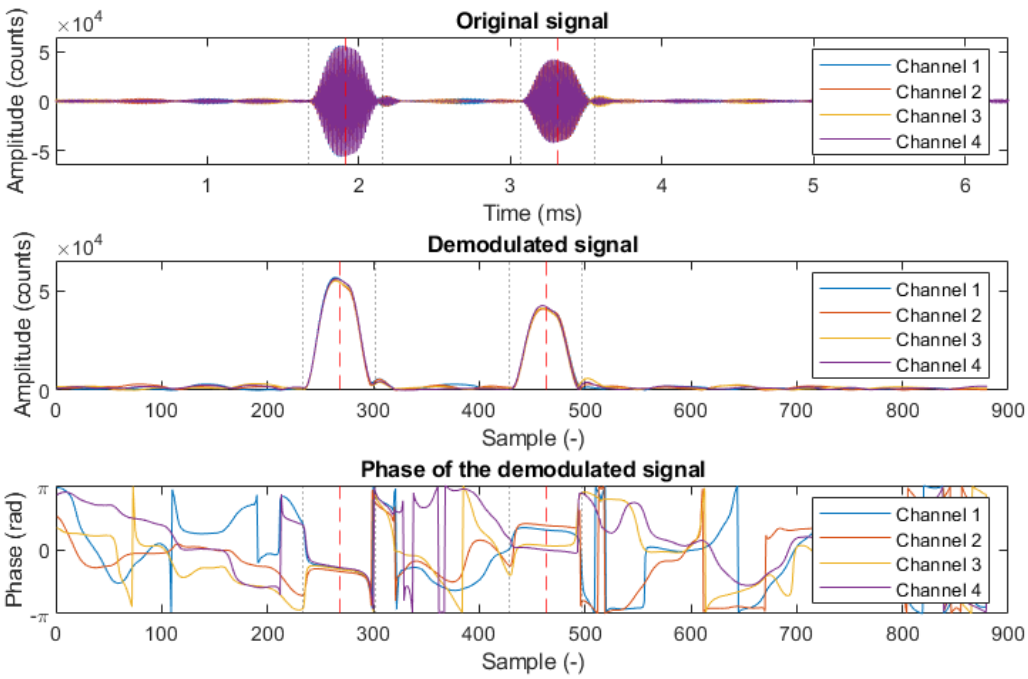

Figure 3.8: Representation of the real signal, amplitude and phase of the digital demodulation with a rate of $\mathrm{d}t_s = 96$ with two TOI in the domain identified with red dashed lines.

3.3.1 Target detection and intensity measurement

There are many methods of detecting a TOI in the signal. In the model, the method of choice is an easy and efficient way to detect TOI in the signal by looking at the convolution of the demodulated signal $C(t)$ and the demodulated pulse template $c(t)$. An arbitrary threshold is set to eliminate false positive in the noise, and the local maxima of the convolution is located at t_{e}.

$$t_{\mathrm{e}} = t\left(\max\left\{C(t) * c(t)\right\}\right) \tag{3.19}$$

An alternative method to detect targets that was used in the field trials signals is from the transducer phase differences. Because the phase difference stabilizes on the location of the targets in the signal, it is possible to search for regions in the signal with small phase difference variability over the duration of the pulse length providing a detection method that does not rely on the intensity of the signal nor the convolution with the pulse template. This method is an effective way to filter the recorded data, making it easier to manually pinpoint the TOI in each ping.

The echo intensity I is measured for all four channels at t_{e} using the max value within the pulse length such as

$$I = \max\left\{C\left(\left[t_{\mathrm{e}} - \frac{\tau}{2}, t_{\mathrm{e}} + \frac{\tau}{2}\right]\right)\right\}. \tag{3.20}$$

3.3.2 Range measurement

The measurement of the range of a TOI is a straight forward process. Because the pulse goes back and forth from a transducer to a target at a given speed, the range can be evaluated from the speed of sound in the water. The range of a target r is

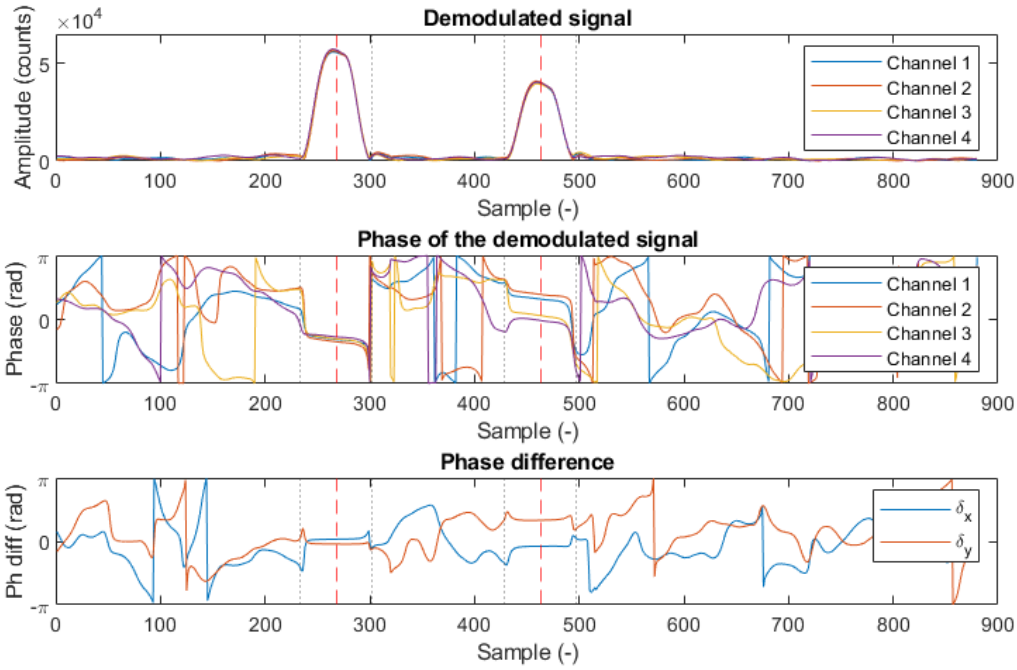

Figure 3.9: Representation of the demodulated signal, the phase of each channel and the phase difference with two TOI in the domain identified with red dashed lines.

defined by

$$r = \frac{ct_e}{2} \tag{3.21}$$

where c is the speed of sound, and t_e is the measured time of the received TOI echo since the pulse transmission. For real life applications, the speed of sound needs to be estimated for the area of the measurement using instruments such as a CTD profiler. For simplicity, c is set as a constant of 1475 m/s in the simulations.

3.3.3 Phase difference measurement

Four different methods to measure the phase shift between the received signals have been explored.

1. The phase difference of the TOI located at $t = t_e$ can be obtained from the real signal $S(t)$ by using the difference between the arguments of the FFTs of the pairs of channels.

$$\delta_x = \mathrm{Arg}\left[\mathcal{F}\{S_1(t_e) + S_4(t_e)\}\right] - \mathrm{Arg}\left[\mathcal{F}\{S_2(t_e) + S_3(t_e)\}\right] \tag{3.22}$$

$$\delta_y = \mathrm{Arg}\left[\mathcal{F}\{S_1(t_e) + S_2(t_e)\}\right] - \mathrm{Arg}\left[\mathcal{F}\{S_3(t_e) + S_4(t_e)\}\right] \tag{3.23}$$

2. Using the cross correlation ($\star$) of the pairs of real signal $S(t)$, the lag between the signal can be obtained. The lag value in samples can be transformed into a time value or a phase shift value.

$$\delta_x = 2\pi f_c \mathrm{d}t\, \mathrm{Lag}\left[(S_1(t_e) + S_4(t_e)) \star (S_2(t_e) + S_3(t_e))\right] \tag{3.24}$$

$$\delta_y = 2\pi f_c \mathrm{d}t\, \mathrm{Lag}\left[(S_1(t_e) + S_2(t_e)) \star (S_3(t_e) + S_4(t_e))\right] \tag{3.25}$$

3. Using the demodulated signal, the argument of the complex number $C(t)$ is the phase of the signal. The expected phase shift can be obtained from the difference between the sum of the pairs of phase value at a given point in the demodulated signal.

$$\delta_x = \mathrm{Arg}\left[C_1(t_e) + C_4(t_e)\right] - \mathrm{Arg}\left[C_2(t_e) + C_3(t_e)\right] \tag{3.26}$$

$$\delta_y = \mathrm{Arg}\left[C_1(t_e) + C_2(t_e)\right] - \mathrm{Arg}\left[C_3(t_e) + C_4(t_e)\right] \tag{3.27}$$

4. The phase difference can be obtained using the argument of the cross correlation with the pairs of complex demodulated signals $C(t)$.

$$\delta_x = \mathrm{Arg}\left[(C_1(t_e) + C_4(t_e)) \star (C_2(t_e) + C_3(t_e))\right] \tag{3.28}$$

$$\delta_y = \mathrm{Arg}\left[(C_1(t_e) + C_2(t_e)) \star (C_3(t_e) + C_4(t_e))\right] \tag{3.29}$$

Methods 1 and 2 were explored to compare the effect of digital demodulation on the phase difference measurement, but were not considered to be used for data sampled at smaller frequency than the carrier. The most accurate algorithm for the demodulated signal $C(t)$ happens to be the argument of the cross correlation with the pairs demodulated signals. The phase difference for a simulated signal is represented in Figure 3.9.

3.3.4 Angular position measurement

With the TOI identified in the signal and the phase difference between the pairs of quadrant receivers measured, the angular position of the TOI can be estimated. With the phase difference of the pairs of quadrants on the x-axis, marked as δ_x, the angle α of the fish with the vertical acoustic axis can be retrieved. Similarly, the phase difference for the other pairs of quadrants, marked as δ_y, provides the angle β. Two methods to retrieve the angular position from the phase differences are explored and compared.

3.3.4.1 Linear method

Foote, Kristensen, and Solli (1984) show use of a linear approach to measure the angular position of a target from the phase difference. As shown in Figure 3.10, the linear approach is achieved by approximating the receivers as point transducers separated by a distance d. Based on Ehrenberg and Torkelson (1996), the equations to measure angular position α from the phase difference δ_x and the angle β from δ_y

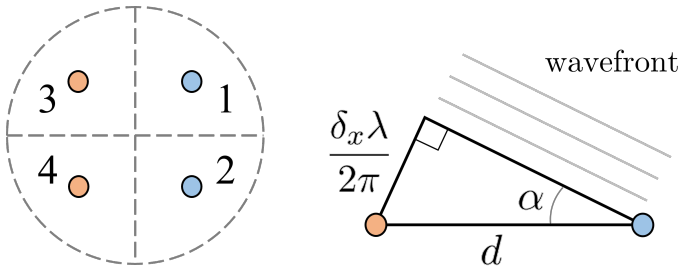

Figure 3.10: Approximating receivers as point transducers to evaluate the angle α of the wavefront with the surface of the transducer.

are given by

$$\alpha\left(\delta_x\right) = \arcsin\left(\frac{\delta_x \lambda}{2\pi d}\right) \approx \frac{\delta_x \lambda}{2\pi d} \tag{3.30}$$

$$\beta\left(\delta_y\right) = \arcsin\left(\frac{\delta_y \lambda}{2\pi d}\right) \approx \frac{\delta_y \lambda}{2\pi d} \tag{3.31}$$

The point transducers are assumed for convenience to be at the geometric centroid of the quadrant transducer, which is located at $4a/3\pi$ with a being the radius of the transducer. This geometry allows the directional ambiguity to be outside the half-power beamwidth for any value of a or λ.

A map of the expected phase difference in x for any point in the far field by using the linear approximation is presented by Figure 3.6 **c)**. By symmetry, a similar but horizontal gradient is obtained for the phase difference map in y.

3.3.4.2 Polynomial method

A beam pattern for a quadrant shaped transducer has been modelled. It is then possible to obtain an accurate phase map that accounts for a quadrant shaped transducer instead of a point element. By taking the argument of the complex value of the pairs of beam patterns on the x axis such as $\mathrm{Arg}(S_1 + S_2) - \mathrm{Arg}(S_3 + S_4)$, the phase map

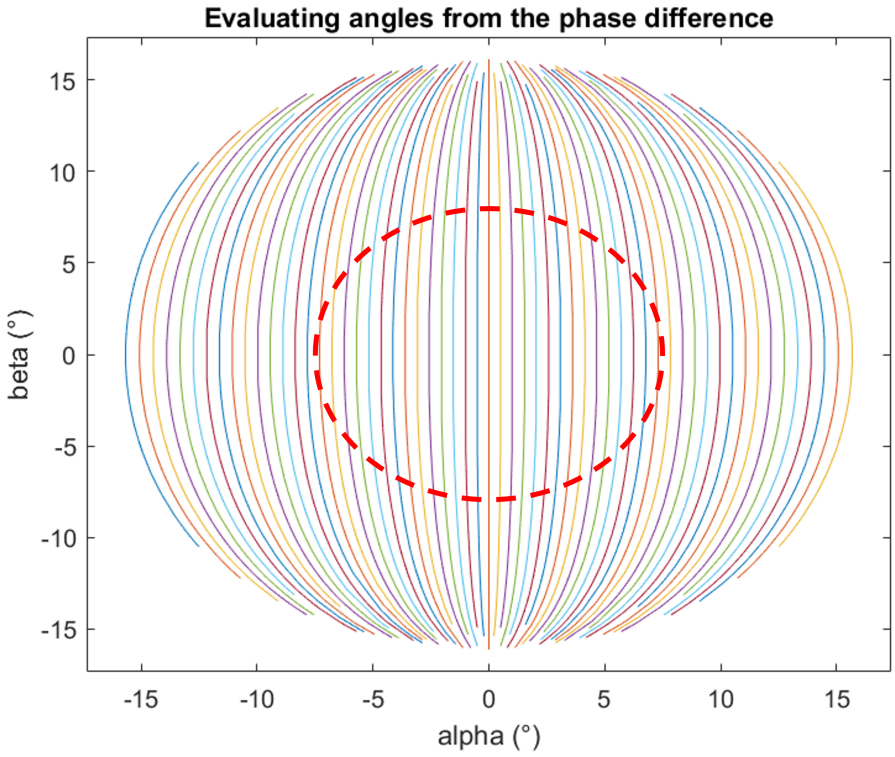

Figure 3.11: Phase difference map in the far field by comparing the absolute phase of the pairs of quadrant-shaped transducers with discrete phase differences value from $-\pi$ to π. The dashed red circle represents the -3 dB beamwidth.

shown by Figure 3.6 **a)** is formed. By symmetry, a similar but horizontal gradient is obtained for the phase difference map in y.

An alternative method that accounts for the non-linearity in the phase map has been developed. Going back to Figure 3.6 **a)**, we can establish a series of discrete phase differences value from $-\pi$ to π inside the limits of ambiguity, defined by angle θ_{lim}. This process is represented by Figure 3.11. Each of these lines can be represented as an equation for the angle α as a function of β such as

$$\alpha(\beta) = \boldsymbol{a}\beta^4 + \boldsymbol{b}\beta^2 + \boldsymbol{c} \tag{3.32}$$

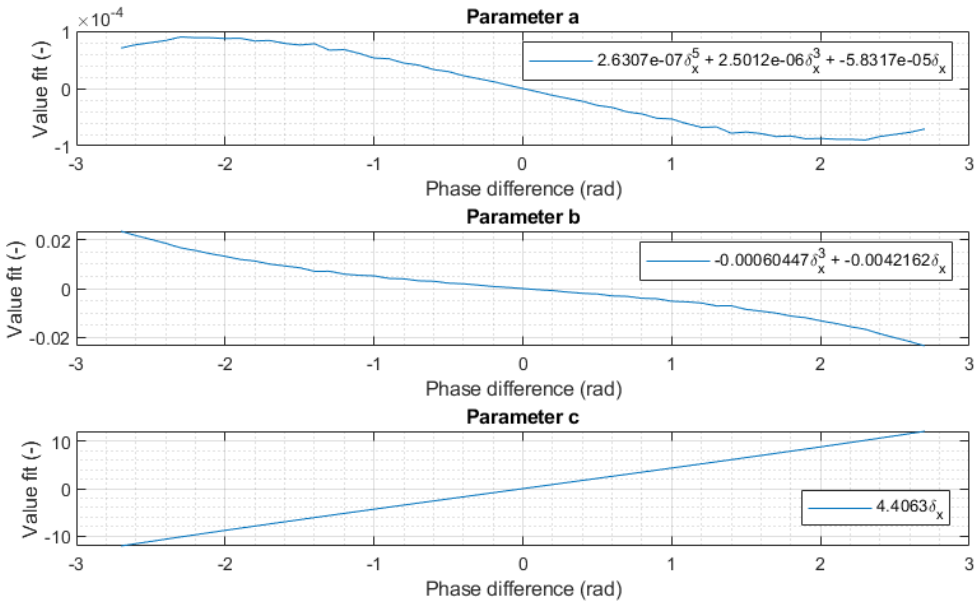

Figure 3.12: Curve fit over parameters $\boldsymbol{a}(\delta_x)$, $\boldsymbol{b}(\delta_x)$ and $\boldsymbol{c}(\delta_x)$.

where $\boldsymbol{a}$, $\boldsymbol{b}$ and $\boldsymbol{c}$ are parameters given by the measured phase difference. These parameters can be seen as functions of the phase difference given by

$$\boldsymbol{a}(\delta_x) = \boldsymbol{A}\delta_x^5 + \boldsymbol{B}\delta_x^3 + \boldsymbol{C}\delta_x, \qquad \boldsymbol{b}(\delta_x) = \boldsymbol{D}\delta_x^3 + \boldsymbol{E}\delta_x, \qquad \boldsymbol{c}(\delta_x) = \boldsymbol{F}\delta_x \tag{3.33}$$

where coefficients $\boldsymbol{A}$, $\boldsymbol{B}$, $\boldsymbol{C}$, $\boldsymbol{D}$, $\boldsymbol{E}$ and $\boldsymbol{F}$ were calculated from curve fitting tools, as shown by Figure 3.12. These coefficients are to be evaluated for a beam pattern of a transducer of a given radius and carrier frequency. By symmetry, the final equations for the angle α as a function of β and δ_x and angle β as a function of α and δ_y are:

$$\alpha(\beta, \delta_x) = \left(\boldsymbol{A}\delta_x^5 + \boldsymbol{B}\delta_x^3 + \boldsymbol{C}\delta_x\right)\beta^4 + \left(\boldsymbol{D}\delta_x^3 + \boldsymbol{E}\delta_x\right)\beta^2 + \boldsymbol{F}\delta_x \tag{3.34}$$

$$\beta(\alpha, \delta_y) = \left(\boldsymbol{A}\delta_y^5 + \boldsymbol{B}\delta_y^3 + \boldsymbol{C}\delta_y\right)\beta^4 + \left(\boldsymbol{D}\delta_y^3 + \boldsymbol{E}\delta_y\right)\beta^2 + \boldsymbol{F}\delta_y \tag{3.35}$$

Because the two equations are functions of each other, an iterative method is needed to solve for α and β. For equations that cannot be solved with general analytical

method, the relaxation method requires the function $f(x)$ to be transformed into an iterative form such as $f(x_{n+1}) = f(x_n)$. By assuming an initial value x_0, a solution will be achieved from the iterative method when a fixed point $x_{n+1} = x_n$ is obtained. Because only one value of α and β can be obtained from a given δ_x and δ_y, the system can only converge to one solution for both angles. To speed up the process, the initial value α_0 and β_0 can be evaluated from the linear approximation (3.30) and (3.31), and the polynomial equation can be used starting with these values to add the non-linear correction induced by a quadrant shaped transducer.

3.3.5 Target strength estimation

With measurements of intensity, range and θ angle using the measure α and β in equation 1.3, the target strength (TS) can be estimated for every TOI in each ping. TS is given by the active sonar equation

$$\mathrm{TS} = \mathrm{RL} - \mathrm{DI} + 2\mathrm{TL} + 2\mathrm{AL} - \mathrm{SL} \tag{3.36}$$

where RL is the received level of the TOI given by the measured received intensity I and the sensitivity of the instrument, DI is the directional compensation given by the logarithm of equation (3.8)

$$\mathrm{DI} = 20\log_{10}\left(\frac{J_1(ka\sin\theta}{ka\sin\theta}\right), \tag{3.37}$$

TL is the transmission loss due to spreading measured with

$$\mathrm{TL} = 20\log_{10}\left(\frac{r}{r_0}\right) \tag{3.38}$$

where r_0 is the reference range defined by 1 m, AL is the absorption loss

$$\mathrm{AL} = \alpha_c r \tag{3.39}$$

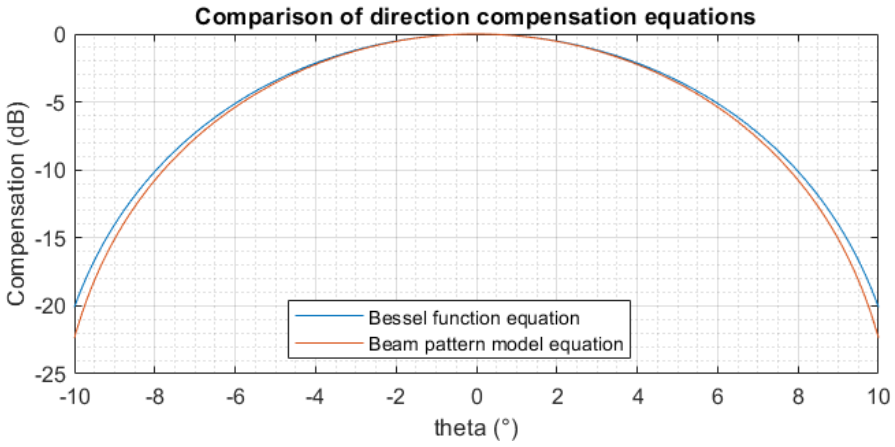

Figure 3.13: Comparison of the parameter DI using the Bessel function equation (3.37) and the beam pattern model equation (3.40).

where α_c is the absorption coefficient as described by equation 3.11, and SL is the source level on transmit. The value of SL is set to 216 dB to match the recorded transmit power of the AZFP-Split prototype.

An alternative method to measure the directional compensation is to use equation (3.13) with the array of subdivision of the full transducer. The equation for the parameter DI then becomes

$$\mathrm{DI} = 20\log_{10}\left(\sum_{n=1}^{N}\frac{g_n e^{ikr_{qi}}}{r_{qi}}\right) \tag{3.40}$$

where N is the number of subdivisions of the surface of the transducer. Figure 3.13 shows the difference between the two equations. A difference of ~ 2 dB at $\theta = 10^\circ$ is observed.

The target strength measurement for the individual channels has been considered. The measurement is achieved by using the measured echo intensity of each channel compensated with equation (3.40) by using the surface of the corresponding quadrant of the transducer. This procedure compensates the target strength measurement with

a quadrant-shaped transducer beam pattern, and the target strength of the TOI can be measured as the mean of the four channels. However, this idea was discarded, because it would require calibration over each quadrant beam pattern and matching the gain of the preamplifiers of the four receiver channels in practice.

Chapter 4

Model Simulations

The model is run using the signal theory described in section 3.2, and the simulated signals are processed using data processing algorithms described in section 3.3. With targets of interest (TOI) scattered in the three-dimensional domain to cover the beam pattern, simulations provide insight on the impact of the beam pattern effect. The goal was to measure the accuracy of the TOI position measurement, the consistency of the target strength measurement over the entire domain, and the impact of various parameters over the results.

4.1 Position measurement accuracy

In the model, an array was created from -6.5° to 6.5° in increments of 0.5° for both α and β, and at a constant z value of 25 metres, making an array of 729 possible positions for the TOI. The TOI was set to a relative backscatter amplitude to result in a target strength of -53 dB to match field trial data. The model was run 729 times, introducing a TOI at one position at a time, using $n_i = 1$ particles, $\tau = 500$ μs, $f_s = 280$ kHz,

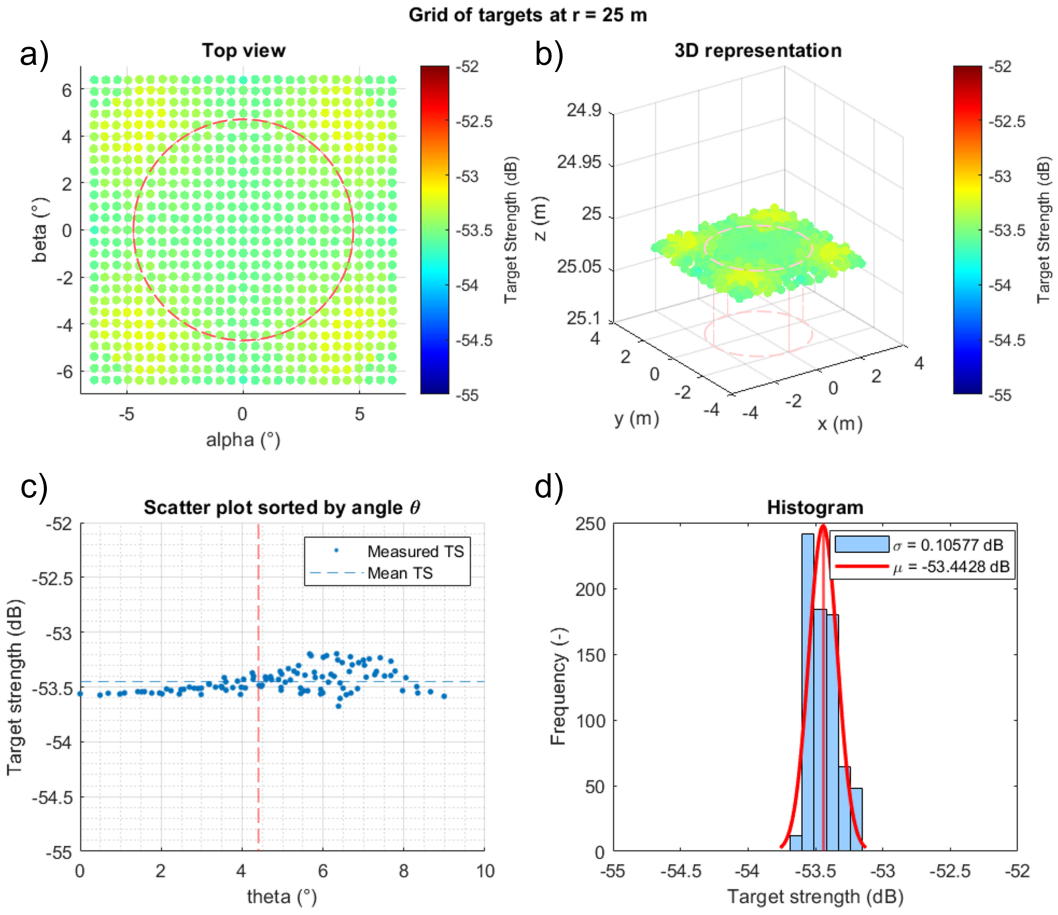

Figure 4.1: Modelled measured target strength of an array of 729 targets located at $r = 25$ m. The dashed red line represents the -3 dB beamwidth.

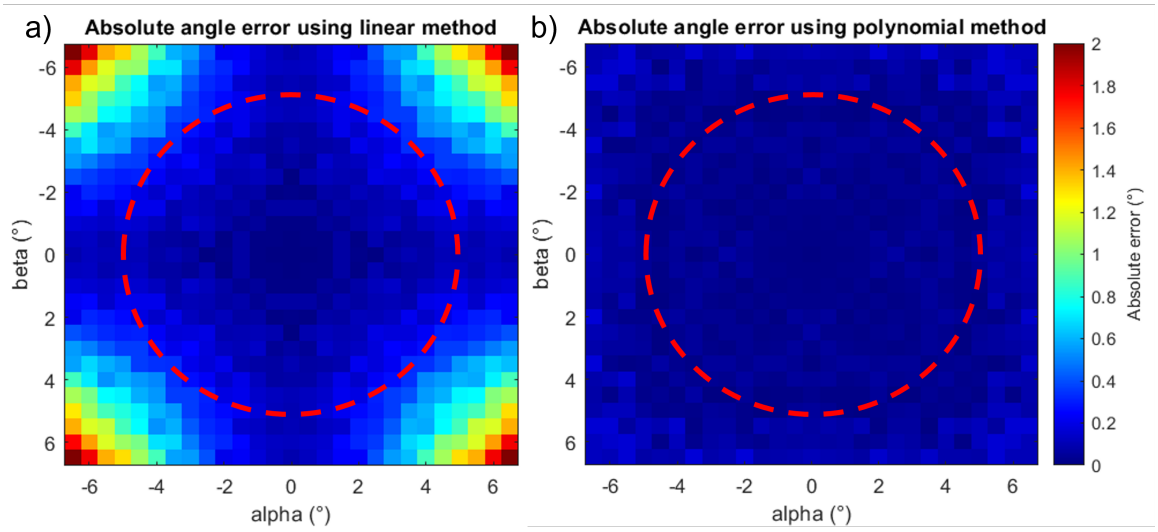

Figure 4.2: Absolute error of angle θ when using the linear equation (**a**)) and the polynomial equation (**b**)). The dashed red line represents the -3 dB beamwidth.

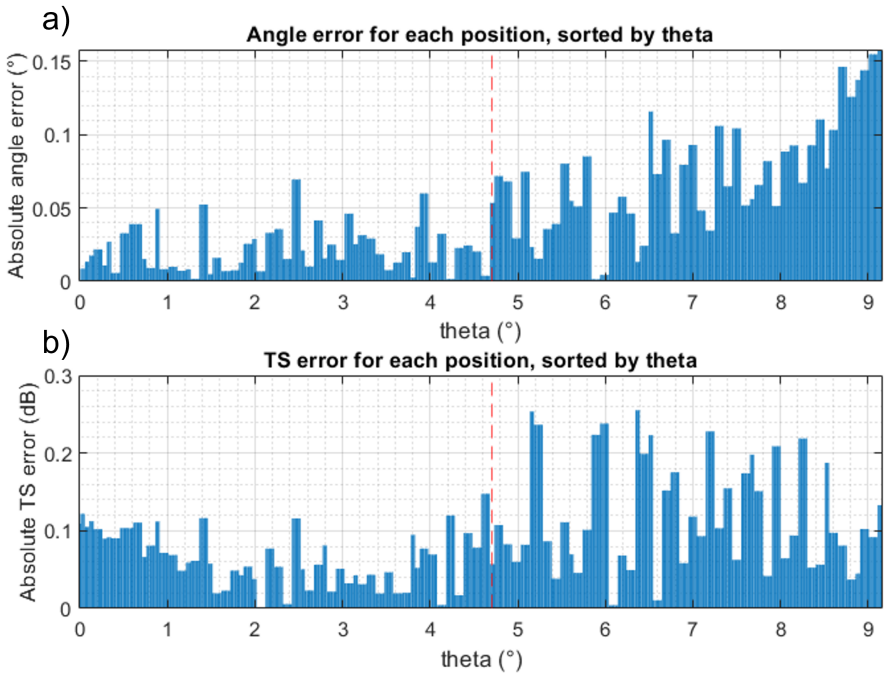

Figure 4.3: Absolute error bars of measured angle θ (**a**)) and target strength for each position of the TOI (**b**)), sorted by angle θ.

and $z_{\min}, z_{\max} = [23, 27]$ m. The position and target strength was evaluated for each TOI using the polynomial method for angular position measurement.

The results are presented by Figure 4.1. Figures 4.1 **a)** and **b)** show a dot for each identified TOI in every ping, located in the measured position in the three-dimensional space, and assigned a colour based on the measured target strength. The dashed red lines represent the -3 dB beamwidth, appearing as a circle in Figure 4.1 **a)**, the top view plotted with angle α against angle β, and as a cone in the three-dimensional representation in Cartesian coordinates in Figure 4.1 **b)**. Figure 4.1 **c)** shows a scatter plot of the measured target strength of each identified TOI against the angle θ, which is the measured angle of the TOI with the acoustic axis, showing the error due to directional compensation. Figure 4.1 **d)** is a histogram plot with the mean TS value and the standard deviation.

Figure 4.2 shows the absolute error of the measured angle θ when using the linear approximation describe by equations (3.30) and (3.31) and when using the polynomial equations described by (3.34) and (3.35). As expected from the results of Figure 3.6 **d)**, a large error would be expected when using the linear equations when both angle α and β are larger than the -3 dB beamwidth. Going from extreme values of -6.5° to 6.5°, the linear method yields an error up to 2.7°. The polynomial equation method keeps the error under 0.35°.

Figure 4.3 shows the absolute error of the measured angle θ and the measured target strength, sorted by angle θ. The mean absolute error (MAE) of the angle θ measured is 0.046°. Both error bar graphs show an increase in the absolute error with increase of angle θ. Within the -3 dB beamwidth, the maximum absolute error is 0.074° and 0.12 dB, and a mean error of 0.020° and 0.06 dB. At larger angles than

the -3 dB beamwidth, the maximum absolute error is 0.164° and 0.26 dB, and the mean error of 0.062° and 0.10 dB.

4.2 Target strength measurement consistency

Similarly to the method used in section 4.1, the model was run placing a TOI at an array of positions. Four arrays were created from -6.5° to 6.5° in increments of 0.5° for both α and β at ranges $r = 25$, 50, 75, and 100 metres. The domain was increased to $x_{\min}, x_{\max} = [-12, 12]$ m, $y_{\min}, y_{\max} = [-12, 12]$ m, and $z_{\min}, z_{\max} = [20, 105]$ m. Other parameters were unchanged from the previous section. This simulation extends the results from section 4.1 to three additional layers at various depths.

Figure 4.4 show the summary of the target strength measurement results. Every layer showed virtually identical results, indicating the symmetry of the system in the farfield. This also confirms the proper compensation of the target strength signal in range with the transmission and absorption loss calculations. The measured TS over the entire domain was within the range of -53.76 dB and -53.12 dB, with a mean value of -53.42 dB, meaning a maximum absolute error of 0.34 dB.

4.3 Impact of parameters

In order to explore the sensitivity of the model to various input parameters, a series of model trials were executed. The number of particles in the domain was explored to see the impact of signal-to-noise ratio (SNR) on the target strength measurement. Pulse length was also explored to see how it affects the precision of the instrument,

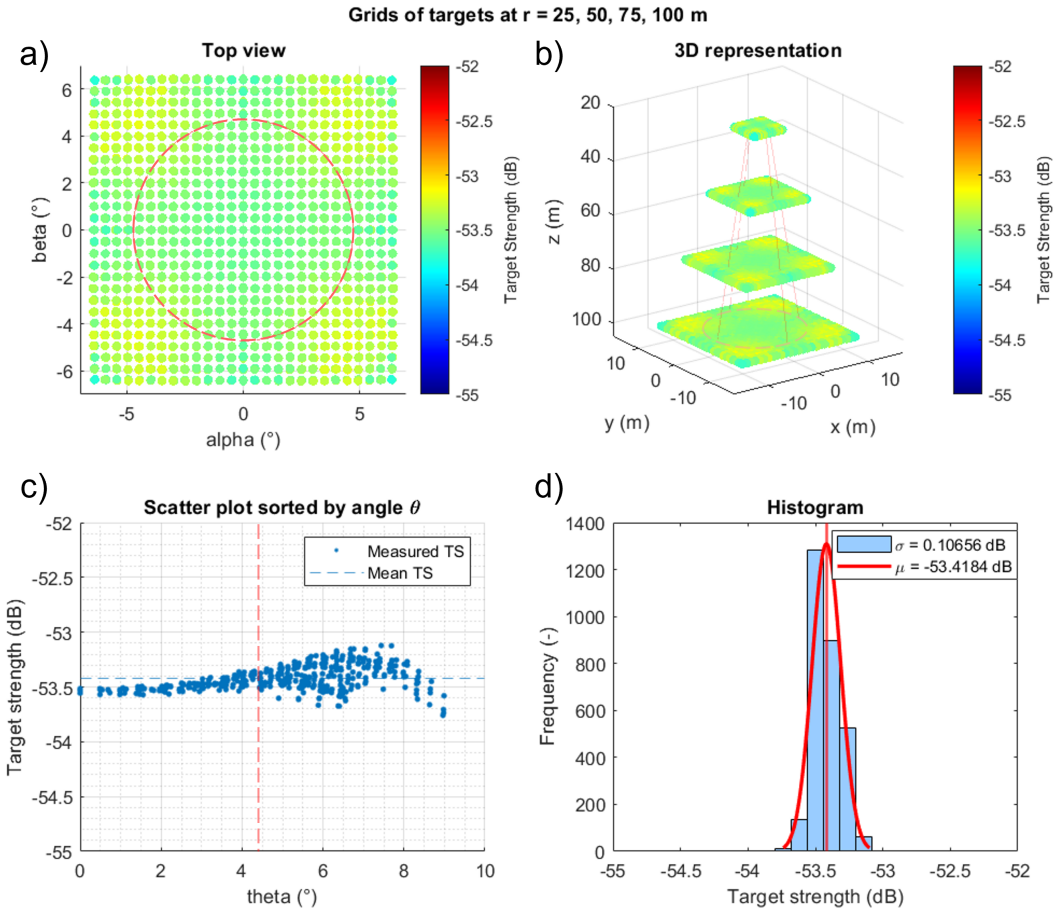

Figure 4.4: Modelled measured target strength of four arrays of 729 targets located at $r = 25$, 50, 75, and 100 m. The dashed red line represents the -3 dB beamwidth.

and how small the pulse can be while still being able to resolve the phase information. The sampling frequency was also explored by increasing the parameter κ in the digital demodulation of the signal, allowing sampling at frequencies less than the carrier.

4.3.1 Number of particles

Results from section 4.1 were recreated using $n_i = 300$ particles in the domain. The TOI is set to contribute an amplitude 160 times greater than that of the background particles. This approach adds a noise floor and allows a simulation of the system in the presence of noise or target clutter.

Figures 4.5 and 4.6 show a clear increase in position and TS error with increase of angle θ. Most positions measured within the -3 dB beamwidth, and therefore the mean TS, remain virtually identical. While the MAE of the measured angle is 0.06° and 0.21 dB for the TS, the maximum absolute error is 0.14° and 0.50 dB within the -3 dB beamwidth, and a mean error of 0.03° and 0.08 dB. At larger angles than the -3 dB beamwidth, the maximum absolute error is 0.36° and 1.6 dB, and the mean error of 0.08° and 0.35 dB.

Figure 4.7 shows the same error values compared to the signal-to-noise ratio (SNR). The noise level is the root mean square (RMS) of the signal before and after the position of the TOI in the signal, corresponding to the noise generated by the particles. Because data recorded at large angle θ corresponds to lower SNR, the graphs show a way to quantify the performance of the system. As expected, the error increases with decreasing SNR, but maintains an error below 0.36° in angle measurement and 1.6 dB in TS measurement for a SNR of 13.7 dB.

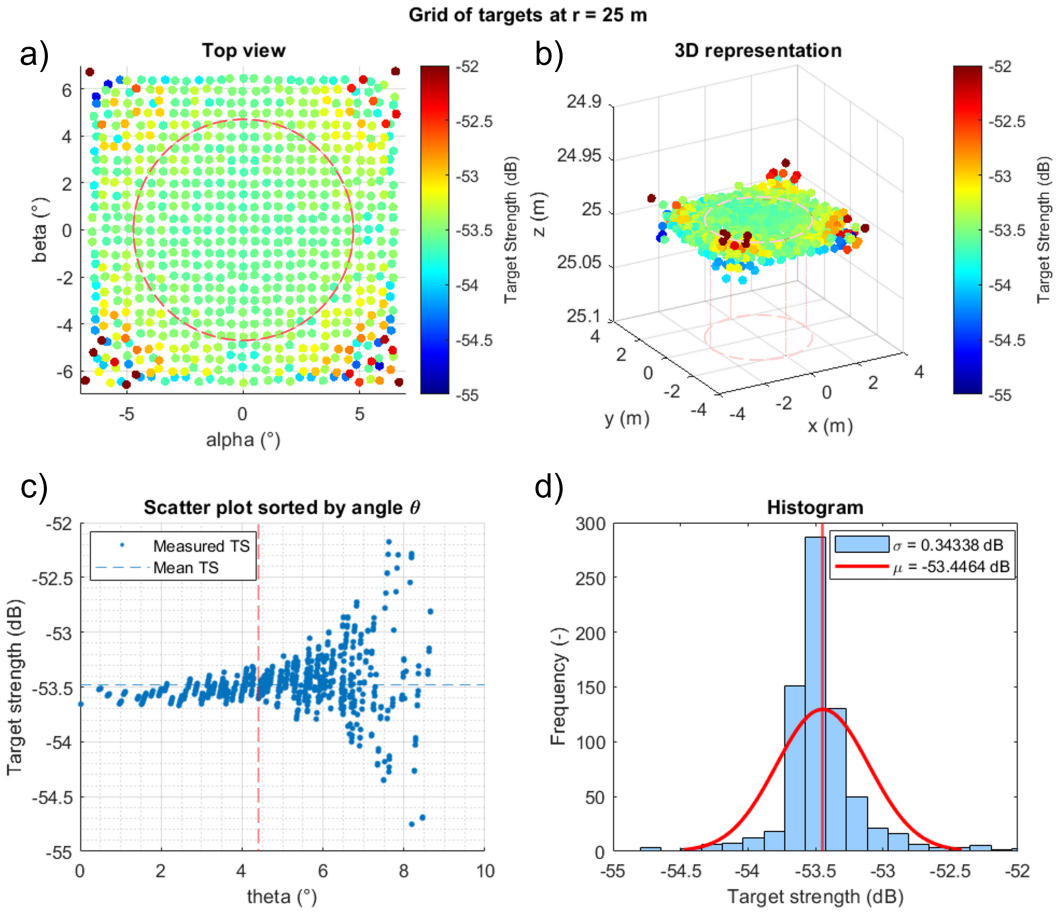

Figure 4.5: Modelled measured target strength of a grid of 729 targets with $n_i = 300$ particles. The dashed red line represents the -3 dB beamwidth.

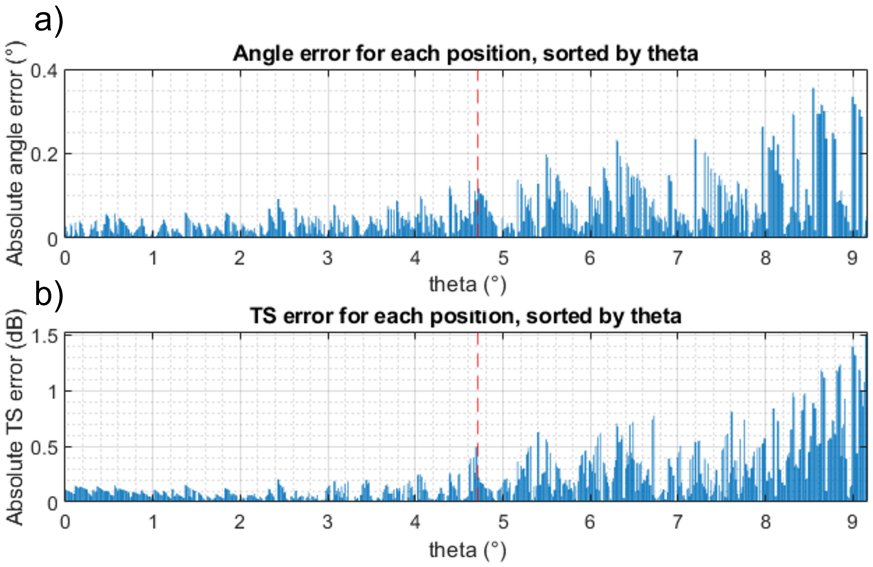

Figure 4.6: Absolute error bars of measured angle θ (**a**)) and target strength for each position of the TOI (**b**)) with $n_i = 300$ particles, sorted by angle θ.

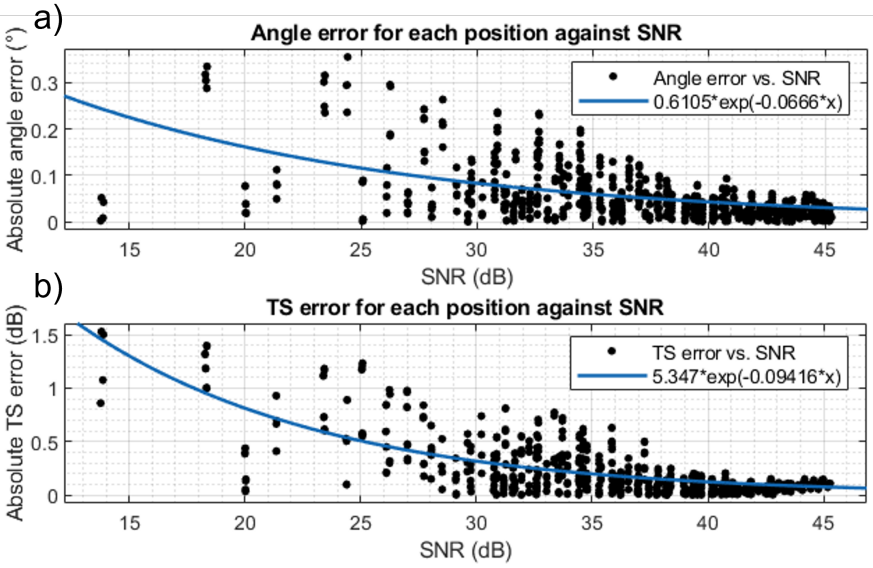

Figure 4.7: Comparison of the absolute error of measured angle θ (**a**)) and target strength (**b**)) for each position of the TOI with $n_i = 300$ particles with the signal-to-noise ratio.

τ (μs)	$\overline{\text{TS}}$ (dB)	σ (dB)	MAE_θ (°)
1000	-53.40	0.10	0.040
500	-53.41	0.08	0.036
300	-53.42	0.08	0.034
200	-53.49	0.08	0.029
100	-56.30	0.10	0.031

Table 4.1: Comparison of the target strength and angle measurement for various pulse lengths.

4.3.2 Pulse length

To simulate the field trials with the AZFP-Split prototype, the model was run over $n_p = 24$ pings with a target moving across the beam, with a negative velocity in x and y, and a range increasing from 25 to 100 metres. $n_i = 2000$ particles were generated to introduce noise in the signal, and the domain was generated with $x_{\min}, x_{\max} = [-8, 8]$ m, $y_{\min}, y_{\max} = [-8, 8]$ m, and $z_{\min}, z_{\max} = [20, 105]$ m. Figure 4.8 shows the results from the model using $\tau = 500$ μs.

Values of mean target strength $\overline{\text{TS}}$, standard deviation σ, and the mean error of the measured angle θ over the 24 pings were computed for pulse length values of 1000, 500, 300, 200, and 100 μs. The results are shown on Table 4.1. The mean TS show close to no difference with pulse length, except for $\tau = 100$ μs. This is expected because the pulse generated by the model does not reach full amplitude at $\tau = 100$ μs with a pulse filtered with a bandwidth of $B = 7$ kHz, thus inducing smaller intensity to the backscattered echo. This would not necessarily be observed with every sonar,

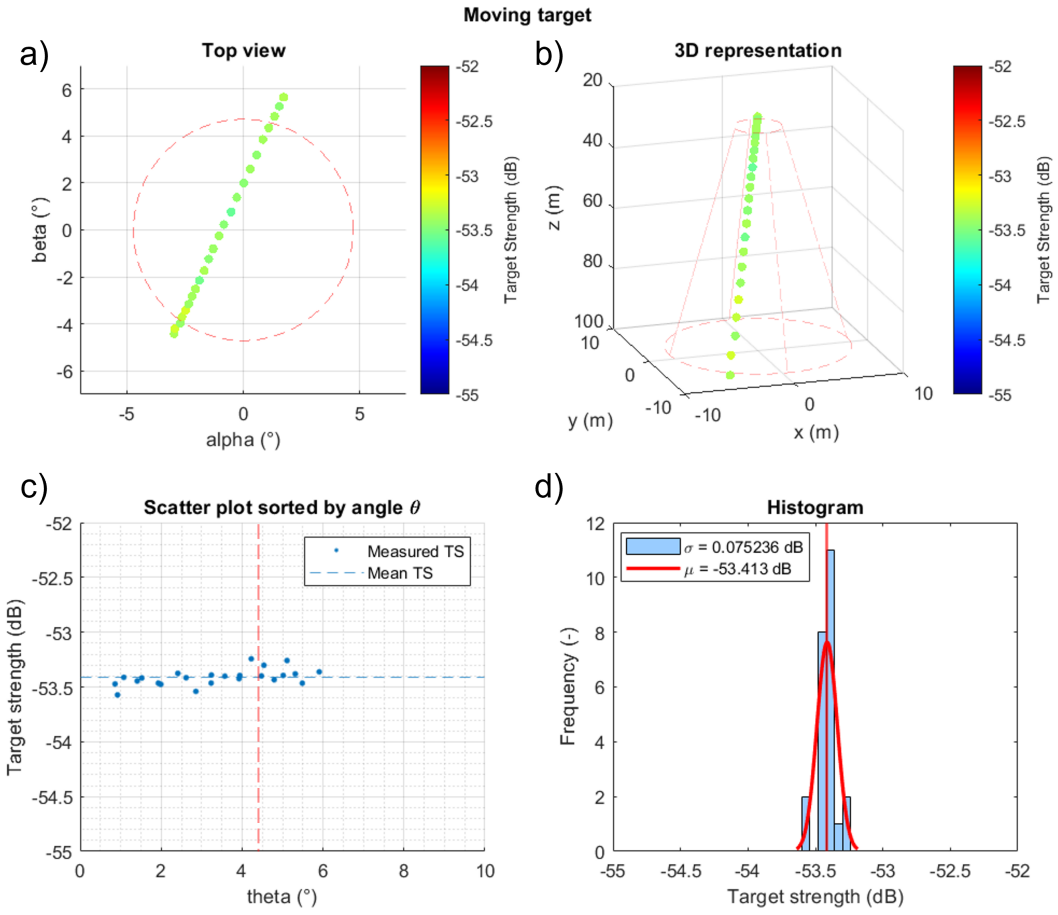

Figure 4.8: Modelled measured target strength of $n_p = 24$ pings for a moving target with $\tau = 500$ μs. The dashed red line represents the -3 dB beamwidth.

κ	f_s (kHz)	$\overline{\text{TS}}$ (dB)	σ (dB)	MAE_θ (°)
1	280	-53.41	0.08	0.032
2	93.33	-53.41	0.12	0.045
3	56	-53.40	0.16	0.042
4	40	-53.43	0.18	0.040
5	31.11	-53.49	0.26	0.055
6	25.45	-53.52	0.29	0.061

Table 4.2: Comparison of the target strength and angle measurement for various sampling frequencies.

because the resonance depends on the characteristics of the transducer. The smallest pulse length does not affect the precision or the phase measurement, because the standard deviation and the mean angular error θ remain almost unchanged with the value of the pulse length. In principle, this offset could be corrected with calibration.

4.3.3 Sampling frequency

Using the same simulations and parameters as used in section 4.3.2, but with a pulse length of $\tau = 500$ μs, various sampling frequencies were studied. By increasing the value of the integer κ in the digital demodulation equation (3.15), values of sampling frequencies can be obtained in a way that preserves the information of intensity and phase of the original signal. This allows the echo to be recorded at a frequency lower than the carrier frequency f_c while preserving the signal information. Values of κ from 1 to 6, resulting in sampling frequencies of 280, 93.33, 56, 40, 31.11, and 25.45 kHz are modelled, and the resulting $\overline{\text{TS}}$, σ and mean angular error are given by Table

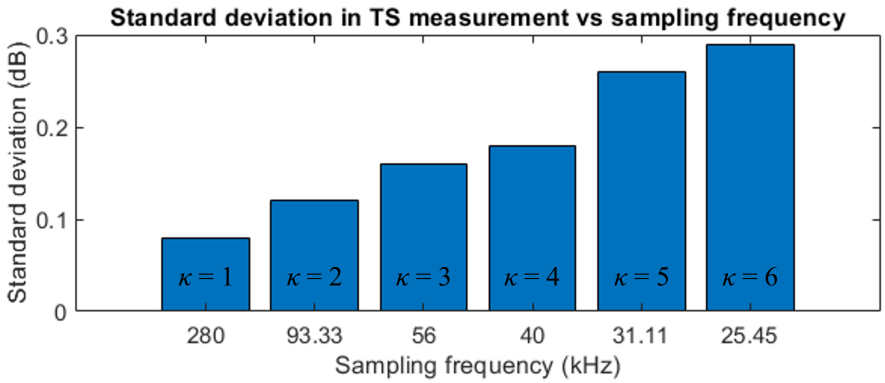

Figure 4.9: Comparison of the standard deviation over the target strength measurement with the sampling frequency given by the digital demodulation coefficient κ.

4.2.

Figure 4.9 shows the increase in the standard deviation with the digital demodulation coefficient κ. Despite having similar mean measured target strength, the precision of the measurements decrease slightly with subsampling, but yields accurate results nonetheless. The uncertainty in the angle measurement also increases by 0.03° between $\kappa = 1$ and $\kappa = 6$.

4.4 Summary of results

The simulation of a backscattered signal using a split-beam transducer was used to explore accuracy sensitivities in a split-beam sonar. The efficiency of the data processing algorithm was demonstrated in a noise-free simulation with a singular particle, showing a low standard deviation in target strength of $\sigma = 0.11$ dB and a maximum absolute error of 0.34 dB. With the introduction of noise down to an SNR of 13.7 dB, the absolute error in TS measurement increases up to 1.6 dB.

Changes in pulse length from 100 to 1000 μs had minimal impact on results, changing the mean measure TS by 0.09 dB and the standard deviation by 0.02 dB. The only exception was the pulse length of $\tau = 100$ μs, where reduced response was attributed to the bandwidth filter of the pulse template limiting pulse amplitude.

Adjusting the sampling frequency using digital demodulation indicated consistent average TS values. An increase of 0.21 dB in standard deviation between sample rates of 280 to 31.11 kHz was observed, as the digital demodulation method is known to introduce noise through aliasing out-of-band signals.

Chapter 5

Prototype Instrument

The split-beam sonar model project was part of a collaboration with ASL Environmental Sciences. The work on the model was done in parallel with the development of a split-beam sonar prototype. The model was used to guide the company with the choice of transducer geometry, predict the sonar performance for given variables, help with the calibration process of the prototype system and analyze the data from field trials.

5.1 AZFP-Split prototype

The first attempt of a split-beam prototype by ASL Environmental Sciences was made of an array of four cylindrical transducers operated at $f_c = 308$ kHz, as shown by Figure 5.1. Despite this configuration being more of a proof of concept than a potential array candidate, this configuration was quickly discarded by the model. The modelled beam patterns show the distance between the elements needs to be in the order of the acoustic wavelength to have a beamwidth large enough to be

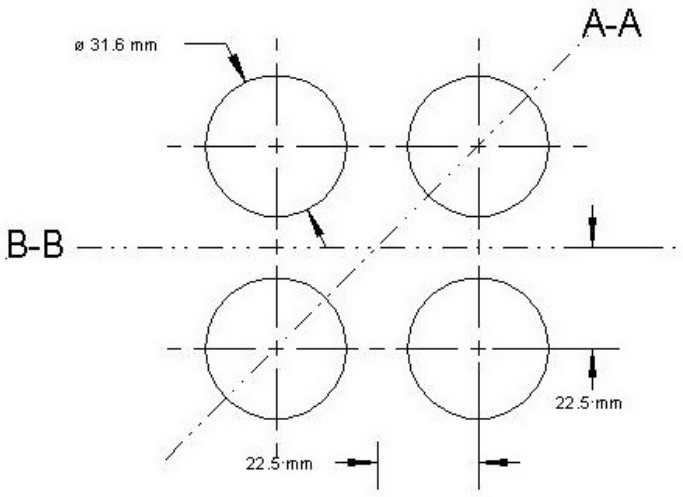

Figure 5.1: Schematic of the $f_c = 308$ kHz prototype split-beam array.

usable with no phase ambiguity. With a separation of 45 mm between the centre of the elements, the 308 kHz array showed a -3 dB beamwidth of 1.9° with the beam pattern model.

After the 308 kHz array was discarded, the following prototype was based on an Airmar M475 split-beam transducer operated at $f_c = 70$ kHz. As represented by Figure 3.2, the array is formed of four quadrant-shaped transducers made of a total of 376 elements.

The transmit circuit consists of a pulse generator that is fed into a power amplifier. The pulse is sent to the transducer where it is converted into acoustic energy. The receiver circuit then starts recording the signal by the four quadrants of the transducer; each channel is fed through preamplifiers, and then through an analog-to-digital converter (ADC) and field-programmable gate array (FPGA). It was set to digitally convert the signal to 18-bit signed integers. For the field trials, the board and the battery was put in a waterproof metal box, as shown by Figure 5.2. The ultimate

Figure 5.2: AZFP-Split prototype circuit board during the field trials. The battery is under the board.

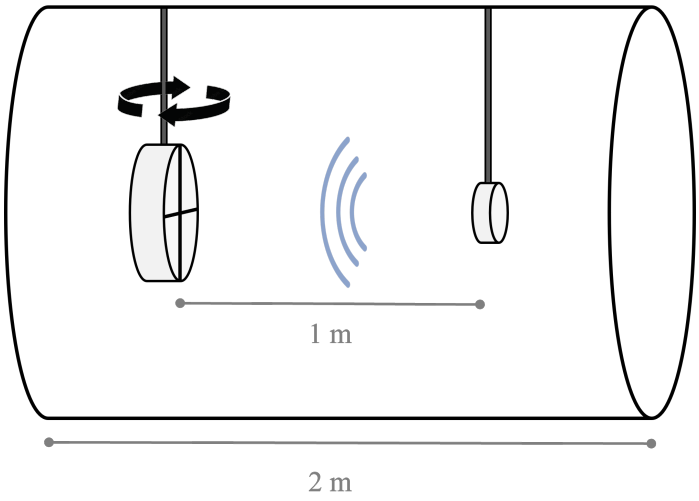

Figure 5.3: Schematic of the receiver calibration setup with the 2 metre tank.

goal is to have a system in a pressure-proof enclosure for long period deployment.

5.2 Calibration

Transducer source level and sensitivity were established through lab calibration in the weeks preceding the field trials. These calibrations were made in ASL Environmental Sciences facilities in Saanichton in January 2023.

On January 12, 2023, the sensitivity of the sonar system was evaluated. As shown by Figure 5.3, the split-beam transducer, wired as a receiver, was placed in the farfield at 1 metre away from a calibration projector. The distance of the theoretical farfield R_0 is defined by

$$R_0 > \frac{\pi a^2}{\lambda} \tag{5.1}$$

where a is the transducer radius, and λ is the wavelength. The fraction on the right side of the equation, using the parameters from the split-beam prototype, yields 0.65

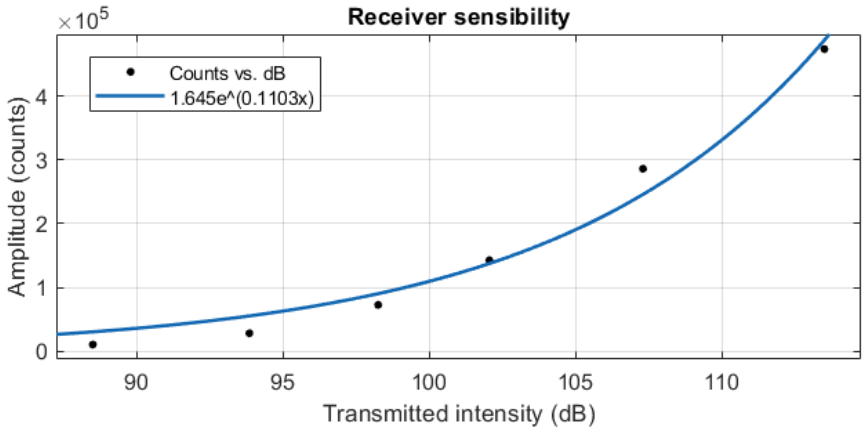

Figure 5.4: Measured receiver sensitivity using the sum of all four receivers and the exponential function fit.

meters. Thus, the distance of 1 meter respects equation (5.1) and was judged to be sufficiently in the farfield to conduct calibration steps. The split-beam transducer was aligned on the projector axis so that the phase difference between the channels would be close to 0. The projector was set to emit a 100 μs pulse at six different intensity values. Figure 5.4 shows the relationship between the transmitted intensity of the projector and the amplitude of the sum of the four receivers in counts, as recorded by the A/D on the circuit board. An exponential function fit was made from the data to provide an equation to convert the recorded amplitude in counts to decibels. The equation to convert counts units to received level RL in decibels is given by

$$\mathrm{RL} = \frac{\ln(|\sum I| / 1.645)}{0.1103} \tag{5.2}$$

where I is the received signal amplitude in counts.

Receiver calibration tests were performed in a 2-metre-long plastic tank on January 13 and 16, 2023. Using the same setup as described by Figure 5.3, the two-metre tank was used to measure the receiver beam pattern and phase response. The split-

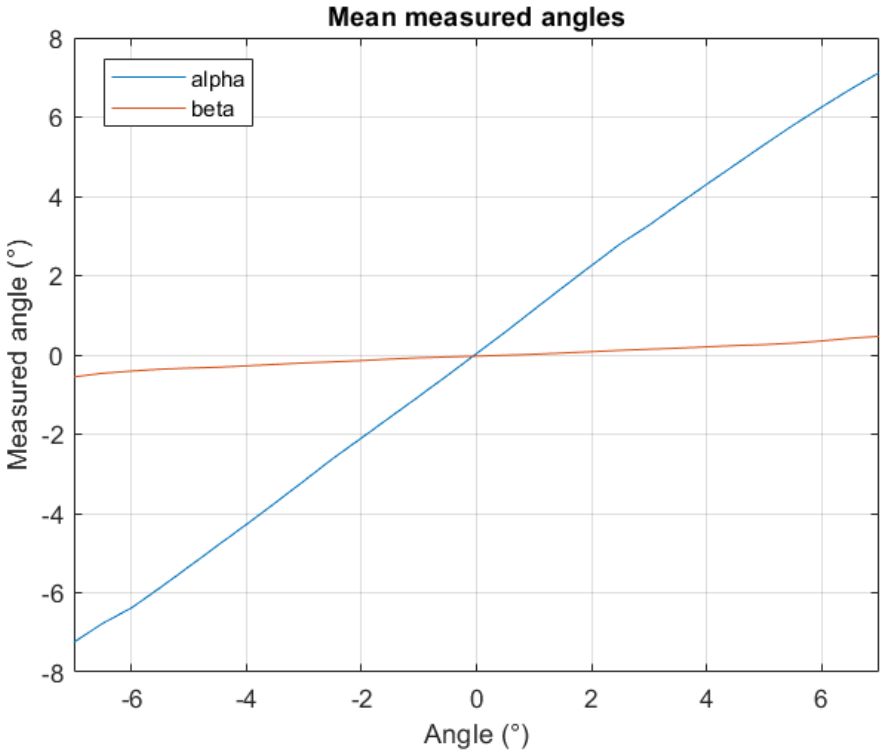

Figure 5.5: Mean value of the measured angles α and β over 5 pings by rotating the transducer from $-7°$ to $7°$ in increments of $0.5°$ in the 2-metre tank.

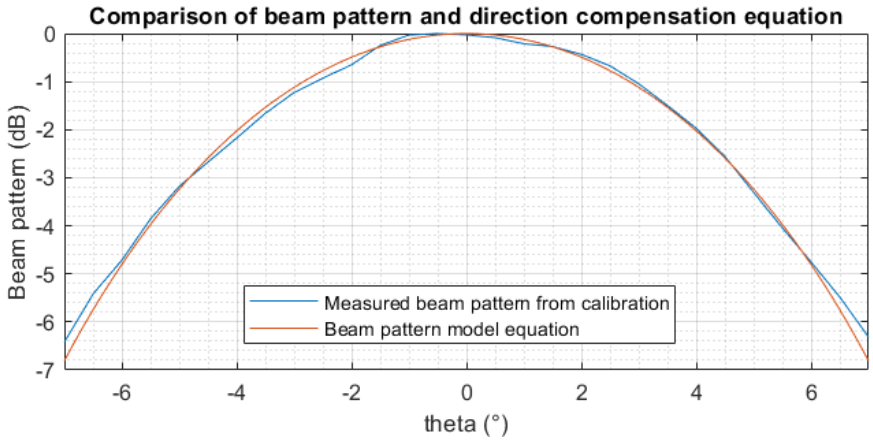

Figure 5.6: Comparison of the measured beam pattern of the transducer and the parameter DI using the beam pattern model equation (3.40).

beam transducer was rotated around the y axis from -7° to 7° in increments of 0.5°. Data was recorded with the projector transmitting 5 pings at a carrier frequency of 70 kHz and a pulse length of 10 μs for each angle increment. Values of α and β were measured, and the coefficients of equations (3.34) and (3.35) were adjusted so that the measured angle matched the rotation angle. Figure 5.5 show the mean measured angles over the 5 pings for each rotation angle for both α and β. The linear dependence of β on α suggests the split-beam transducer was slightly rotated around the acoustic axis, but calibration of the coefficients could still be made by using the combined angle θ. The orange curve of Figure 5.6 shows that simulation done by the model of the rotation of a transducer around the y axis with a projector at 1 metre away provided a matching curve when the transducer rotated around the z axis by $\sim 0.2^\circ$.

The directional compensation DI was also verified to match the equation (3.40). Figure 5.6 shows the comparison with the measured relative amplitude of the sum of the four channels and the equation of the model beam pattern. The theoretical beam pattern matches the observed beam pattern with an error of less than 0.16 dB between -6° and 6°, and increases to 0.39 dB at -7° and 7°.

On January 30, 2023, backscatter trials were done in a larger metal tank. With a length of 5 metres and a radius of 2.5 metres, the tank provided an underwater environment to have backscatter trials with a calibration sphere 4.4 metres away from the transducer. An example of the received signal is shown by Figure 5.7. For this trial, the sonar was not programmed to lower the transmit power. As a result, the signal from the calibration sphere, located at 4.4 metres, was fully saturated and the phase information could not be retrieved. However, it was possible to retrieve the

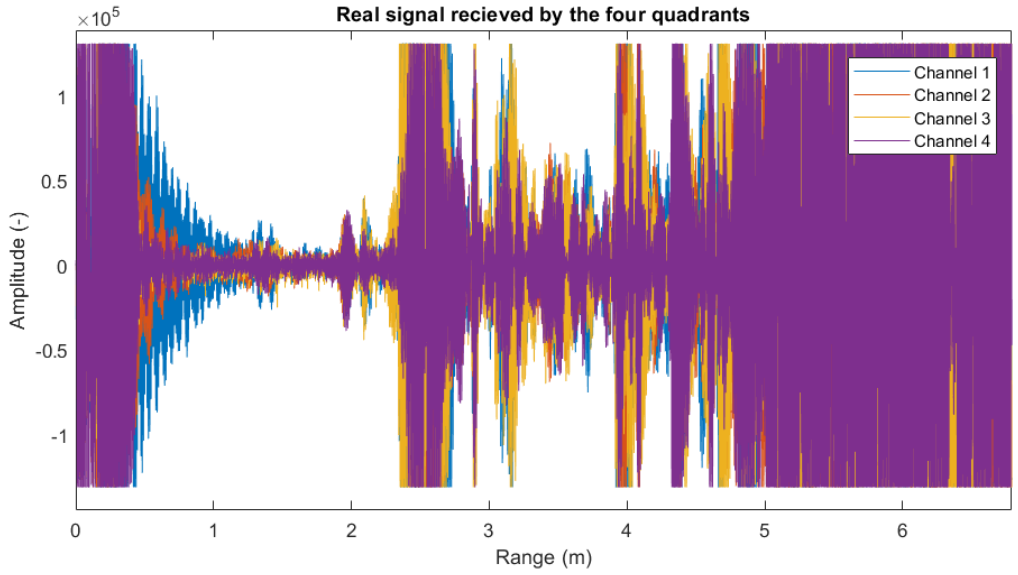

Figure 5.7: Signal received by the four channels with a calibration sphere at 4.4 metres from the transducer in the 5 metre tank.

range of the target, as well as measuring the range of the backscattered echo from the sidelobes at 2.5 metres, and the back of the tank at 5 metres. This test confirmed the correct functioning of the sonar prior to the field trials, with both the transmit and receiving functions operating properly, and the data was read and displayed correctly by the data processing algorithm.

5.3 Field trials

On February 1, 2023, field trials for the AZFP-Split were conducted in Saanich Inlet, near Victoria, British Columbia. The location was chosen for its proximity to the ASL Environmental Sciences office in Saanichton, and for DFO's Institute of Ocean Sciences on Patricia Bay, from where the research vessel was launched, and for the

Figure 5.8: Airmar M475 transducer hanging on the side of the vessel, photo from the February 1, 2023, field trip.

availability of the deep water in a relatively protected coastal area. The experiment was made possible by Stéphane Gauthier, research scientist with DFO, who was the skipper for the trials. The crew consisted of Steve Pierce and Graeme Thompson from ASL Environmental Sciences, Dr. Len Zedel and Axel Belgarde from Memorial University of Newfoundland. The research vessel provided by DFO for the trials was the R/V Doug Anderson. Figure 5.8 shows the transducer setup on the vessel.

A list of goals was set for the field trials. These goals included:

1. Measure the noise recorded by the instrument in a minimal noise environment,
2. Transmit and receive a sound pulse with the prototype sonar system,
3. Measure the maximum operating range of the instrument at full power,
4. Measure the target strength of a calibration sphere at different positions in the beam,
5. Evaluate the impact of sampling frequency and pulse length on the results.

The calibration sphere as well as the ballast weight and attachment hardware were attached at the end of a fishing line shown by Figure 5.9. Figure 5.10 shows the configuration, with each target around one metre apart. A piece of electrical tape was added to help identify the location of the targets when reeling in the line. Using NOAA's Standard Sphere Target Strength Calculator from Fisheries Resources Division, Southwest Fisheries Science Centre, the TS of the 0.5" calibration tungsten sphere at a carrier frequency of 70 kHz was estimated at -53 dB under the approximated field trials condition of water temperature of 8°C and conductivity of 3 S/m.

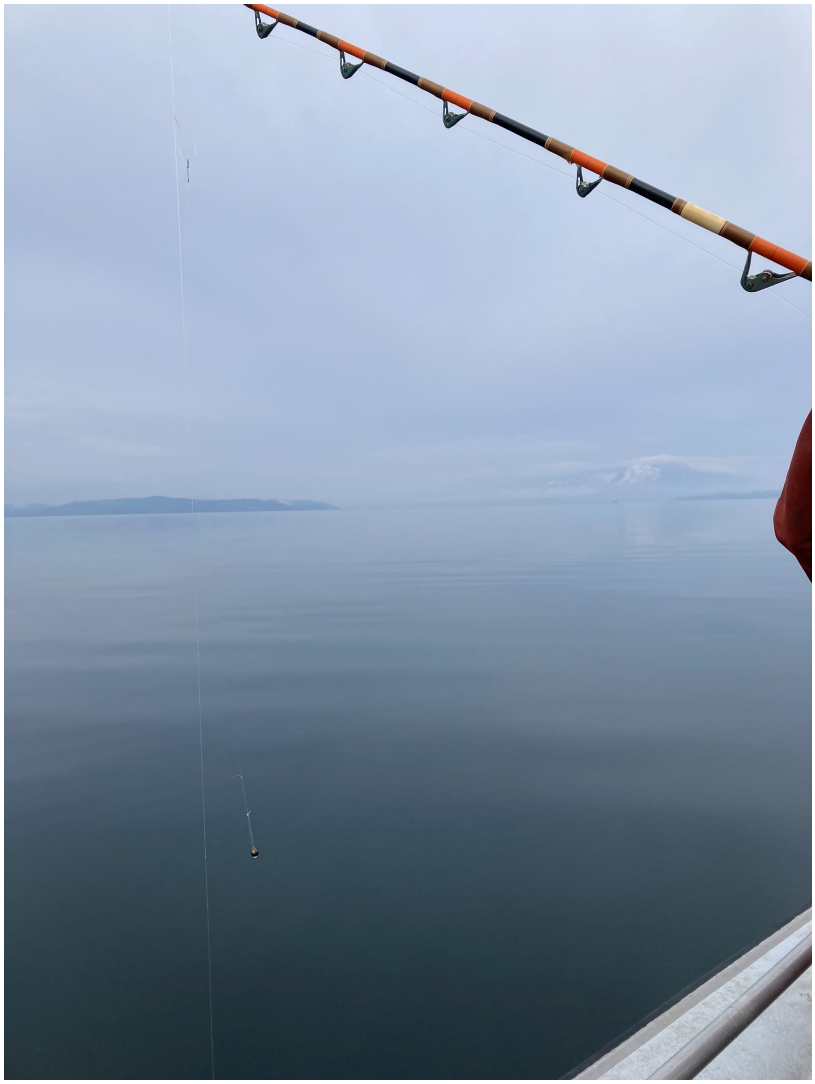

Figure 5.9: Tungsten calibration sphere attached to the fishing line, photo from the February 1, 2023, field trip.

File name	f_s (kHz)	τ (μs)	n_p (pings)	Time (hh:mm)	Comment
`00010100_01C.ASLSplit`	280	0	77	10:12	Noise measurement, no transmission
`00010100_01D.ASLSplit`	280	1000	85	10:18	Target dropping on starboard side
`00010100_01E.ASLSplit`	280	1000	81	10:25	Target lifting on starboard side
`00010100_01F.ASLSplit`	280	500	121	10:47	Target drop + lift on starboard side
`00010100_01G.ASLSplit`	280	300	151	10:57	Target drop + lift on starboard side
`00010100_01H.ASLSplit`	280	100	135	11:10	Target drop + lift on port side
`00010100_01I.ASLSplit`	560	500	165	11:20	Target drop + lift on port side
`00010100_01J.ASLSplit`	560	0	164	11:33	Noise measurement, no transmission
`00010100_01K.ASLSplit`	-	-	64	11:38	(Part 1 of 00010101_01A.ASLSplit)
`00010101_01A.ASLSplit`	280	0	13	11:38	Noise measurement, no transmission
`00010101_01B.ASLSplit`	280	300	127	11:47	Dropping copper spheres and steel spheres
`00010100_01L.ASLSplit`	56	0	-	12:04	Noise measurement / Experimental settings
`00010100_01M.ASLSplit`	280	300	218	12:15	Walking around with a target down at $\sim$25 m

Table 5.1: List of data files captured during the February 1, 2023, field trials.

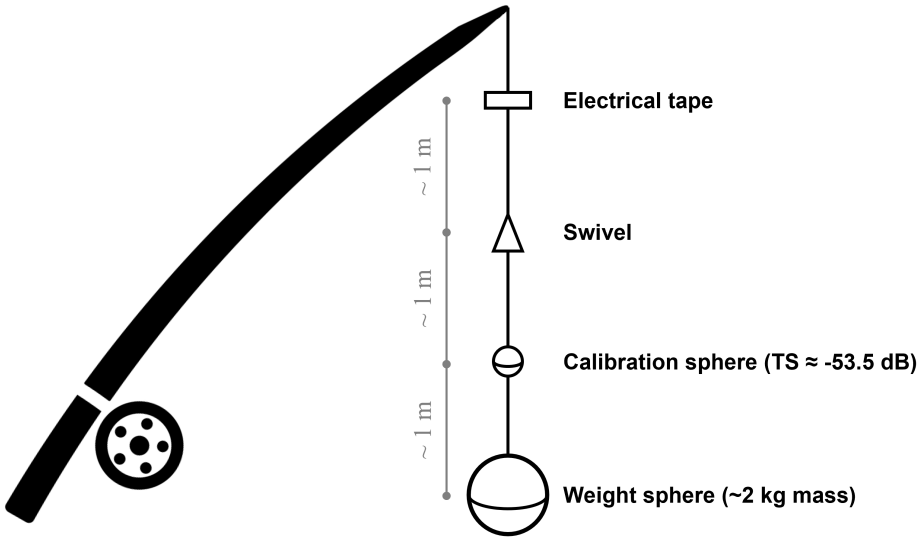

Figure 5.10: Diagram of the different elements on the fishing line during the field trials.

Thirteen data files were recorded over a period of just over two hours. As listed in Table 5.1, data were collected at sampling frequencies of f_s = 56, 280 and 560 kHz, which correspond to 0.8, 4 and 8 times the carrier frequency respectively. Different pulse lengths were also explored, including τ = 100, 300, 500 and 1000 μs. All datasets were recorded to a range of 250 metres. In total, 4 noise measurements, 6 recordings with the calibration sphere going from the surface to 220 metres depth, 1 recording with copper and steel spheres, and 1 recording with the calibration sphere at a constant ∼25 m were conducted. Recordings `00010101_01B.ASLSplit` and `00010100_01L.ASLSplit`, corresponding to the copper and steel spheres and the f_s = 56 kHz respectively as described by table 5.1, ended up being unsuccessful because the on-board settings ended up failing the experiment. Recordings `00010100_01K.ASLSplit` and `00010101_01A.ASLSplit` were from the same dataset, but split in two files for unknown reasons.

#	Time (hh:mm)	GPS coordinates (°,°)
1	10:12	48.607497, -123.499845
2	10:47	48.606728, -123.501321
3	11:10	48.606241, -123.502697
4	11:33	48.605756, -123.502461
5	12:04	48.604570, -123.504097
6	12:15	48.605134, -123.504837

Table 5.2: GPS coordinates recorded on the February 1, 2023, field trials.

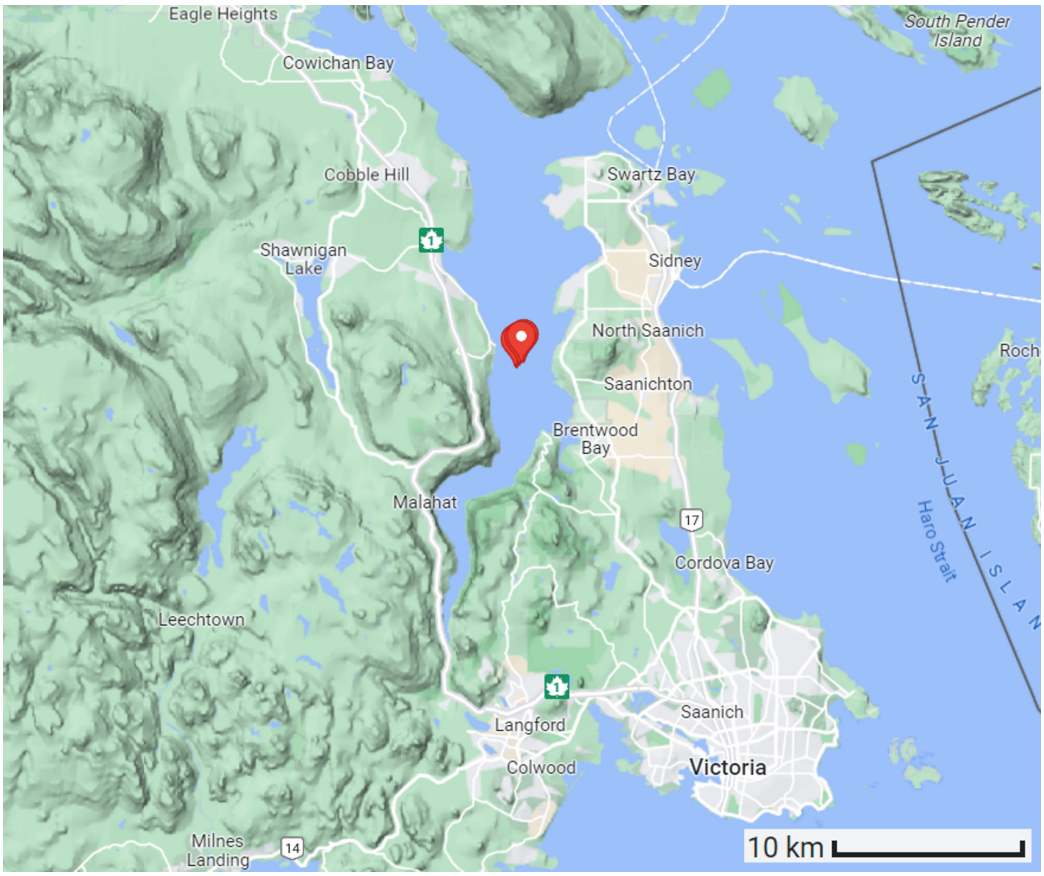

Figure 5.11: Location of the February 1st field trials in Saanich Inlet.

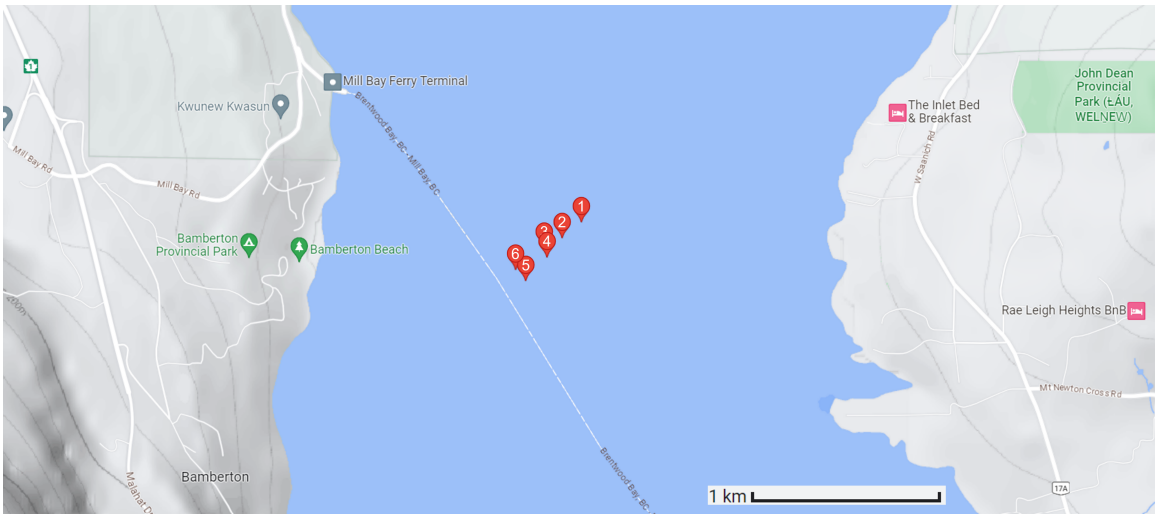

Figure 5.12: Location of the six recorded GPS coordinates, numbered chronologically.

As shown by Table 5.2, the GPS location at the start of the data acquisition was (48.607497°, -123.499845°), and ended up at (48.605134°, -123.504837°). As illustrated in Figure 5.12, the boat drifted a distance of ∼500 m over the two hours of data acquisition.

A CTD profiler was cast at the end of the data acquisition. It was lowered to a depth of ∼50 m to measure the temperature and conductivity of the water to estimate the sound speed in the water column. The recorded temperature and salinity are shown by Figure 5.13. Using equation (1.1), the approximated sound speed used in data processing is 1443 m/s.

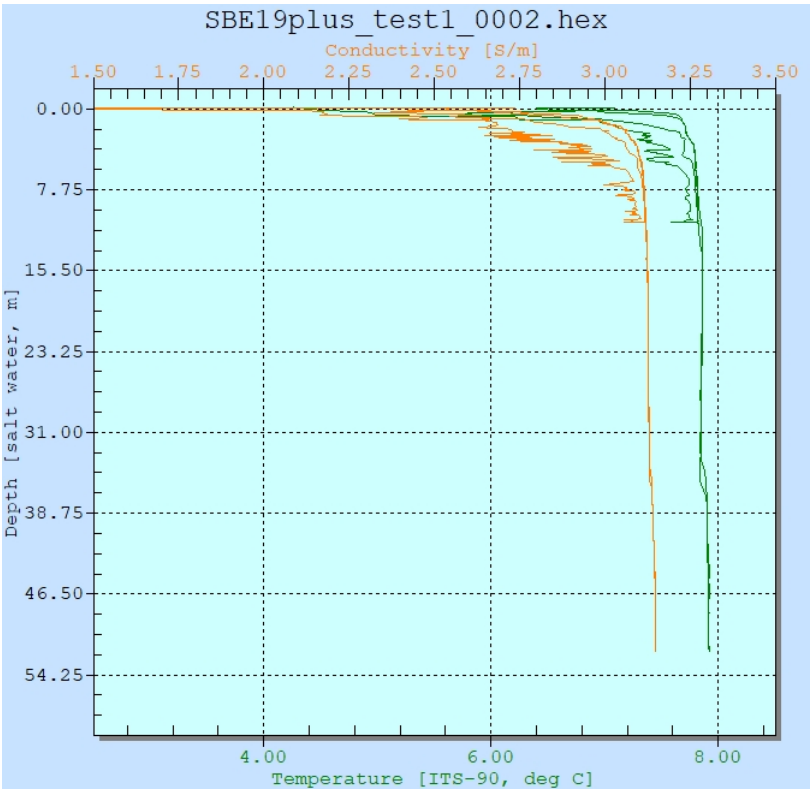

Figure 5.13: Temperature and conductivity profiles recorded by the CTD profiler on February 1st.

Chapter 6

Field Trials Results

6.1 Data analysis

The data analysis tools developed for reviewing the sonar model presented in section 3.3 were suitable for measuring the intensity, range, position and target strength of the calibration sphere in the field trials. An extra algorithm routine for target detection was developed for the field trials data. An algorithm was also written to split the raw signal by pings, and plot each ping against the measured depth, thus creating echogram figures.

6.1.1 Noise measurement

Four datasets of noise measurement were made during the field trials. Two were made at $f_s = 280$ kHz at an hour apart, one was made at $f_s = 560$ kHz, and one was made with experimental settings at $f_s = 56$ kHz. The latter was not analyzed, because the FPGA coding was incompatible with the experimental sampling rate.

File name	f_s (kHz)	Time (hh:mm)	n_p (pings)	Mean noise (dB)
00010100_01C.ASLSplit	280	10:12	77	49.0
00010100_01J.ASLSplit	560	11:33	164	46.1
00010100_01K.ASLSplit + 00010101_01A.ASLSplit	280	11:38	77	46.6

Table 6.1: Mean noise value measured for the three noise measurement datasets.

Table 6.1 shows the mean received level values recorded with no transmission in the water for the three noise measurement datasets. The results show a decrease of 3 dB between the earlier and later datasets. No significant difference is observed between the two sampling frequencies.

6.1.2 Echogram figures

An overview of the field trial data is best achieved by looking at the echograms from the received data. An echograms is a representation of the received level of each pulse with range. Figures 6.1 to 6.7 show echogram of selected data set from the field trip. Because the recording begins at the start of the pulse emission, all figures show saturation in the first 100 to 1000 μs of the signal, which is equivalent to the transmitted pulse length as expected. However, all figures also show a constant noise of RL = $\sim$80 dB which was not accounted for the first 16 ms. This was picked up by the noise inducted by the transmit section of the circuit board unintentionally interacting with the receiver section. All figures also show a strong acoustic return that corresponds to the bottom at $\sim$218 m. They also show an acoustic layer between 80 and 120 m. It was mentioned by Stéphane Gauthier that this acoustic layer is

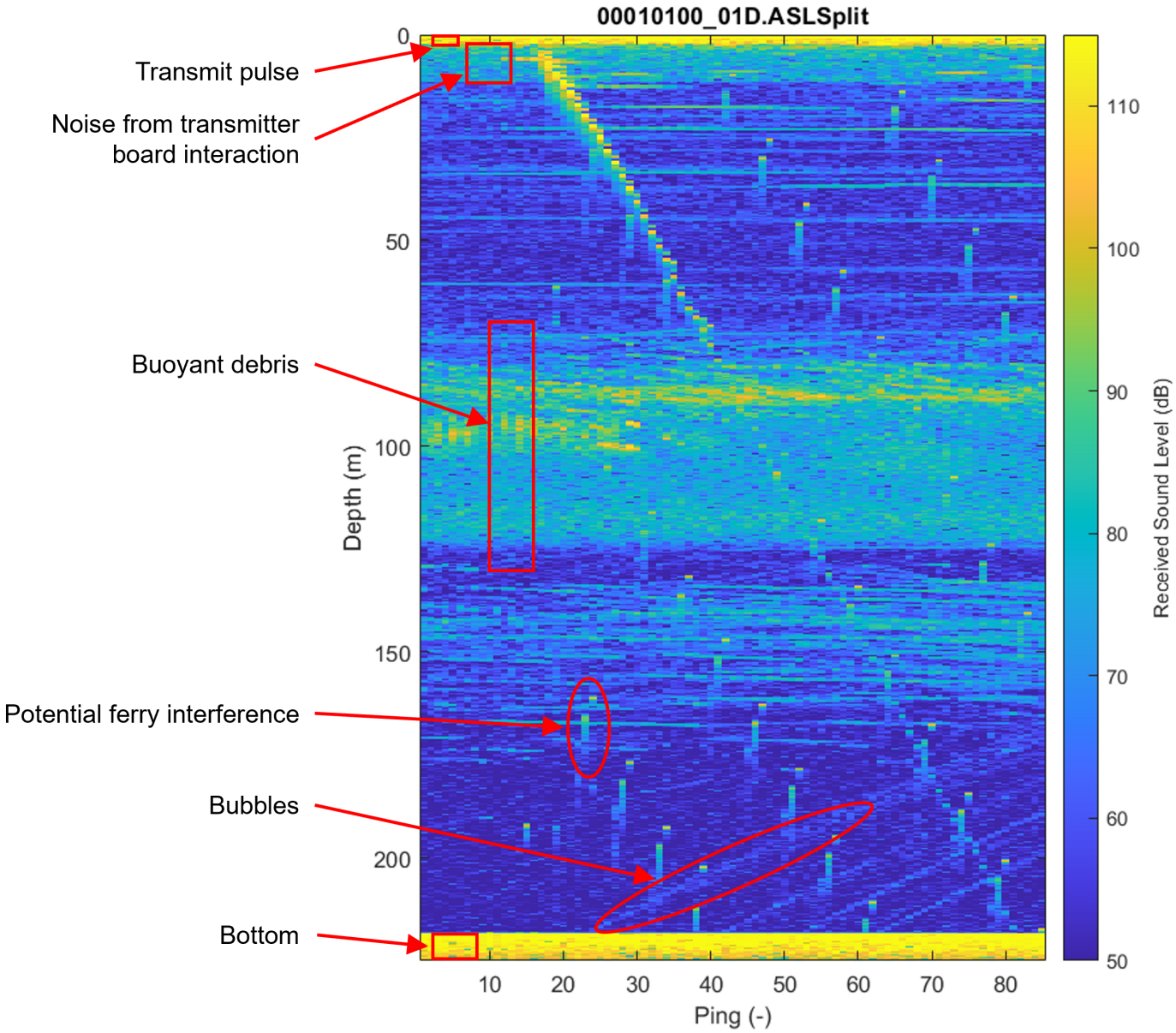

Figure 6.1: Echogram of dataset `00010100_01D.ASLSplit` with $\tau = 1000$ μs.

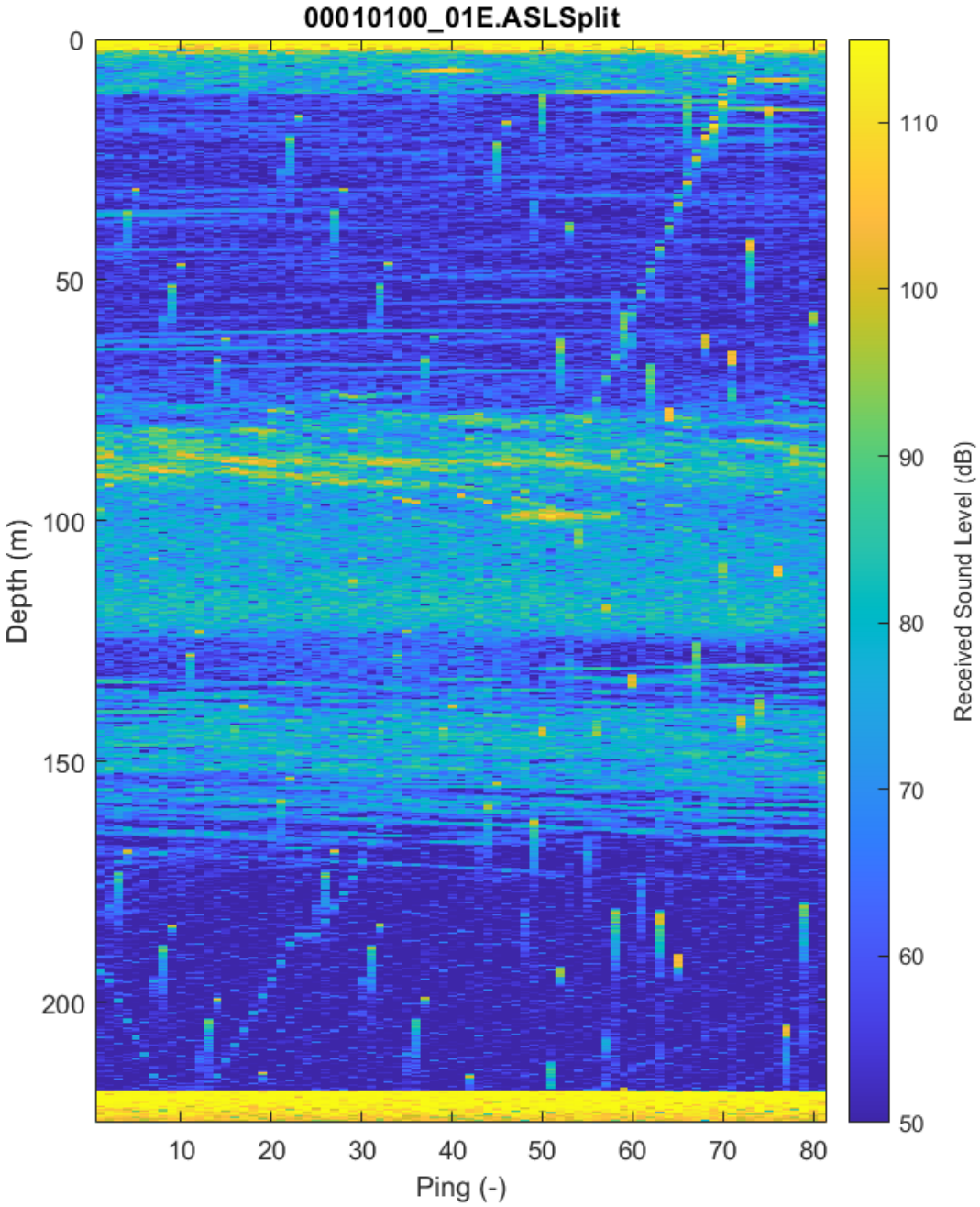

Figure 6.2: Echogram of dataset `00010100_01E.ASLSplit` with $\tau = 1000$ μs.

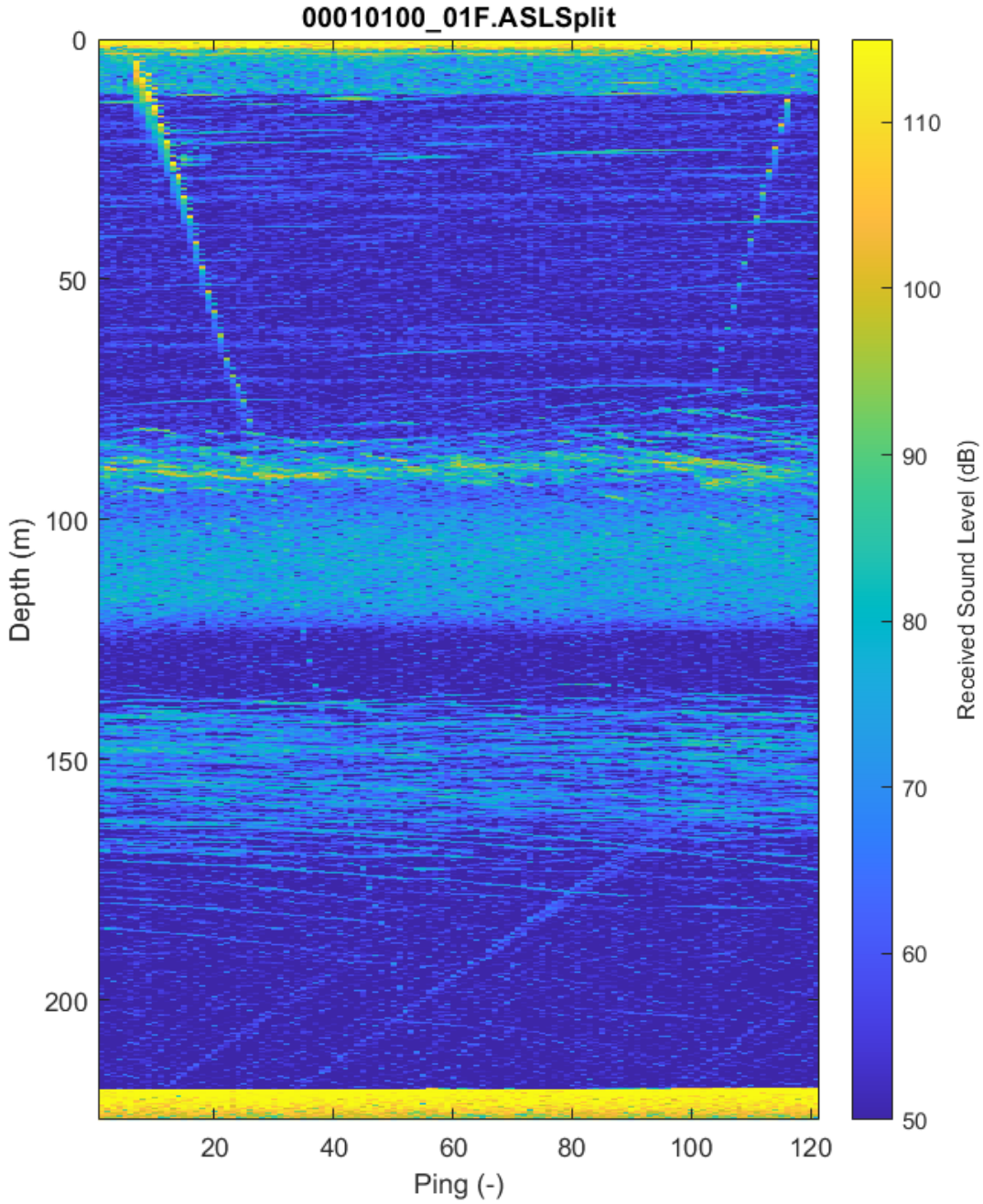

Figure 6.3: Echogram of dataset `00010100_01F.ASLSplit` with $\tau = 500$ μs.

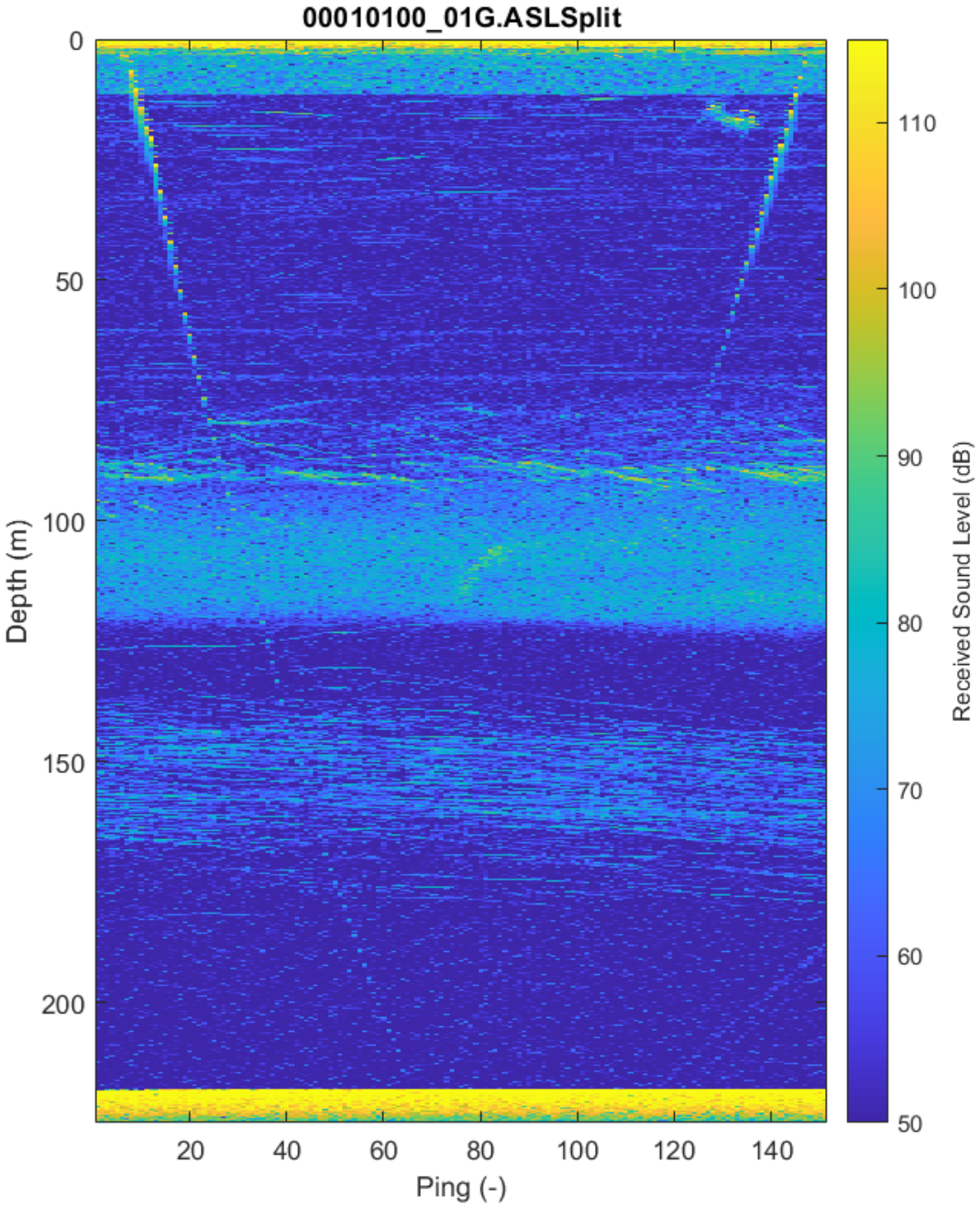

Figure 6.4: Echogram of dataset `00010100_01G.ASLSplit` with $\tau = 300$ μs.

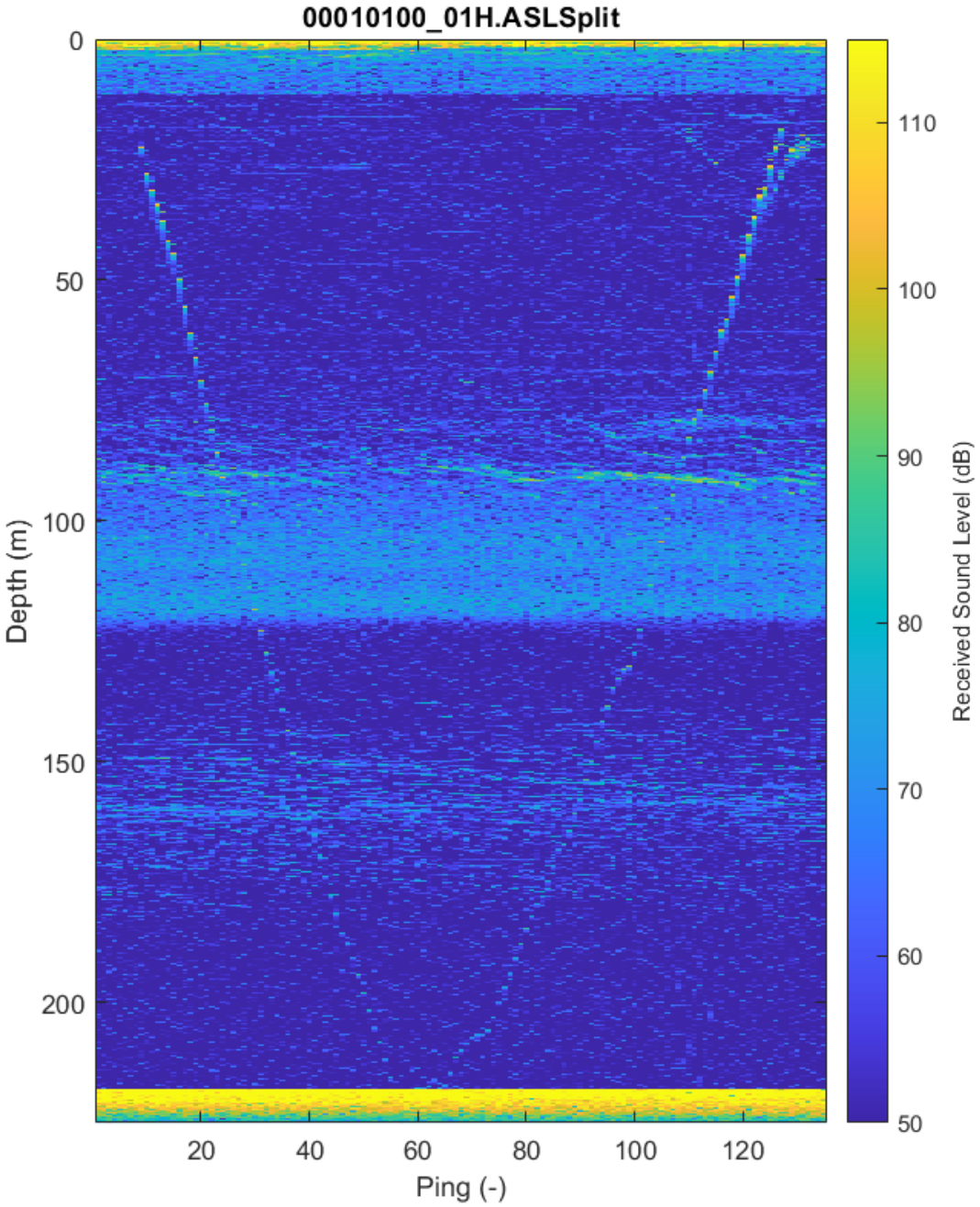

Figure 6.5: Echogram of dataset `00010100_01H.ASLSplit` with $\tau = 100$ μs.

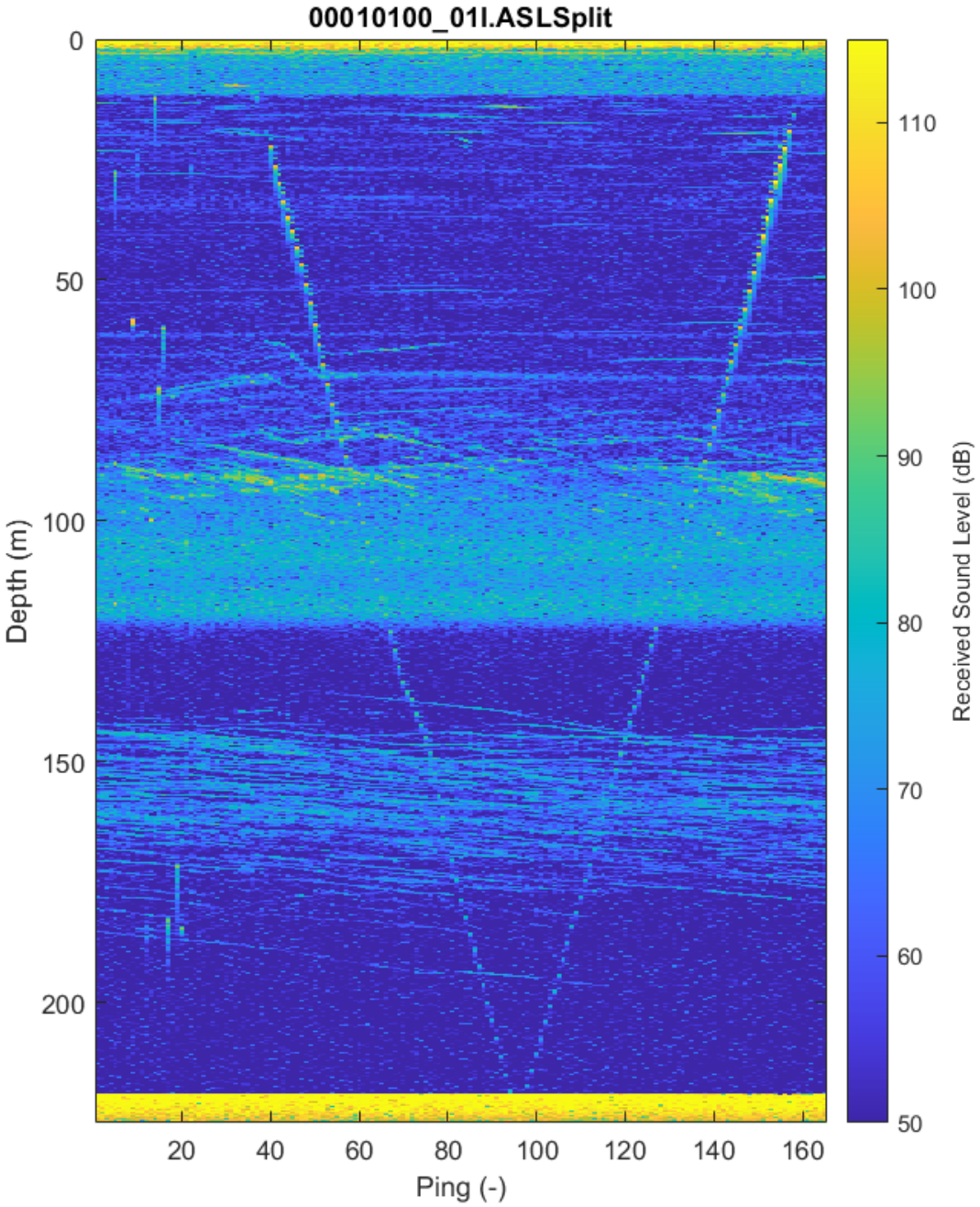

Figure 6.6: Echogram of dataset `00010100_01I.ASLSplit` with $\tau = 500$ μs and $f_s = 560$ kHz.

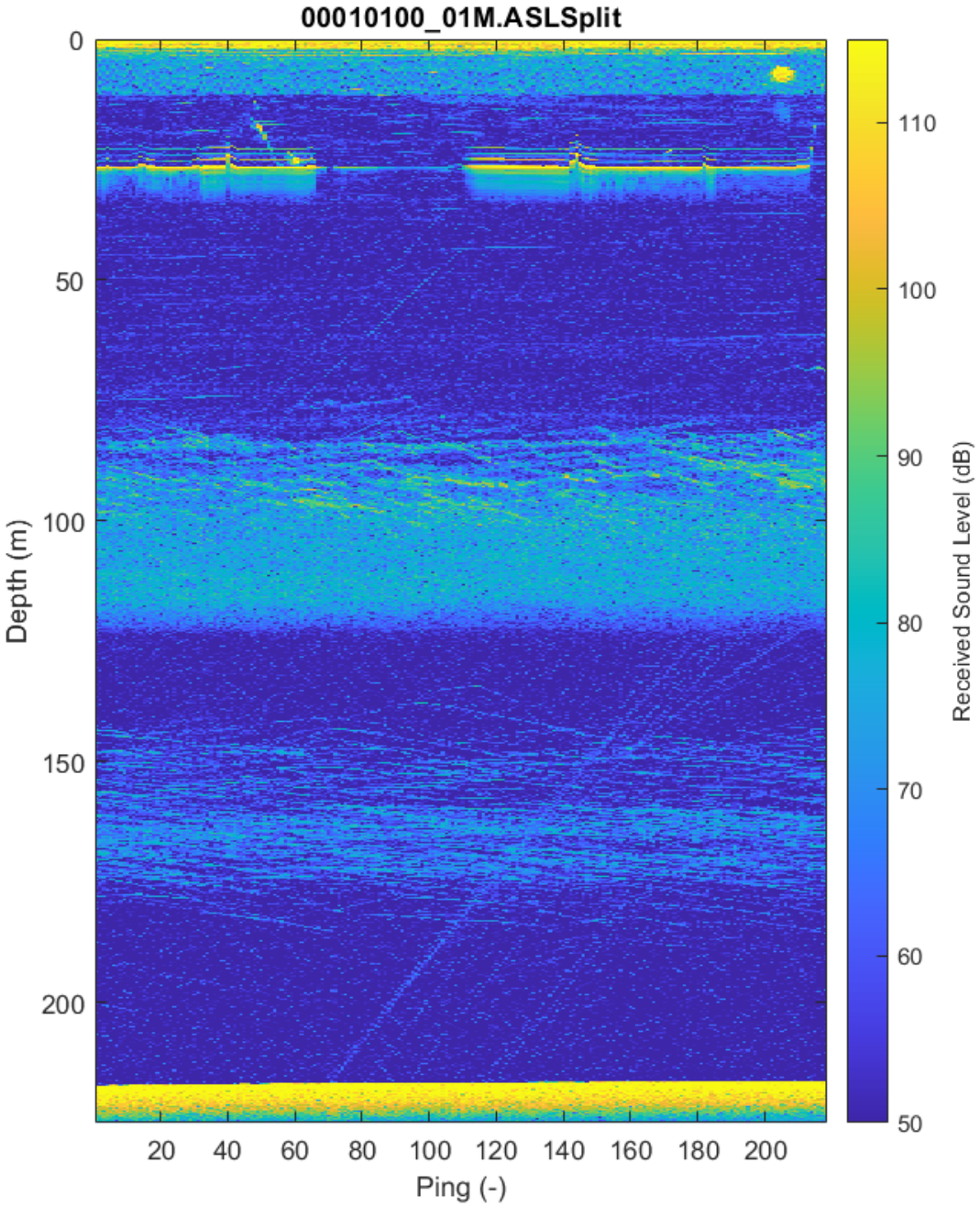

Figure 6.7: Echogram of dataset `00010100_01M.ASLSplit` with $\tau = 300$ μs.

caused by a layer of buoyant debris from a sill at ∼80 m in Saanich Inlet. Most figures also show diagonal lines elevating from the ocean bottom. These were assumed to be bubbles raising from the bottom, because gas bubbles are very visible acoustically and were rising with time.

Figures 6.1 to 6.6 show the acoustic trace of the targets lowered to the ocean bottom. The large weight sphere was visible in the entire water column, while the calibration sphere was usually visible for the first 90 metres. Figure 6.7 shows the data recorded with the targets at constant depth of ∼25 m. The targets were moved around the vessel so that the targets would appear in different parts of the acoustic beam to allow assessment of the directional compensation, which explains the variability in intensity throughout the recording.

Figures 6.1 and 6.2, as well as the first 20 pings of Figure 6.6, show vertical lines suspected to be interference with a radar or an echosounder on board the Brentwood Bay-Mill Bay ferry that was passing by around a 100 meters away from the location of the field trials. Pings affected by this interference were removed from the analysis.

6.1.3 Target strength measurements

Using the data analysis tools developed with the model to identify the targets in every ping. Figure 6.8 shows an example of a ping where the four elements on the fishing line appear both in received amplitude and phase difference. The four peaks in amplitude represent the piece of tape, the swivel, the calibration target, and the weight sphere in order. With the phase difference of both channels stabilizing around the targets, the data was filtered to only preserve the parts of the signal where the

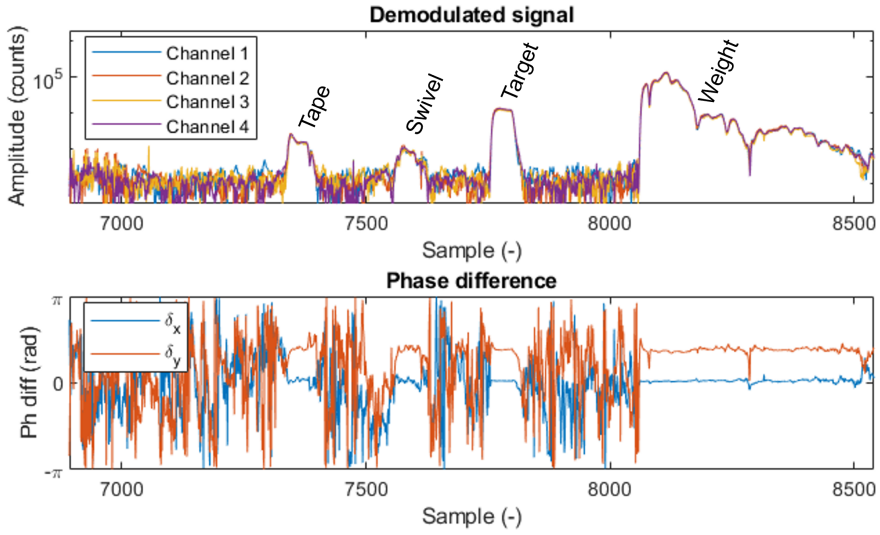

Figure 6.8: Demodulated signal of the 16th ping of `00010100_01G.ASLSplit` showing the four targets on the fishing line and the corresponding phase differences.

variability of the phase difference is small for the duration of the pulse length. The results of the filtered data with the echogram of `00010100_01M.ASLSplit` are shown by Figure 6.9. The calibration sphere was manually identified in every ping, allowing the position and target strength measurement to be extracted.

Figure 6.10 to 6.16 show the measured TS results of each data set using the same data presentation as used in chapter 4, using with a representation of the position and measured TS from a top view in sub-figures **a)**, a three-dimensional representation of the position and measured TS in **b)**, a scatter plot of the TS sorted by angle θ in **c)**, and a histogram plot with the mean TS value and the standard deviation in **d)**.

All datasets showed measured TS value within the range of -56.3 to -52.2 dB, with a mean TS measured at -53.76 dB. Figures 6.11, 6.12 and 6.13 clearly show larger angles when the sphere was reeled back to the surface from the drifting of the vessel,

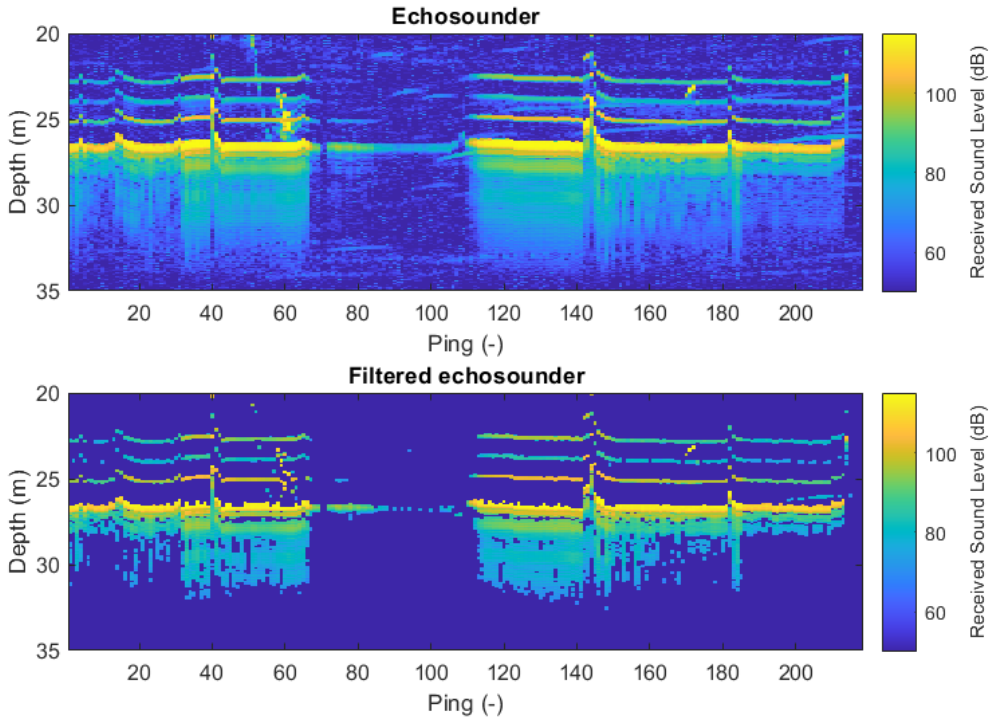

Figure 6.9: Echogram of dataset `00010100_01M.ASLSplit` and filtered data to identify targets with stable phase difference for duration longer than the pulse length.

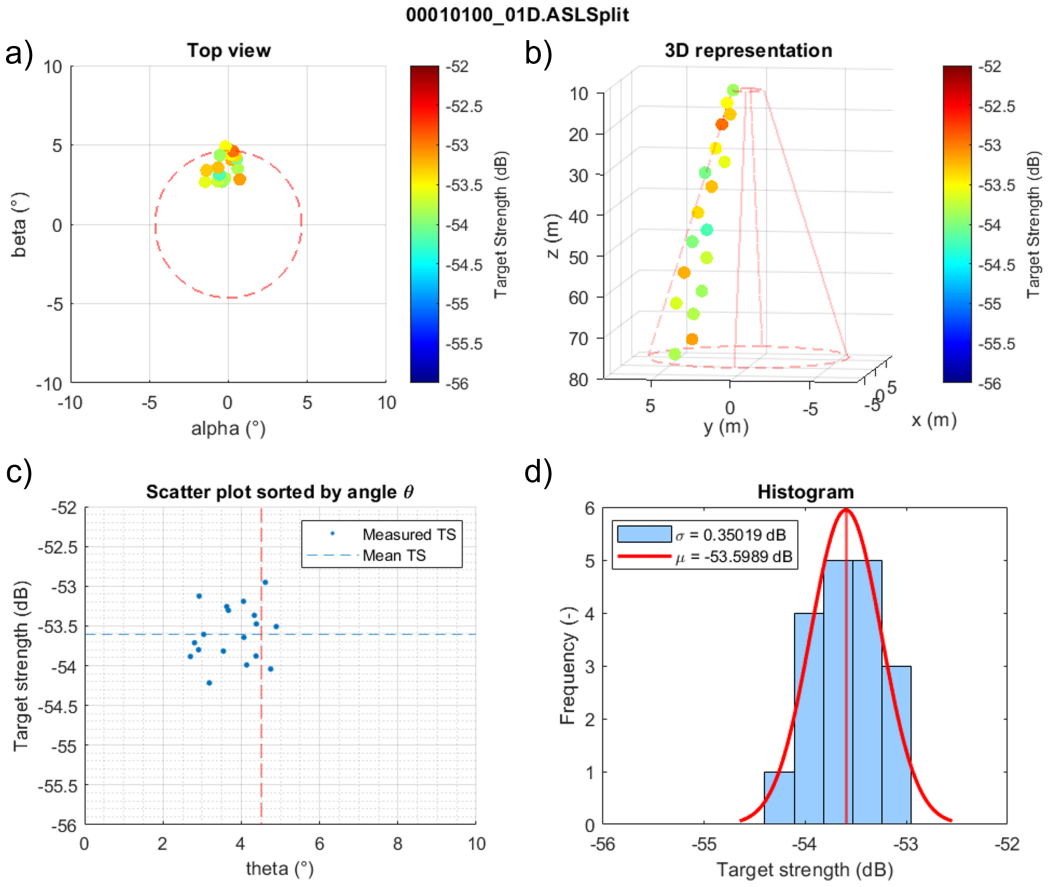

Figure 6.10: Measured target strength of the calibration sphere dataset `00010100_01D.ASLSplit` with $\tau = 1000$ μs. The dashed red line represents the -3 dB beamwidth.

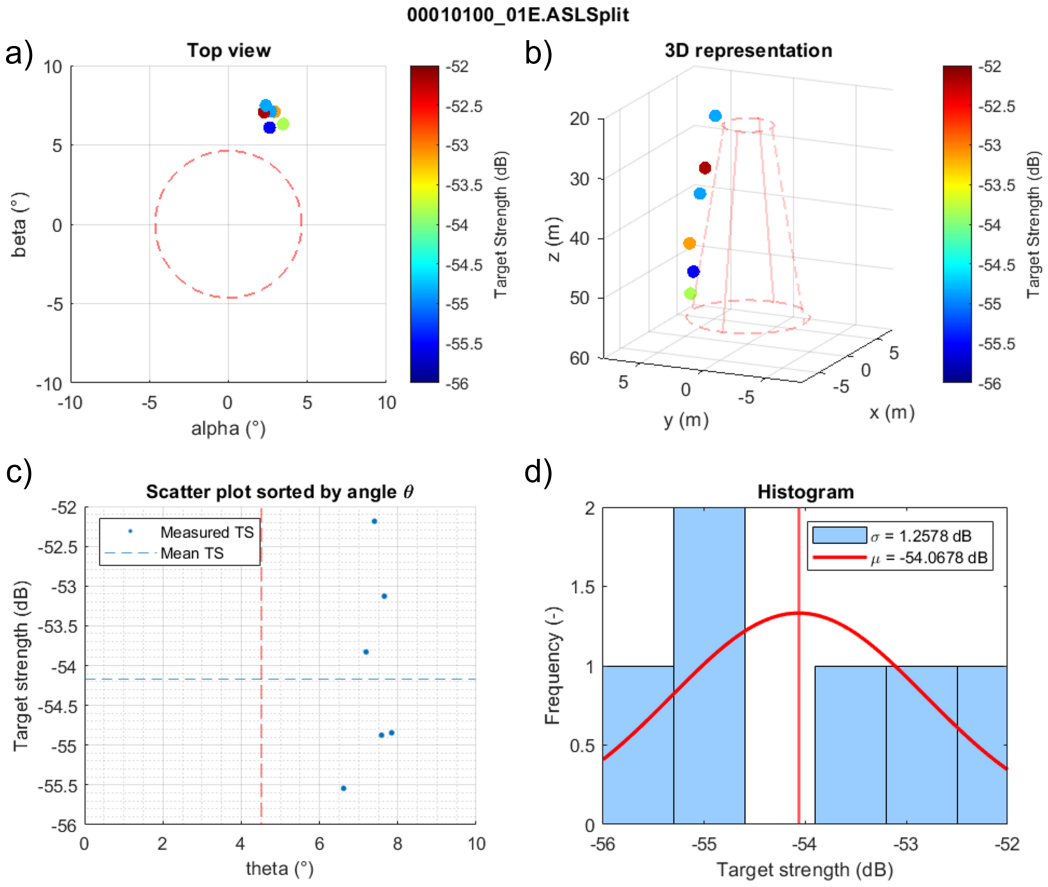

Figure 6.11: Measured target strength of the calibration sphere dataset `00010100_01E.ASLSplit` with $\tau = 1000$ μs. The dashed red line represents the -3 dB beamwidth.

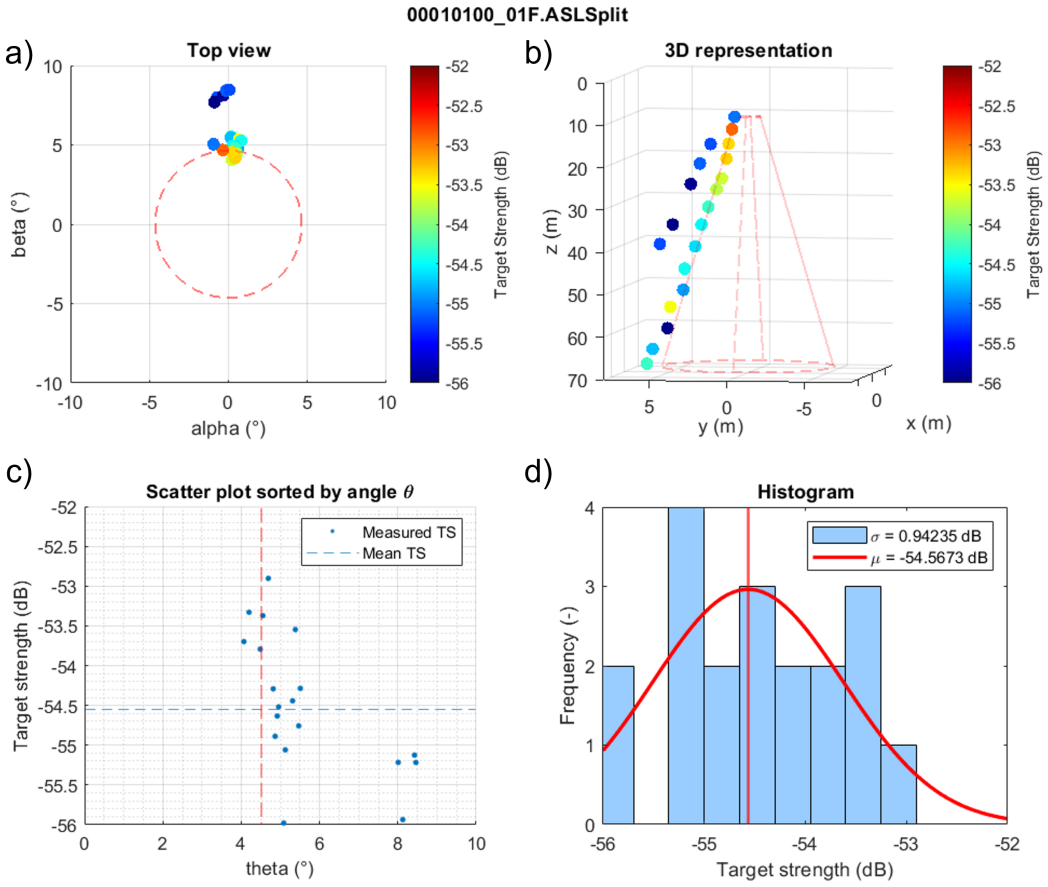

Figure 6.12: Measured target strength of the calibration sphere dataset `00010100_01F.ASLSplit` with $\tau = 500$ μs. The dashed red line represents the -3 dB beamwidth.

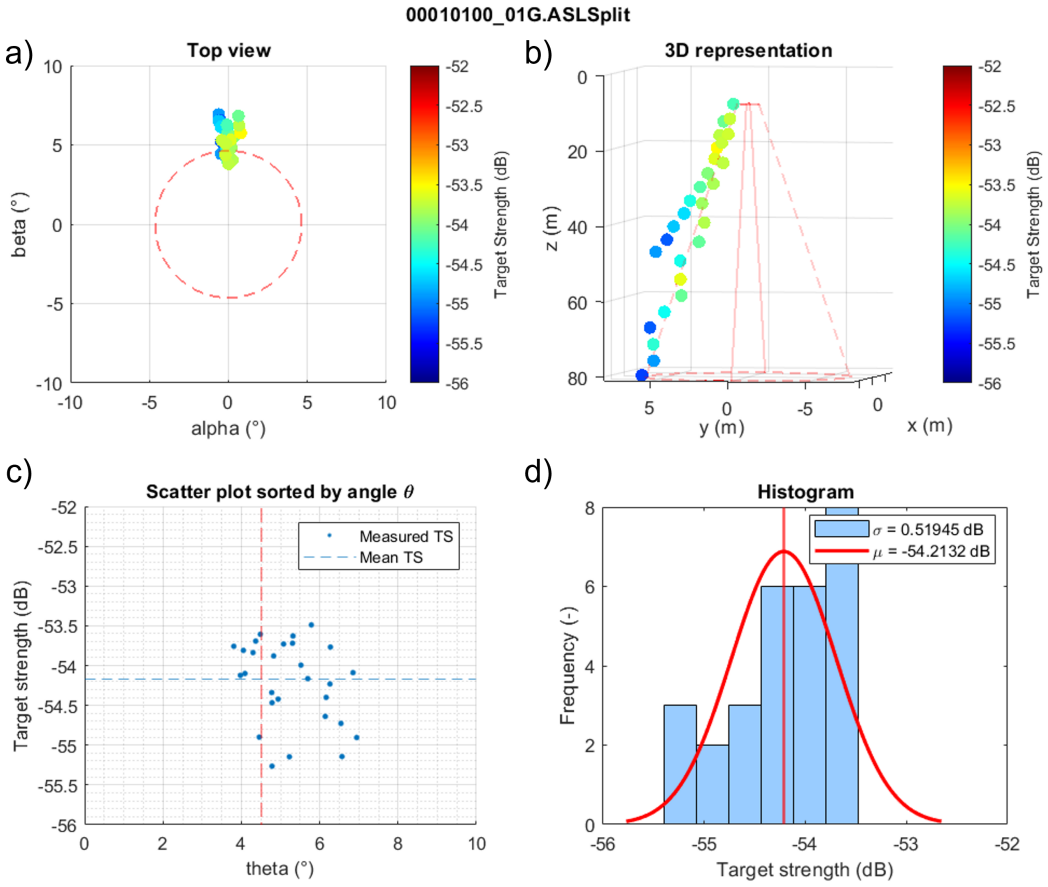

Figure 6.13: Measured target strength of the calibration sphere dataset `00010100_01G.ASLSplit` with $\tau = 300$ μs. The dashed red line represents the -3 dB beamwidth.

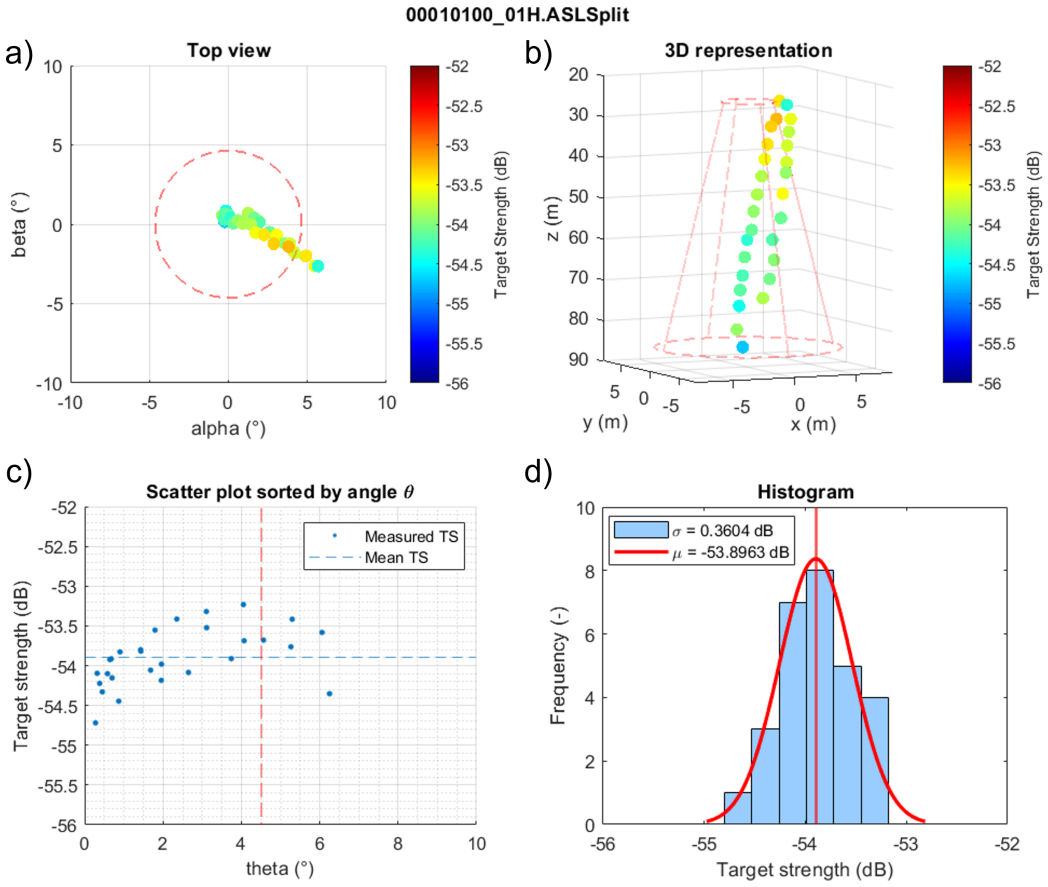

Figure 6.14: Measured target strength of the calibration sphere dataset `00010100_01H.ASLSplit` with $\tau = 100$ μs. The dashed red line represents the -3 dB beamwidth.

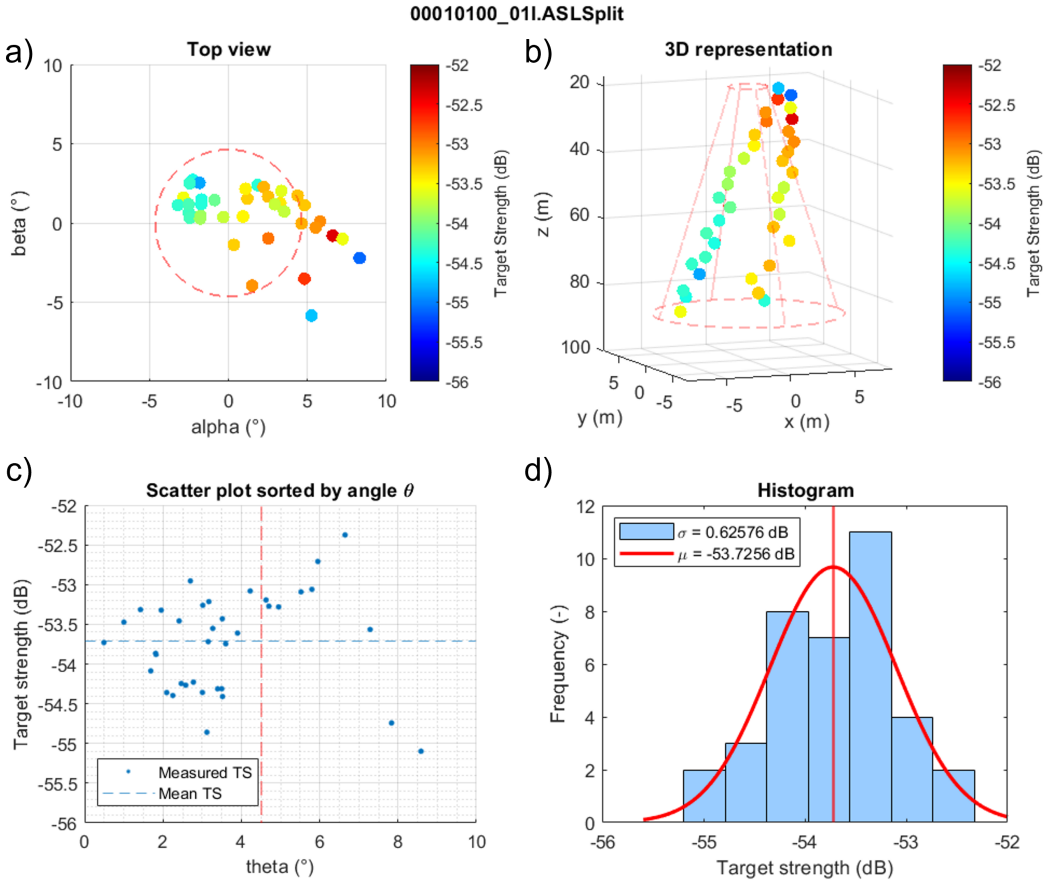

Figure 6.15: Measured target strength of the calibration sphere dataset `00010100_01I.ASLSplit` with $\tau = 500$ μs and $f_s = 560$ kHz. The dashed red line represents the -3 dB beamwidth.

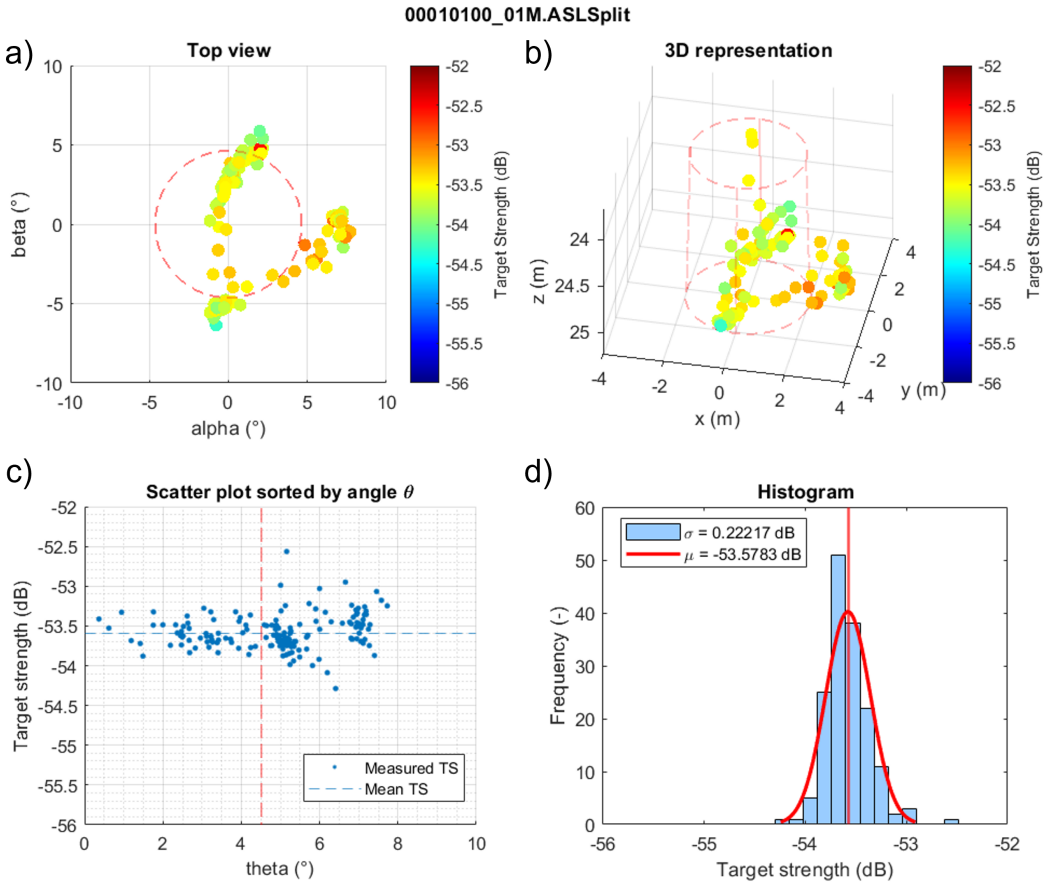

Figure 6.16: Measured target strength of the calibration sphere dataset `00010100_01M.ASLSplit` with $\tau = 300$ μs. The dashed red line represents the -3 dB beamwidth.

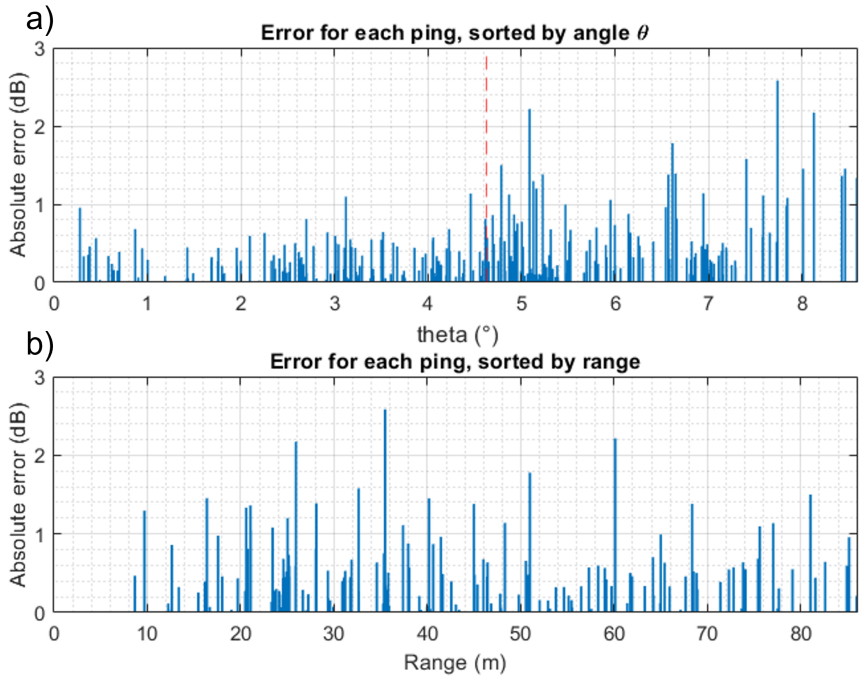

Figure 6.17: Absolute error bars for each ping with a detected target, sorted by angle θ (**a**)) and by range (**b**)).

resulting in a larger uncertainty in TS measurement due to smaller SNR. Figures 6.14 and 6.15 show datasets from the recording where the targets were dropped from port side, showing more data points within the -3 dB beamwidth. Figure 6.16 shows the measured TS for echoes covering all sides of the vessel at a constant range.

The error was obtained by comparing each detected target with the mean TS value of -53.76 dB. Over 297 pings with a detected target, the mean absolute error was 0.37 dB. The maximum absolute error over all the data was 2.58 dB, that reduces to 1.14 dB within the -3 dB beamwidth. The mean error is 0.28 dB under the -3 dB beamwidth, and increases to 0.44 dB at larger angles. As shown by Figure 6.17, no pattern dependence with range is observed. Using the same method described

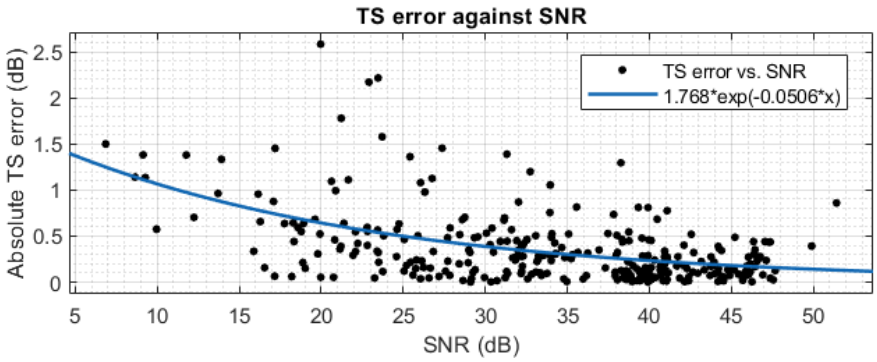

Figure 6.18: Comparison of the target strength for each ping with a detected target with the signal-to-noise ratio.

in section 4.3.1, the comparison of TS error with SNR from Figure 6.18 shows an increase in error with decreasing SNR.

6.2 Comparison with the model simulations

The simulations report a mean target strength of -53.4 dB but this value was forced to match the field trial observations where the mean TS of -53.76 was observed. However, meaningful comparisons between model and observations can be considered in measurement accuracy as evaluated through sample standard deviations. With the TOI at a range 25 m, the simulation from section 4.1 predicted a standard deviation of $\sigma = 0.11$ dB without noise, while the simulation from section 4.3.1 predicted $\sigma = 0.34$ dB with an noise added down to an SNR of 13.7 dB at $\theta = 8.7°$. The dataset `00010100_01M.ASLSplit` yields a standard deviation of $\sigma = 0.22$ dB. Thus, the dataset with the calibration sphere at a constant range falls between the two values predicted by the model, supporting the consistency of the model with the field

κ	f_s (kHz)	$\overline{\text{TS}}$ (dB)	σ (dB)
1	280	-53.58	0.22
2	93.33	-53.61	0.24
3	56	-53.62	0.29
4	40	-53.78	0.29
5	31.11	-53.80	0.38
6	25.45	-54.00	1.04

Table 6.2: Comparison of the target strength of dataset `00010100_01M.ASLSplit` for various sampling frequencies.

trials. Additionally, figures 4.7 and 6.18 show comparable curves, where the absolute error in TS measurement increases at lower SNR. The model simulations predicted a curve going from an error of 0.1 dB at SNR = 45.0 dB to an error up to 1.5 dB at an SNR of 13.7 dB, and the field trials yield a curve with an error of 0.2 dB at SNR = 45.0 dB to an error of 1.3 dB at SNR = 6.9 dB.

The change in transmit pulse length between the dataset results show no significant variation in the mean target strength measurement. All datasets show $\bar{\text{TS}}$ between -54.6 and -53.6 dB with no clear correlation with the change of pulse length from 100 to 1000 μs. This matches the prediction of the model from section 4.3.2 that showed no significant change in mean target strength and standard deviation from the pulse length. The exception is with the pulse length of 100μs in the model simulation, which yielded different results due to bandwidth effects.

Similarly to the exercise done in section 4.3.3, the field trials data was downsampled to values of the digital demodulation coefficient κ to study the impact over the

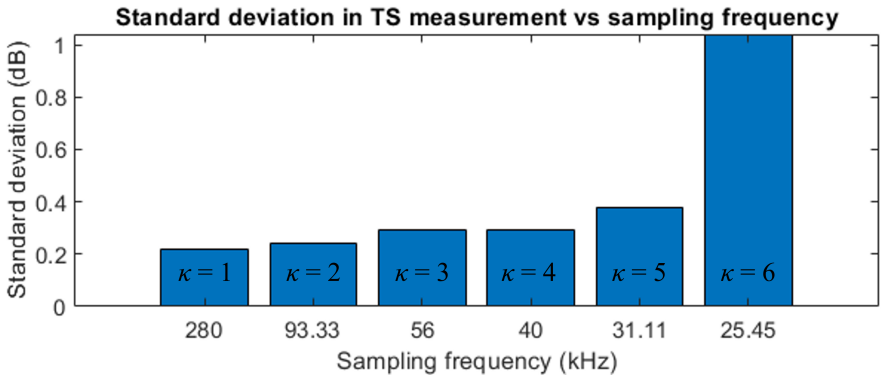

Figure 6.19: Comparison of the standard deviation over the target strength measurement of dataset `00010100_01M.ASLSplit` with the sampling frequency given by the digital demodulation coefficient κ.

results. Using dataset `00010100_01M.ASLSplit`, Table 6.2 shows the mean target strength is kept within the range of -53.58 and -53.80 dB for values of κ from 1 to 5, and the variation in the standard deviation is illustrated by Figure 6.19. As expected from the model results shown by Figure 4.9, the standard deviation increases slightly with lower sampling frequencies, but not significantly for values under $\kappa = 6$. The smallest sampling frequency studied, $f_s = 25.45$ kHz, is too close to the bandwidth of $B = 7$ kHz to ensure the preservation of the information.

Chapter 7

Summary and discussion

This thesis reports on the development of a split-beam sonar system. A computer model was developed that allowed simulation of various acoustic beam and backscatter signal building to predict sonar performance. Model results guided the development of a prototype system. Performance of ASL Environmental Sciences' AZFP-Split prototype system in field trials confirmed the model capabilities.

7.1 Model results

The ability to compute beam patterns from transducer geometries guided the work with ASL Environmental Sciences before committing to a hardware design. In particular, model trials of the four elements 308 kHz transducer demonstrated the separation between the elements was much larger than the order of the wavelength leading to large ambiguity in the acoustic beam phase. As a result, the project went on using the Airmar M475 transducer. The beam pattern modelling also provided predictions on the intensity and phase behaviour of the chosen transducer, allowing us to generate

$z_{\min}, z_{\max}$ (m)	n_i (particles)	τ (μs)	f_s (kHz)	$\overline{\text{TS}}$ (dB)	σ (dB)	MAE_θ (°)
[23, 27]	1	500	280	-53.44	0.11	0.046
[20, 105]	1	500	280	-53.42	0.11	0.045
[23, 27]	300	500	280	-53.45	0.34	0.065
[20, 105]	2000	1000	280	-53.36	0.13	0.040
[20, 105]	2000	500	280	-53.41	0.08	0.036
[20, 105]	2000	300	280	-53.42	0.08	0.034
[20, 105]	2000	200	280	-53.49	0.08	0.029
[20, 105]	2000	100	280	-56.30	0.10	0.031
[20, 105]	2000	500	280	-53.41	0.08	0.032
[20, 105]	2000	500	93.33	-53.41	0.12	0.045
[20, 105]	2000	500	56	-53.40	0.16	0.042
[20, 105]	2000	500	40	-53.43	0.18	0.040
[20, 105]	2000	500	31.11	-53.49	0.26	0.055
[20, 105]	2000	500	25.45	-53.52	0.29	0.061

Table 7.1: Summary of measured target strength values and mean absolute error of the angular measurement from the model simulations.

data processing algorithms needed for the calibration process.

The beam pattern and backscatter signal simulations were used to identify the limitations of the system. The angular limit for which a target can be processed was obtained through a mix of theoretical equations and model confirmation, providing a more accurate threshold limit for split-beam sonar systems than the arbitrary intensity beamwidth. The limitation from the data loss for a given target backscattered echo in a noise floor can also be computed from the model.

Having an accurate depiction of the beam pattern allowed testing of data processing techniques to improve results. Matching the angular position measurement equations to the phase maps improved the precision and accuracy of the position measurement of the target from the traditional linear approximation described in the literature. The error of over 1° was observed for the measured position of particles within the -12 dB beamwidth when using the linear method and was reduced to 0.15° by a polynomial method with the coefficients derived from the beam pattern.

The ability to simulate a backscattered signal from a target with a split-beam transducer provided insight on the sonar performance. Table 7.1 presents a summary of the simulations featured in chapter 4. The simulation run with a singular particle, i.e. without noise, showed a standard deviation of $\sigma = 0.11$ dB, demonstrating the efficiency of the data processing algorithm. While the mean TS value remained virtually unchanged, the standard deviation increased with the addition of noise in the system to 0.34 dB from simulations with 300 particles due to the SNR decreasing to 13.7 dB at the edge of the beam. This is due to the decrease of SNR at large angle, introducing variability in the intensity and phase and resulting in a drop in precision in the measurement. Further exploration of SNR with increasing noise in the

simulation could provide insight in the threshold of target detection in the instrument design.

The change in pulse length from 100 to 1000 μs showed virtually no difference to the results, except for $\tau = 100$ μs. The reduced response at extremely short transmit pulse is due to the bandwidth filter of the pulse template restraining the amplitude of the pulse.

The change in sampling frequency indicated that the data processing would yield similar average TS values. As expected, the chosen sampling frequency values for the digital demodulation method respect the equations described by Lyons (2011) and preserve the information in phase and amplitude, allowing sampling at values lower than the carrier frequency. An increase of $\sigma = 0.21$ dB in the standard deviation between sample rates of 280 to 31.11 kHz is observed, because the digital demodulation technique increases noise through aliasing out of band signals.

7.2 Field trials results

Algorithms for calibration and data processing of the AZFP-Split prototype were derived from the methods used in assessing model performance. A MATLAB program was created with the same data processing algorithm, allowing us to compute results for the prototype instrument data, as well as an easy way to improve the model based on the field trials results. The model was then used to compare its performance to the AZFP-Split prototype field trials. It is important to note that the TS value chosen for the TOI in the model simulations was arbitrarily chosen to approximately represent a similar SNR with the background particles to the field trials. While the $\overline{\text{TS}}$ value

File name	n_{pi} (pings)	$\overline{\text{TS}}$ (dB)	σ (dB)
00010100_01D.ASLSplit	18	-53.60	0.35
00010100_01E.ASLSplit	6	-54.07	1.26
00010100_01F.ASLSplit	20	-54.57	0.94
00010100_01G.ASLSplit	28	-54.21	0.52
00010100_01H.ASLSplit	28	-53.90	0.36
00010100_01I.ASLSplit	37	-53.73	0.63
00010100_01M.ASLSplit	160	-53.58	0.22
Sum	297	-53.76	0.54

Table 7.2: Summary of measured target strength values for the calibration sphere during the field trials.

might differ between model simulation and field trials, the precision and accuracy of the instrument was compared.

The average received level for the noise measurement was around 47 dB. The noise decreased from 49.0 dB to 46.1 dB between the measurements made at 10:12 and 11:33, suggesting a change in the prevailing noise levels with the position of the vessel. The SNR of the backscattered signal was sufficient to process the data.

The prototype instrument successfully transmitted pulses of sound of various pulse lengths and recorded the backscattered echo at various sampling frequencies over seven datasets. Only dataset 00010100_01L.ASLSplit ended up failing due to mistakes made on the on-board setting configurations.

At full power, the maximum range recorded for the -53 dB calibration sphere was 85.98 metres. The weight sphere was visible over the entire 220 m range, and the

other elements on the line, such as the swivel and the piece of tapes, were even visible for the first ~ 50 m.

The NOAA's Standard Sphere Target Strength Calculator estimated the TS value of the calibration sphere to -53 dB. The mean measured value was slightly lower than the expected -53 dB, but the results were consistent between datasets. As shown by Table 7.2, all datasets results were within the range of -54.57 to -53.58 dB, with a mean TS measured at -53.76 dB, and an average standard deviation of 0.54 dB. With targets measured at angles θ up to 8.6° and at ranges from 8.7 to 86.0 metres, the data analysis algorithm proved to properly compensate the measured target strength in range and in DOA.

An important detail to point out is the lack of coverage of sphere detection in the beam. As shown by the measured position of the calibration sphere in Figures 6.10 to 6.16, the sphere detection did not cover the whole beam.This was due to the limitation of the setup during the field trials, time limitation with the calibration process, and the limited ping rate of the prototype hardware. Demer et al. (2015) mentions a minimum of 100 detections evenly distributed throughout the -3 dB beamwidth and covering all four quadrants is needed to precisely calibrate the instrument and accurately measure the angle and TS. Since the field trip data did not cover the entire beam, the exact shape of the beam and the TS at different angles in all four quadrants could not be calculated empirically. This prevented a direct comparison and validation of the model. It is worth noting that the model could be used to quantify the uncertainties from the number of detection in calibration and predict the accuracy from any amount of samples based of the position of the calibration sphere in the beam.

As predicted by the model simulation, the sampling frequency and pulse length

had no significant impact on the target strength measurement. Differences in the maximum range for the calibration sphere with pulse length were observed. However, the position of the sphere in the beam played an important role in its detectability. The trials would need to be in more controlled conditions to provide information on the impact of pulse length over the range. As for the post-processing downsampling, the change in standard deviation with the integer κ match closely the predictions from the model, indicating the ability to sample at smaller frequencies than the carrier while preserving the information. The advantage of using subsampling, including lower power consumption and smaller data files, and the method will be considered in future revision of ASL Environmental Sciences' split-beam system.

7.3 Future work

The model presents opportunities to explore other areas of sonar processing. The capability of the model allows to simulate and predict the sonar performance with various parameters and processing techniques before the hardware design process. Multiple sonar methods that were not explored as part of this thesis shows potential to improve target strength measurement, as well as potential algorithms to separate overlapping targets from the signals.

To model the sonar efficiency of a biological target and compute accurate depiction of the swim bladder morphology, introducing a more complicated target structures would be required to ensure accurate measurements, rather than point scatterers. Different approaches have been established to model realistic shapes of biological target for backscattered target strength measurement. Kirchoff ray-mode approximation

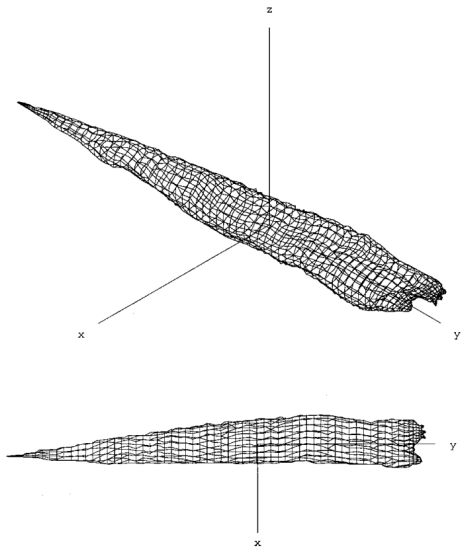

Figure 7.1: Boundary element mesh (BEM) of the swim bladder of a pollack shown in both oblique and dorsal views. Reproduction of Figure 1 from Foote and Francis (2002) with permission.

(KRM), as described by Foote (1985), and the boundary element method (BEM), as described by Foote and Francis (2002) could be considered to be added to the model. Figure 7.1 shows an example of a three-dimensional digital map of the nodes used for these two methods.

The results of the model and the field trials could be improved by using a sound speed profile instead of a constant value of $c = 1450$ m/s. This would lead to more accurate measured target range r, and therefore more accurate compensation over the transmission loss TL and absorption loss AL, as a difference of 50 m/s can yield over 0.3 dB of error in the target strength measurement. The CTD cast from the field trials showed variation of less than 0.2° C from 5 to 50-metre range, indicating a good approximation of a constant sound speed value. In a warmer, saltier, or more

complex water column, using a sound speed profile to compute the data would be beneficial to increase the accuracy of the measurement.

Position estimation of TOI could be improved by increasing the number of receivers. Split-beam sonar algorithms are relying on two pairs of receivers to compute the position in the x and y axes. Providing a transducer with more independent receivers allow more accurate tracking, and the positional errors can be estimated through statistical analysis of redundant measurements. The model could be used to explore the potential benefits of this method.

The prototype system is transmitting a continuous wave (CW) tone pulse at a bandwidth for its purpose, i.e. around 10% of the carrier frequency. In principle, the more frequencies there are in a signal, the more information is conveyed from the source to the receiver. Holliday (1977) suggested that the size of fish relates to the resonance frequency of the swim bladder. This frequency can be determined from the spectrum of echoes generated by a broadband source. Broadband sonar can be simulated in the model by changing the bandwidth parameters in the pulse template function. Another way to achieve broad bandwidth signals is by using frequency-modulated transmissions, or a chirp. A chirp sonar is a system in which the transmitted frequency increases or decreases with time. The model includes a mean of implementing chirp signals as they were incorporated into the coherent Doppler sonar model (Zedel (2008)) it is based from. However, the performance of chirps pulses were not studied, because it was not planned to be a feature on the AZFP-Split prototype. Future system prospect using chirp or broadband signal could be studied using the model.

Methods described by Bofill and Zibulevsky (2001) and algorithms developed by

Yu (2019) have been considered to separate the TS measurement of two targets at the same range. However, the bandwidth of the prototype system proved to be insufficient to use these methods. Better results of the blind source separation algorithms could be achieved by using broadband, chirps or multiple frequency simulations. The model would provide an efficient tool to compare and test the efficiency of various source separation algorithms and scenarios.

The model could be adapted to a list of transducer designs and parameters, allowing to predict the performance of a large variety of echosounder designs. By considering the specific characteristics and technical specifications of the alternative equipment, a comprehensive list of pros and cons for any given design could help the industry in committing to a specific design. Modifications can be easily accounted in the model setup to account for variations in pulse length, sampling frequency, and beam geometry. A thorough understanding of the distinct functionalities and performance attributes of the specific echosounder in question is crucial for a successful adaptation of the split-beam sonar model to ensure accurate simulations and insights for any potential uses of the instrument.

Bibliography

Bofill, Pau and Michael Zibulevsky (2001). "Underdetermined blind source separation using sparse representations". In: *Signal Processing* 81(11), pp. 2353–2362. ISSN: 0165-1684. DOI: 10.1016/S0165-1684(01)00120-7.

Demer, David A. et al. (Jan. 2015). "Calibration of acoustic instruments". In: DOI: 10.17895/ices.pub.5494. URL: https://ices-library.figshare.com/articles/report/Calibration_of_acoustic_instruments/19056617.

Ehrenberg, John E. (1974). "Two applications for a dual-beam transducer in hydroacoustic fish assessment systems". In: *Ocean '74 - IEEE International Conference on Engineering in the Ocean Environment*, pp. 152–155. DOI: 10.1109/OCEANS.1974.1161349.

Ehrenberg, John E. (1989). "A Review of Target Strength Estimation Techniques". In: *Underwater Acoustic Data Processing*. Ed. by Y. T. Chan. Springer Netherlands: Dordrecht, pp. 161–176. ISBN: 978-94-009-2289-1. DOI: 10.1007/978-94-009-2289-1_17.

Ehrenberg, John E. and Thomas C. Torkelson (1996). "Application of dual-beam and split-beam target tracking in fisheries acoustics". In: *ICES Journal of Marine Science* 53(2), pp. 329–334. ISSN: 1054-3139. DOI: 10.1006/jmsc.1996.0044.

Foote, Kenneth G. (1979). "Fish target-strength-to-length regressions for application in fisheries research". In: *Proceedings of the ultrasonic international* 19, pp. 327–333.

Foote, Kenneth G. (1985). "Rather-high-frequency sound scattering by swimbladdered fish". In: *The Journal of the Acoustical Society of America* 78(2), pp. 688–700. ISSN: 0001-4966. DOI: 10.1121/1.392438.

Foote, Kenneth G. (1986). "Digital representation of split-beam-transducer beam patterns". eng. In: *ICES CM Documents*.

Foote, Kenneth G., Asgeir Aglen, and Odd Nakken (1986). "Measurement of fish target strength with a split-beam echo sounder". In: *The Journal of the Acoustical Society of America* 80(2), pp. 612–621. DOI: 10.1121/1.394056.

Foote, Kenneth G. and David Francis (2002). "Comparing Kirchhoff-approximation and boundary-element models for computing gadoid target strengths". In: *The Journal of the Acoustical Society of America* 111, pp. 1644–54. DOI: 10.1121/1.1458939.

Foote, Kenneth G., Finn Hogne Kristensen, and Haakon Solli (1984). "Trial of a New, Split-beam Echo Sounder". In: *International Council for the Exploration of the Sea*.

Holliday, D.V. (1977). "The use of swimbladder resonance in the sizing of schooled pelagic fish". In: *Rapp. P.-v. Reun. Cons. Int. Explor. Mer 170*, pp. 130–35.

Jech, J. Michael et al. (2005). "Comparing two 38-kHz scientific echosounders". In: *ICES Journal of Marine Science* 62(6), pp. 1168–1179. ISSN: 1054-3139. DOI: 10.1016/j.icesjms.2005.02.014.

Jones, Ian S. F. and Jishi Xie (1994). "A sound scattering layer in a freshwater reservoir". In: *Limnology and Oceanography* 39(2), pp. 443–448. DOI: 10.4319/lo.1994.39.2.0443.

Love, Richard H. (1971). "Dorsal-Aspect Target Strength of an Individual Fish". In: *The Journal of the Acoustical Society of America* 49(3B), pp. 816–823. ISSN: 0001-4966. DOI: 10.1121/1.1912422.

Lyons, Richard G. (2011). *Understanding Digital Signal Processing*. 3rd Edition. Pearson. ISBN: 013702741-9.

MacLennan, David N. and Ingvald Svellingen (1989). "Simple calibration of a split-beam echo-sounder". eng. In: *Fisk.Dir. Skr. Ser. Havunders.* 18, pp. 365–79.

McClatchie, S, G.J Macaulay, and R.F Coombs (2003). "A requiem for the use of 20 log10 Length for acoustic target strength with special reference to deep-sea fishes". In: *ICES Journal of Marine Science* 60(2), pp. 419–428. ISSN: 1054-3139. DOI: 10.1016/S1054-3139(03)00004-3.

Medwin, Herman (1975). "Speed of sound in water: A simple equation for realistic parameters". In: *The Journal of the Acoustical Society of America* 58(6), pp. 1318–1319. ISSN: 0001-4966. DOI: 10.1121/1.380790.

Medwin, Herman and Clarence S. Clay (1998). *Fundamentals of Acoustical Oceanography*. Applications of Modern Acoustics. Academic Press: San Diego, pp. 1–VI. ISBN: 978-0-12-487570-8. DOI: 10.1016/B978-0-12-487570-8.X5000-4.

Midttun, Lars (1984). "Fish and other organisms as acoustic targets". In: *Rapports et Proces-Verbaux des Reunions, ICES* 184, pp. 25–33.

Ona, Egil (1990). "Optimal acoustic beam pattern corrections for split beam transducers". In: ICES, 1990/B:30.

Ona, Egil (1999). *Methodology for Target Strength Measurements: With Special Reference to in Situ Techniques for Fish and Mikro-nekton : Prepared for the Study Group on Target Strength Methodology*. ICES cooperative research report. International Council for the Exploration of the Sea.

Shannon, C.E. (1949). "Communication in the Presence of Noise". In: *Proceedings of the IRE* 37(1), pp. 10–21. DOI: 10.1109/JRPROC.1949.232969.

Simmonds, E. John and David N. MacLennan (2005). *Fisheries acoustics : theory and practice*. eng. 2nd ed. Fish and aquatic resources series ; 10. Blackwell Science: Oxford ; Ames, Iowa. ISBN: 063205994X.

Traynor, J. J. and John E. Ehrenberg (1990). "Fish and standard sphere target strength measurements obtained with a dual-beam and split-beam echo-sounding system". In: *Rapports et Proces-Verbaux des Reunions, ICES* 189, pp. 325–335.

Vatnehol, Sindre N. and Egil Ona (2017). "Evaluation of target angular position algorithms for multi-beam fishery sonars". In: *The Journal of the Acoustical Society of America* 141(2), pp. 1074–1083. ISSN: 0001-4966. DOI: 10.1121/1.4974857.

Yu, Gang (2019). "An Underdetermined Blind Source Separation Method with Application to Modal Identification". In: *Shock and Vibration* 2019, pp. 1–15. DOI: 10.1155/2019/1637163.

Zedel, Len (2008). "Modeling Pulse-to-Pulse Coherent Doppler Sonar". In: *Journal of Atmospheric and Oceanic Technology - J ATMOS OCEAN TECHNOL* 25. DOI: 10.1175/2008JTECHO585.1.

Zedel, Len (2015). "Modelling Doppler sonar backscatter". In: *2015 IEEE/OES Eleveth Current, Waves and Turbulence Measurement (CWTM)*, pp. 1–5. DOI: 10.1109/CWTM.2015.7098132.

Appendix

A. Airmar M475 Data Sheets

Included in the following pages are the specification sheet provided by Airmar Technology Corporation for the M475 Split-Beam Transducer, and the directivity beam pattern of the transducer used by ASL Environmental Sciences for the AZFP-Split prototype at $f_c = 70$ kHz. Note that the beamwidth presented in the data sheet is defined as a full angle beamwidth, rather than the half-angle as defined in the thesis.

SPECIFICATIONS M475

Resonant frequency (nominal?)	None
Frequency range	58 kHz to 110 kHz
Circular beam width	8° @ 80 kHz
Directivity characteristics:	
D:	548 @80 kHz
DI:	26.9dB @ 80 kHz
Equivalent two-way beam angle:	Y = 0.012 steradians @ 80 kHz
Side lobes:	-30dB @ 80 kHz
Back radiation	-40dB @ 80 kHz
Nominal impedance	12.5 Ω
Transmitting response	180dB re 1µPa per volt @ 1m @ 80 kHz
Receiving sensitivity, open circuit	-187dB re 1volt per µPa @ 80 kHz
Electro-acoustic efficiency	32% @ 80kHz
Max pulse power input	1kw @ 1% duty
Max continuous input	15W
Cable diameter	Nominal 0.635" (16.15 mm)
Weight	17.35 Kg (38.25 lbs)
Storage temperature	Range: -20C to +60C (-4F to 140F)
Input power	1 kw @ 1% duty
Pulse length	Variable
Connector	Unterminated

DIMENSIONS M475

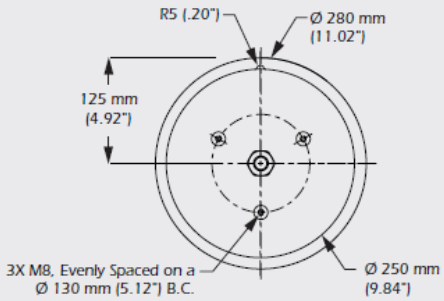

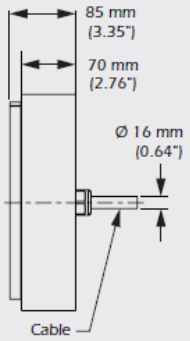

TRANSMIT RADIATION PATTERN M475

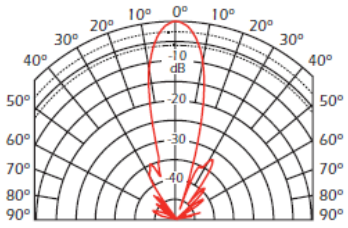

Beamwidth @ 60 kHz

-3 dB 10°

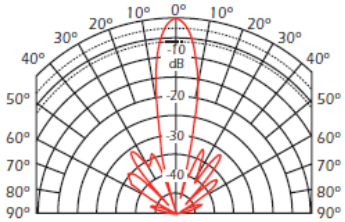

Beamwidth @ 80 kHz

-3 dB 8°

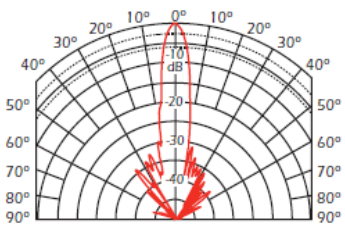

Beamwidth @ 110 kHz

-3 dB 5°

Wiring Diagram INterconnect M475

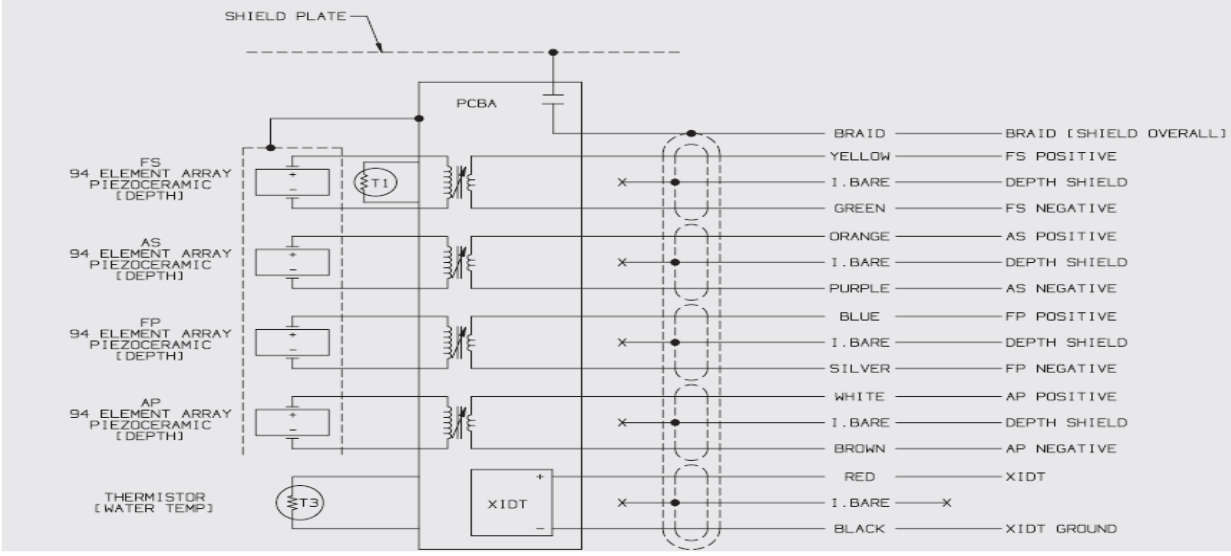

AIRMAR TECHNOLOGY CORPORATION
35 Meadowbrook Drive
Milford, New Hampshire 03055-4316, USA

Directivity Pattern

Customer: ASL
Airmar PN: M475
Serial #: 60173586
Frequency; 70kHz

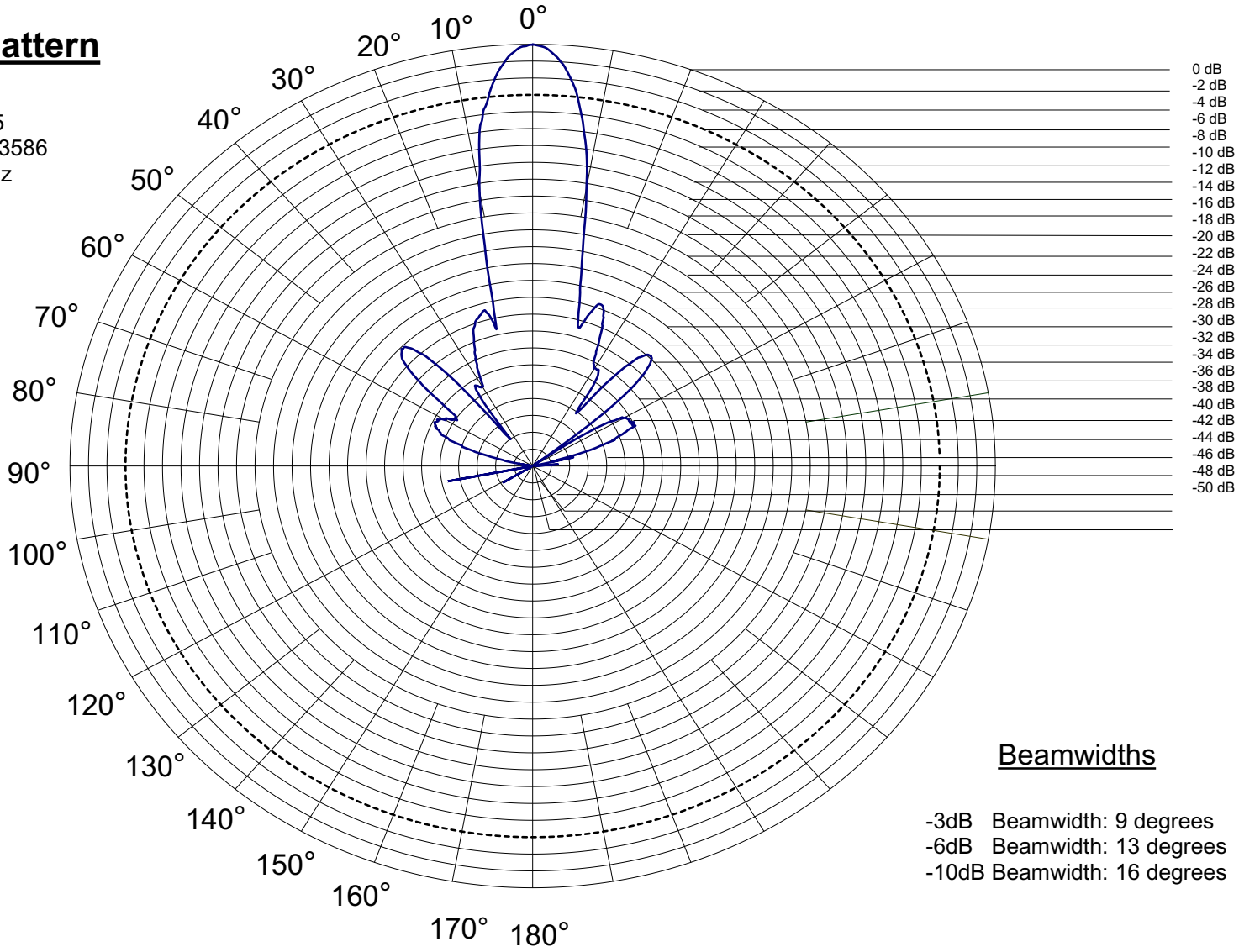

Beamwidths

-3dB Beamwidth: 9 degrees
-6dB Beamwidth: 13 degrees
-10dB Beamwidth: 16 degrees

Airmar Part Number: M475-MTNC
Serial Number: SN60173586 70kHz
Test Date: 9/11/2019

Filename: SN60173586 70kHz.xls